A NEW **WATER** CALORIMETER FOR MODERN RADIOTHERAPY
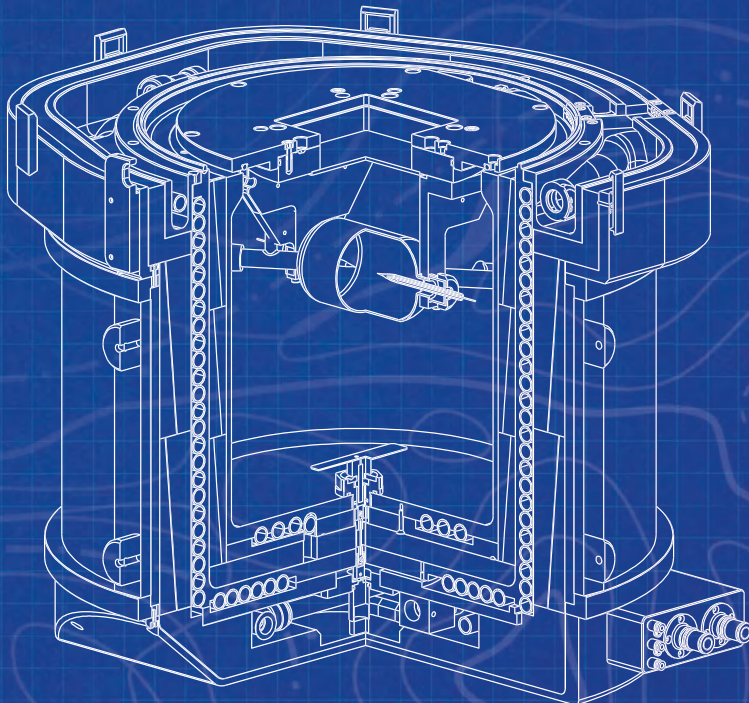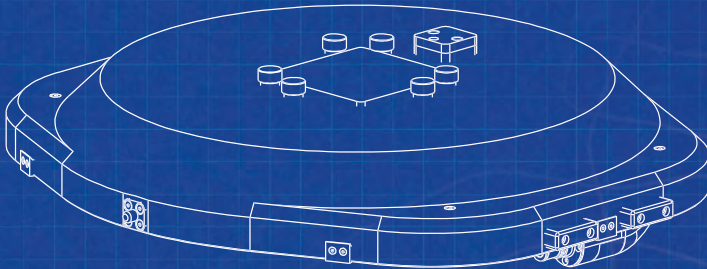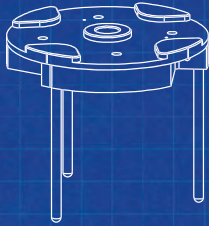
Leon de Prez

A new water calorimeter for modern radiotherapy

Leon de Prez

A new water calorimeter for modern radiotherapy

Een nieuwe watercalorimeter voor de moderne radiotherapie

(met een samenvatting in het Nederlands)

Proefschrift

ter verkrijging van de graad doctor aan de Universiteit Utrecht
op gezag van de rector magnificus, prof. dr. H.R.M.B. Kummeling,
ingevolge het besluit van het college voor promoties
in het openbaar te verdedigen
op donderdag 26 september 2019 om 12.45 uur

door

Leon Armand de Prez

geboren op 1 maart 1975 te Schiedam

Table of Contents

1

Introduction

1.1. Radiation therapy

Radiation therapy (radiotherapy) uses ionizing radiation to kill cancer cells and sterilize tumours. This is done by delivering the highest possible radiation dose to the malicious tissue while sparing healthy tissue. Ultimately, this results in a successful treatment with the least possible side effects and the best possible quality of life for the patient. In clinical terms: the aim of radiotherapy is to improve the balance of tumour control versus normal tissue complication incidence.

In external beam radiotherapy (EBRT or *teletherapy*[1]) the tumour inside the patient is irradiated with beams of ionizing radiation originating from a source outside the patient. During the treatment, the patient is placed on the treatment couch in the treatment room of a linear accelerator. Radiation beams of various shapes and energy are targeted towards the treatment volume. This takes place according to a treatment plan that is based on pre-treatment imaging and dose calculations. A typical treatment takes between 10 and 20 minutes and is usually repeated over a period of several days to weeks in which the patient returns to the radiotherapy department on a daily basis.

Multidisciplinary teams, consisting of radiation oncologists, radiotherapy technologists (RTTs), medical physicists and medical physics engineers, contribute to the treatment process (van der Merwe *et al* 2017, IAEA 2017). The success of the treatment outcome depends on numerous factors such as patient-specific clinical aspects, and tumour-specific biological aspects, anatomy changes during the treatment period, positioning of the patient and accuracy of the physical dose delivery in relation to the treatment plan. The medical physics team is responsible for the accurate delivery of the treatment dose. Among other aspects, this depends on the dosimetric and geometric accuracy of the radiation treatment equipment (i.e. clinical accelerators) including its commissioning data such as dose output factors and beam profiles. It involves reference dosimetry based on available Codes of Practice (CoPs), machine quality control (QC), calibration of equipment and implementation of quality procedures.

---

1 opposed to *brachytherapy*, where the radiation source is brought close to the tumour, often inside the patient

1.2. Accurate radiotherapy dose delivery

1.2.1. Accuracy

Accuracy of the dose delivery can be defined in analogy to *measurement accuracy*[2] as 'the closeness of agreement between the *planned absorbed* dose and the *true absorbed dose* delivered to the patient'. It is dependent on many factors (e.g. adequate staffing, training, QA programmes, QC tools, etc.), including adequate *calibration*[3] of treatment machines and dosimetry equipment. The latter involves the measurement of the quantity *absorbed dose to water*, D_w. The concept *measurement accuracy*, however, cannot be given a numerical value since the *true value* is never known exactly. A measurement is said to be more accurate when it offers a smaller measurement error (JCGM 2012). Therefore, accuracy of a measurement is expressed by its measurement uncertainty, explained in section 1.3.3.

1.2.2. Importance of accuracy in radiotherapy

The success of the individual patient treatments as well as the quality of clinical trial studies relies on the accuracy of the dose delivery during the radiotherapy process. Besides, decisions on prescribed doses for specific tumour sites and individual patients are based on the outcome of these clinical trials: i.e. if the accuracy in the delivered dose during clinical trials is low, the evidence for effectiveness of the treatment might be questionable. To ensure confidence in the accuracy or the measurement results they must be *traceable*[4] to physical standards that are directly linked to the international system of units (SI, Système International). This is explained in section 1.5.

1.2.3. Accuracy requirements in radiotherapy

It is well recognized that accuracy in the radiation dose delivery process has an impact on clinical outcome. However, the actual measurement of that outcome has its own uncertainties. Before accuracy is addressed information is needed on its requirements. The IAEA Human Health Series Report No. 31 (van der Merwe *et al* 2017, IAEA 2017) provides nine general recommendations on the aspects of the treatment process, addressed in the next section.

---

2 *measurement accuracy*: closeness of agreement between a measured quantity value and a true quantity value of a measurand (JCGM 2012)

3 *calibration*: operation that, under specified conditions, in a first step, establishes a relation between the quantity values with measurement uncertainties provided by measurement standards and corresponding indications with associated measurement uncertainties and, in a second step, uses this information to establish a relation for obtaining a measurement result from an indication (JCGM 2012)

4 *metrological traceability*: property of a measurement result whereby the result can be related to a reference through a documented unbroken chain of calibrations, each contributing to the measurement uncertainty (JCGM 2012)

1.3. Accuracy recommendations

IAEA recommendations 1, 3, 7 and 9 are related to the accuracy aspects of the radiation treatment:

IAEA recommendation 1. 'All forms of radiotherapy should be applied as accurately as reasonably achievable (AAARA), technical and biological factors being taken into account.'

IAEA recommendation 3. 'The data found in Tables 15 and 16 (IAEA 2017) for external beam radiotherapy (EBRT) and brachytherapy, respectively, should be used as a guide for estimating the levels of accuracy that are practically achievable …'

IAEA recommendation 7. 'For reporting purposes, as part of clinical trials, publications, etc., the uncertainties associated with the relevant quantities and parameters should be estimated and presented …', quoting ICRU report 83 (ICRU 2010).

IAEA recommendation 9. 'A number of areas of research should be pursued to aid with improvements in providing accurate and safe radiotherapy with reduced uncertainties.'

1.3.1. AAARA (IAEA recommendation 1)

The issue of quantifying *what is reasonable* is not trivial. It is generally accepted that accuracy requirements are based on biological effects in the form of dose-response data, i.e. Tumour Control Probability (TCP) and Normal Tissue Complication Probability (NTCP). An under-dose to the tumour could yield a decrease in the probability of tumour control while, for normal tissues, an overdose could yield a significantly higher probability of morbidity. Consequently, the accuracy of the delivered dose directly contributes to the success of individual patient treatment. At the same time, the decisions for treating individual patients are based on the outcome of clinical studies. This emphasises the importance of early adoption of the IAEA recommendation when new treatment techniques are introduced, including the AAARA concept in measurements.

The term *accuracy* is often used to qualify the proficiency of a measurement for its purpose. A measurement is accurate (enough) or it is not. It is defined as 'the closeness of agreement between a measured quantity value and a true quantity value of a measurand' (JCGM 2012). However, the *true quantity value* is considered unique and unknowable. Therefore, the concept of *measurement accuracy* cannot be given a numerical value *Accuracy* is usually expressed numerically by a measure of estimated *inaccuracy*[5]. In

---

5   Note that the term 'measurement accuracy' should not be confused with 'measurement precision' which relates to the closeness of agreement between indications or measured quantity values obtained by repeated measurements. Measurements can be very precise (repeatable), without being accurate (close to the true value).

general, a measurement is said to be more accurate when it offers a smaller measurement *uncertainty*. The discussion on what is reasonable and achievable depends on the purpose of the measurement and the resources and information available.

1.3.2. Accuracy levels (IAEA recommendation 3)

The accuracy requirement on each individual part of the dose delivery process must be significantly less than the overall requirement in order to achieve the final recommended accuracy value (Thwaites 2013). This means that, to reach the required uncertainty of around 3.5 % (see section 1.3.4), the uncertainty in each contributing step of the dose delivery process should be of the order of 1 % ($k = 1$, explained in the next section). According to (IAEA 2017), the absorbed dose at a reference point in a water phantom for MV-photon beams, D_w, should have an uncertainty not larger than 1.5 % and preferably of the order of 1 % ($k = 1$). The exact requirement depends on the AAARA principle (section 1.3.1).

1.3.3. Presentation of uncertainty (IAEA recommendation 7)

Accuracy is expressed by a measure of *uncertainty*. The combined standard uncertainty, u, is a non-negative value characterizing the expected spread of the quantity to be assessed. Uncertainties are expressed in terms of expanded uncertainty, U, where U is the standard uncertainty, u, multiplied by coverage factor k (not to be confused with measurement correction factors, k, explained later). For a normal distribution, $k = 1$ corresponds to a coverage probability of 68 %, while $k = 2$ corresponds to a coverage probability of 95 %.

The combined standard uncertainty of a measurement, u, is established by combining the information available from various uncorrelated components, u_i. This combination takes place in quadrature such that $u^2 = \Sigma(u_i^2)$, thus $u = \sqrt{(\Sigma(u_i^2))}$. This quadratic summation makes the larger uncertainties dominate the overall uncertainty. Some of the uncertainty contributions originate from a *Type A* contribution. Type A uncertainties are evaluated from the statistical distribution of repeated measurements. It can be characterized by standard deviations (SD), representing the spread of individual samples. Or it can be characterized as the standard deviation of the mean (SDOM) of N samples (SDOM = SD/$\sqrt{N}$), when the user is interested in the best estimate of a quantity based on N measurements. All uncertainty contributions not originating from a repetition of measurements are of *Type B*. *Type B* uncertainties are evaluated from (estimated) probability density functions, based on experience or other information.

In this thesis, the standard uncertainty of measurement are determined in accordance with the Guide to the Expression of Uncertainty in Measurement (JCGM 2008). The

combined uncertainty in the measurement is established by a numerical table, showing the individual uncertainty contributions, u_i, to the measurement result (see e.g. Aalbers *et al* 2008, EA 2013, JCGM 2008). This leads to a 'combined standard uncertainty', u (sometimes expresses as u_c), and a reported expanded uncertainty with coverage factor $k = 2$. For example a calibration coefficient of a Farmer-type ion chamber in a beam of ^{60}Co can be expressed as '$N_{D,w} = (45.31 \pm 0.45)$ mGy nC^{-1} ($k = 2$)'; a correction factor can be expressed as '$k_B = 0.963(4)$ with $k = 1$' where the standard uncertainty is represented between brackets as the least significant digits of the reported value.

1.3.4. Improvement of accuracy (IAEA recommendation 9)

The accuracy improvement of radiotherapy concerns all steps involving the delivery of absorbed dose. This was studied previously (Brahme 1984, Mijnheer et al 1987, Wambersie 2001). It was concluded by Mijnheer *et al* (1987) that any transfer of information from one radiotherapy clinic to another would introduce unacceptable risks of complications if the overall uncertainty in the absorbed dose value would be larger than about 7 %. This value was considered the expanded uncertainty (U with a coverage factor, $k = 2$), resulting in a requirement for the combined standard uncertainty, u, in the absorbed dose delivery of 3.5 %. These accuracy requirements were partially based on the clinical information and procedures available at that time. In addition to technological changes and advancements in dosimetry equipment, new data have been published from clinical studies using new technologies. Based on this, the accuracy requirements in radiotherapy have recently been revised (Thwaites 2013, IAEA 2017). These studies show that from clinical considerations and practically achievable accuracy levels, no single number suffices to describe the accuracy requirements. However, it was concluded that in most cases, uncertainty requirements for dose delivery in external beam radiotherapy should be reduced to 3 % and in some cases to 2 % ($k = 1$). The accuracy improvement of absorbed dose delivery is directly linked to the reduction of measurement uncertainties in reference dosimetry and measurement of the quantity absorbed dose to water, D_w, addressed in this study.

1.4. The need for traceable dosimetry in radiotherapy

For existing radiotherapy applications, dosimetry and Codes of Practice (CoPs) are usually well established. However, when new treatment modalities or techniques are introduced, existing CoPs could become (partially) invalid because of a change in methods and fundamental instrument corrections or physical constants. Even though analytical models exist to describe the instrument behaviour or calculate physical constants, they are inherently limited by the applied physical models and their input data. In those cases, it is essential that measurements are performed to determine or

support physical data (e.g. detector correction factors) provided by the CoPs. In principle, the clinical introduction of new treatment modalities is hampered by two issues:

a) a lack of a suitable dosimetry standards, resulting in the absence of international traceability;
b) a lack of Codes of Practice for reference dosimetry to ensure patient safety and to increase confidence in the results from clinical trials.

Dosimetry standards and Codes of Practice are essential to ensure reliable and accurate measurements for (the initial) patient treatments and clinical trials on which decisions are based for future patients. To support future Codes of Practice, there is a strong demand for traceable measurements and calibration of reference dosimetry equipment in new treatment modalities. To ensure confidence in measurement results, they must be directly linked to the international system of unit (SI, Système International), that is, traceable to internationally accepted primary measurement standards.

1.5. International traceability organized by the BIPM

On a global level, *metrology*[6], including dosimetry, is organized by the International Bureau of Weights and Measures, the BIPM (i.e. the *international standards laboratory*). The BIPM provides the basis for a single coherent system of measurements throughout the world, traceable to the International System of Units (SI, *Système International*). The International Committee for Weights and Measures (CIPM) is the scientific supervisory board of the BIPM, that in turn has 10 Consultative Committees (CCs) for the various fields of metrology expertise. For ionizing radiation and dosimetry the Consultative Committee for Ionizing Radiation (CCRI) is advising the CIPM. At the highest international political level, metrology is organized by the General Conference on Weights and Measures (CGPM), where representatives from governments worldwide meet every four years to discuss and decide on issues of the worldwide metrology infrastructure.

A framework for international traceability in measurements worldwide is established by the CIPM Mutual Recognition Arrangement, the CIPM MRA (CIPM 1999). It was established in 1999 as a formal system whereby countries recognize each other's *calibration and measurement capabilities* (CMCs) as being equivalent. The core data of the CIPM MRA are held in the BIPM *key comparison database* (KCDB) on the BIPM website (BIPM 2019). The equivalence of the CMCs is based on comparisons

---

6   *metrology:* the science of measurement and its application (JCGM 2012)

of national standards that are organized by the Consultative Committees (the CCRI for ionizing radiation and dosimetry) on behalf of the CIPM. These are predominantly *key comparisons* that lead to *degrees of equivalence* (DoEs, see section 3.5) for the participating National Metrology Institutes (NMIs). The comparisons organized by the BIPM are normally an ongoing series of bilateral comparisons in key areas for the NMIs with the highest technical competence. In dosimetry these are the primary standards dosimetry labs (PSDLs) and the comparisons are against stable reference standards of the BIPM. The measurements made with the BIPM standard form the basis of the *key comparison reference value* (KCRV) relative to which the DoEs are established for the NMIs that participate, explained elsewhere (Allisy et al 2009). The final comparison report must be approved by the relevant Consultative Committee, after which the results and degrees of equivalence may be published in the KCDB. All the CMCs in the KCDB have been through a rigorous intra- and inter-regional review process to ensure their validity under the CIPM MRA.

In reference dosimetry, the DoEs with BIPM are established by the PSDLs relative difference of compared absorbed dose to water, D_w, to BIPM and their relative expanded uncertainty, $U_{D,w}$ established by the PSDL, both in relative values. $U_{D,w}$ is usually equal or close to the uncertainty provided by the PSDL for calibration of dosimetry equipment. This is the first step towards traceable reference dosimetry for radiotherapy.

1.6. Reference dosimetry and its uncertainty

1.6.1. Reference dosimetry

Medical linear accelerators in radiotherapy are calibrated in terms of absorbed dose to water, D_w, in the unit gray[7] (Gy), where 1 Gy represents the absorption of 1 Joule of radiation energy per unit of mass in kg (i.e. 1 Gy = 1 J kg^{-1}). Calibration of linear accelerators is usually achieved through a transmission ion chamber (the beam passes through its thin entry and exit windows), that is placed between the accelerator focus and the collimator jaws inside the accelerator treatment head. The reading of this transmission ion chamber is expressed in arbitrary monitor units (MU) which is, after calibration, related to the absorbed dose under reference conditions in a water phantom: i.e. D_w per transmission monitor reading in Gy MU^{-1}. The general formalism for measurement of D_w is performed according to commonly applied Codes of Practice, CoPs (e.g. Hohlfeld 1988, Klevenhagen *et al* 1996, Aalbers *et al* 2008, Almond *et al* 1999, McEwen *et al* 2014, Lillicrap *et al* 1990, Palmans *et al* 2017) and given by:

---

7   named after medical physicist / radiobiologist Louis Harold Gray (1905 – 1965)

$$D_{\mathrm{w}} = M \cdot N_{D_{\mathrm{w}},Q_0} \cdot k_{\mathrm{Q}}. \tag{1.1}$$

Here, M is the ion chamber reading corrected for influence quantities (i.e. temperature, pressure, chamber bias polarity, incomplete charge collection, etc.). N_{D_{w},Q_0} is the ion chamber calibration coefficient for absorbed dose to water in the reference beam quality, Q_0, usually ^{60}Co. Ion chamber calibration coefficient, $N_{D_{\mathrm{w}},Q}$, in the beam quality Q is valid under reference conditions as specified in the relevant CoPs and determined according to:

$$N_{D_{\mathrm{w}},Q} = \frac{D_{\mathrm{w}}}{M}. \tag{1.2}$$

This equation applies also $N_{D_{\mathrm{w}},Q0}$ in beam quality Q_0, usually ^{60}Co, and is valid without the presence of a magnetic field, i.e. $B = 0$ T. D_{w} is determined with a reference measurements standard, in this study a water calorimeter, used as an absorbed dose to water primary standard. k_{Q} in equation (1.1) is a factor that corrects its calibration coefficient in beam quality Q_0 (in this study ^{60}Co) to that in the user beam quality Q. Note that k_{Q} is usually expressed as k_{Q,Q_0} However, when reference beam quality Q_0 is ^{60}Co it is simply expressed as k_{Q} and follows (Andreo 1992):

$$k_{\mathrm{Q}} = \frac{N_{D_{\mathrm{w}},Q}}{N_{D_{\mathrm{w}},Q_0}}. \tag{1.3}$$

When measurements are performed in beam quality Q and in the presence of a magnetic field, B, the change in chamber response due to the magnetic field also needs to be accounted for by a factor k_{B} (or $k_{\mathrm{Q,B}}$ when k_{Q} and k_{B} are combined). k_{Q} in equation (1.1) is then replaced by $k_{\mathrm{Q,B}}$ and equation (1.3) becomes:

$$k_{\mathrm{Q,B}} = \frac{N_{D_{\mathrm{w}},Q,B}}{N_{D_{\mathrm{w}},Q_0}}, \tag{1.4}$$

with

$$k_{\mathrm{Q,B}} = k_{\mathrm{Q}} \cdot k_{\mathrm{B}} = \frac{N_{D_{\mathrm{w}},Q}}{N_{D_{\mathrm{w}},Q_0}} \cdot \frac{N_{D_{\mathrm{w}},Q,B}}{N_{D_{\mathrm{w}},Q}}. \tag{1.5}$$

If no magnetic field is present (i.e. at 0 T), equation (1.5) reduces to equation (1.3). Values for k_{Q} or $k_{\mathrm{Q,B}}$ can be obtained from:

a) measurement for a specific ion chamber based on calibrations in beam qualities, Q (optionally with $B \neq 0$ T) and Q_0;

b) measurement of generic k_Q or $k_{Q,B}$ values for the ion chamber type of interest;

c) calculated generic k_Q or $k_{Q,B}$ values for the ion chamber type of interest, e.g. based on analytical models or (partial) Monte Carlo simulations.

To obtain k_Q or $k_{Q,B}$ factors by option a) and b), measurements with an absorbed dose to water primary standard in the beam qualities Q and Q_0 of interest are required. Option a) requires a PSDL to have continuous access to beam quality Q, while option b) requires a transportable primary standard that is operable on-site at the required accelerator facilities.

1.6.2. Uncertainty in reference dosimetry

In reference dosimetry, uncertainties are often expressed as relative values, in %. For determination of D_w in medical linear accelerators, each term on the right hand-side of equation (1.1) contributes to the relative uncertainty in the measurement of absorbed dose in beam quality Q (and magnetic field B), $u_{D,w}$:

$$u_{D_w} = \sqrt{(u_M)^2 + \left(u_{N_{D_w,Q_0}}\right)^2 + \left(u_{k_{Q,B}}\right)^2}. \tag{1.6}$$

For measured $k_{Q,B}$ values (equal to k_Q when $B = 0$ T), the relative uncertainty is determined by the uncertainties in the calibration coefficients in beam quality Q (optionally in magnetic field B) and beam quality Q_0, ^{60}Co without magnetic field.

To ensure that the absorbed dose delivered to patients in radiotherapy clinics worldwide can be compared, confidence in results for reference dosimetry, D_w and its uncertainty is essential. Therefore, measurements must be traceable to internationally accepted primary dosimetry standards in such a way that the absorbed dose determined in any two radiotherapy clinics in the world agree within their claimed uncertainty.

1.7. Recent advances in external beam radiotherapy

1.7.1. Flattening filter free beams (FFF)

Recently, major advances in external beam radiotherapy (EBRT) have led to an increased complexity in providing traceable measurements in clinical treatment beams[8]. *Flattening*

---

8 Technological developments have moved from conventional two-dimensional (2D) radiotherapy to the implementation of three-dimensional (3D) conformal radiotherapy (CRT), intensity modulated radiotherapy (IMRT), volumetric-modulated arc therapy (VMAT), image-guided radiotherapy (IGRT), adaptive radiotherapy (ART) and four-dimensional (4D) imaging and motion management in radiotherapy (Thwaites and Malicki 2011, Yu and Tang 2011).

filter free (FFF) beams became available for applications such as intensity-modulated radiotherapy (IMRT) and volumetric-modulated arc therapy (VMAT) (Georg *et al* 2011, Paynter *et al* 2014). The main advantages of FFF compared to *conventional flattening filtered* (cFF) beams are the increased dose rate, resulting in reduced treatment time, reduced lateral beam quality variation and a reduced out-of-field dose to the patient (Robar *et al* 2002, Titt *et al* 2006, Vassiliev *et al* 2006). However, application of FFF beams raised the question if ion chamber k_Q factors, given in existing Codes of Practice that were developed for cFF beams could also be apply in FFF beams.

1.7.2. MRgRT devices

Currently, integrated MRI-guided radiotherapy treatment (MRgRT) devices are under development or in clinical use (Fallone 2014, Keall *et al* 2014, Lagendijk *et al* 2014b, Mutic and Dempsey 2014). They allow for unprecedented visualization and motion tracking of the target during the actual treatment, in real time. Dosimetry in the presence of a magnetic field, *B*, is however not trivial because the energy deposition of the secondary electrons trajectories are influenced by the Lorentz force. Dose distributions change e.g. in build-up and penumbra regions, in the central beam region and at material or tissue interfaces (Raaijmakers *et al* 2008, Raaymakers *et al* 2004, Oborn *et al* 2010, Woodings *et al* 2018). The magnitude of these dose effects depends on the magnetic field strength and its orientation relative to the photon beam, material differences and density inhomogeneities. Not only the dose distribution is affected but also the response of commonly used dosimeters in terms of their calibration coefficient as e.g. described by van Asselen *et al* (2018).

1.7.3. Ion chamber correction factors in new modalities

Existing CoPs do not provide ion chamber correction factors for application in the new types of treatment machines. Currently these involve k_Q factors for FFF beams and k_Q and k_B factors for treatment machines incorporating strong magnetic fields. k_Q values have been determined by analytical models and (partial) Monte Carlo calculations. Here, direct measurements are essential to validate model results. Recently attempts have been made to calculate k_B factors, however complications in doing so involved the ion chamber dead-volume effect that has been unquantified until now (Butler *et al* 2015). For MRgRT facilities, measurements are essential to ensure applicable ion chamber correction factors. Besides, calculations are inherently limited by the use of models for both ion chambers and accelerator beams, especially when it involves new equipment not characterized before. Therefore, direct measurement of k_Q and k_B factors with primary standards are essential to understand the behaviour of physical chambers in real clinical treatment machines and their reference conditions.

1.8. Target uncertainties for k_Q and $k_{Q,B}$

Each term on the right-hand side of equation (1.6) contributes to the uncertainty in the measurement of absorbed dose, $u_{D,w}$, with a target for D_w, $u_{D,w}$ of 1.0 % - 1.5 % ($k = 1$) according to IAEA recommendation 3 (see section 1.3.2). Referring to equation (1.6), the corrected ion chamber reading M can be measured with a standard uncertainty of u_M of 0.4 % or smaller. The quantity $N_{D,w,Q0}$, is the ion chamber calibration coefficient for absorbed dose to water in reference beam quality ^{60}Co, this is provided by the primary or secondary dosimetry laboratory (PSDL or SSDL) with an uncertainty, $u_{ND,w,Q0}$ between respectively 0.5 % and 0.7 % (BIPM 2019). $k_{Q,B}$ can be expressed as the product of k_Q, the ion chamber beam quality correction factor and k_B, the ion chamber magnetic field correction factor (see Chapter 6). Note that k_B is unity with no uncertainty when no magnetic field is applied.

Based on the target uncertainty requirement for D_w (with $u_{D,w}$ between 1.0 % and 1.5 %), from the uncertainties in $N_{D,w,Q0}$ ($u_{ND,w,Q0} < 0.7$ %) and M ($u_M < 0.4$ %), follows the uncertainty requirement for $k_{Q,B}$, $u_{kQ,B}$ to be between 0.6 % and 1.2 % ($k = 1$).

1.9. The need for transportable D_w primary standards

For conventional radiotherapy applications, dosimetry procedures and traceability are well established (see e.g. Hohlfeld 1988, Klevenhagen *et al* 1996, Aalbers *et al* 2008, Almond *et al* 1999, McEwen *et al* 2014, Lillicrap *et al* 1990, Palmans *et al* 2017). These CoPs in general provide the ion chamber k_Q correction factors for their application in conventional EBRT machines. Since it is neither financially nor practically feasible for primary standard dosimetry laboratories (PSDLs) to establish reference beam qualities for all novel radiotherapy modalities in-house, there is a fundamental need for primary standards that can be transported and operated in a clinical environment, on-site.

Although some calorimeters have been designed to operate on-site (McEwen and Duane 2000, Krauss 2006b, Rapp *et al* 2013, Renaud *et al* 2013), only BIPM has recently reported on-site measurements with a transportable primary absorbed-dose standard (Picard *et al* 2009, 2013b), described in Chapter 3. Operation of an absorbed dose to water primary standard on-site calls for special demands on its construction and operation while maintaining the best possible uncertainty. Evidently the equipment needs to be compact, transportable, and easy to set up. As beam time is often limited, the measurements need to be performed within a short time. Since the performance of the measurement equipment needs to be checked frequently, i.e. before and after the on-site measurements, components need to be calibrated and validated using standard
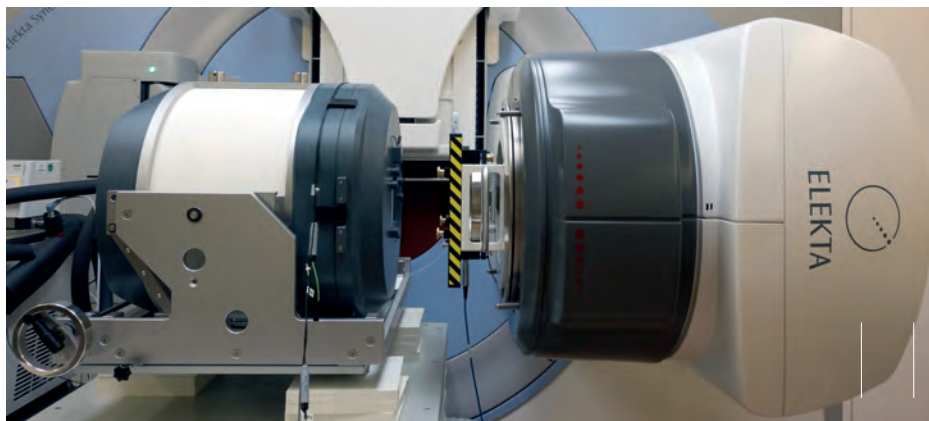
Figure 1-1. The new water calorimeter in front of a clinical accelerator at NKI-AVL in Amsterdam (The Netherlands).

procedures at the home laboratory. Due to the diversity of beam geometries such as orientation (vertical and horizontal), distances to the treatment machine and availability of space, the measurement phantom needs to be flexible in alignment.

In order to make the measurement results obtained with the primary standard accepted at an international level via the CIPM MRA (see section 1.5), its calibration measurement capabilities (CMC) needs to be documented in the BIPM key comparison database (KCDB). For this, participation in an internationally accepted key comparison, e.g. organized by the BIPM, is essential.

1.10. This thesis

The aim of this thesis is to develop an absorbed dose to water primary standard, a water calorimeter, that can be fully applied on-site in modern clinical EBRT facilities, including MRgRT devices. The new primary standard, realizing the quantity absorbed dose to water, D_{w}, in the unit gray (Gy), is designed and constructed with the purpose to calibrate radiation detectors (mostly ion chambers) in order to measure beam quality correction factors, k_{Q}, and magnetic field correction factors, k_{B}, with a target standard uncertainty smaller than 1.0 % ($k = 1$).

Chapter 2 describes the new transportable water calorimeter and its validation as an absorbed dose to water primary standard for application in the standards laboratory (PSDL) and in clinical (MRI-incorporated) treatment machines. Special attention was paid to its operation in a restricted space and with different beam geometries and beam

modalities including the operation in magnetic fields. Validations were performed in the VSL ^{60}Co beams against the previous calorimeter and on-site in horizontal and vertical clinical MV-photon beams. Uncertainty budgets for ^{60}Co and MV-photons are described, including a budget for application in a magnetic field.

Chapter 3 describes the participation of the new water calorimeter in the BIPM.RI(I)-K6 key comparison between BIPM and VSL in accelerator photon beams. This comparison took place on-site at the accelerator faculty of the National Physical Laboratory in Teddington (UK). The comparison was based on the determination of absorbed dose to water, D_w in the unit Gy, for three radiation qualities. It resulted in the registration of degrees of equivalence (DoEs) for VSL in the BIPM key comparison database, a prerequisite for providing direct traceability to the international system of units (SI, Système International) through its new primary standard.

Chapter 4 describes the application of the new water calorimeter to measure for the first time k_Q factors in pairs of clinical flattening filter free (FFF) and conventional flattening filter (cFF) MV-photon beams. The aim of this study was to assess to which extent k_Q factors, based on existing Codes of Practice (CoPs), could be applied in the new FFF beams for clinical reference dosimetry. This was done by comparing measured k_Q factors for a selection of three Farmer-type ion chambers (8 serial numbers) in FFF-cFF beam pairs of a clinical Elekta VersaHD.

Chapter 5 describes commissioning of the calorimeter and its performance as an absorbed dose to water primary standard in the 7 MV-photon beam of a pre-clinical MRI-linac at a 1.5 T magnetic field. The measurements were repeated without magnetic field. The goal was to validate the calorimeter claimed standard uncertainty for measurement of D_w in the presence of a magnetic field, as described in Chapter 2. Evaluation took place on a parameter by parameter basis, including a thermodynamic description of potential effects on the heat capacity of water due to the magneto-caloric effect (MCE).

Chapter 6 describes the application of the water calorimeter to measure for the first-time ion chamber k_Q and k_B factors. The correction factors were measured for two types of commonly used waterproof Farmer-type ion chambers (6 serial numbers) by calibration in the VSL ^{60}Co source (0 T) and in a pre-clinical 7 MV MRI-linac at 0 T (for k_Q) and at 1.5 T (for k_B). The results are compared with the available literature values.

In Chapter 7 this thesis is summarized, followed by a general discussion and conclusion in Chapter 8.

1.11. Disclaimer

Certain commercial equipment, instruments, or materials are identified in this report to specify adequately the experimental procedure. Such identification does not imply recommendation or endorsement, nor that the materials or equipment identified are necessarily the best available for the purpose.

2

A water calorimeter for on-site absorbed dose to water calibrations in ^{60}Co and MV-photon beams including MRI-incorporated treatment equipment

Abstract

In reference dosimetry the aim is to establish the absorbed dose to water, D_w, under reference conditions. However, existing dosimetry protocols are not always applicable for rapidly emerging new treatment modalities. For primary standard dosimetry laboratories (PSDLs) it is generally not feasible to acquire such modalities. Therefore, it is strongly desired that D_w measurements with primary standards can be performed on-site in clinical beams for the new treatment modalities to characterize and calibrate detectors. To serve this need, VSL has developed a new transportable water calorimeter serving as a primary D_w standard for ^{60}Co and MV-photons including MRI-incorporated treatment equipment. Special attention was paid to its operation in different beam geometries and beam modalities including the application in magnetic fields. The new calorimeter was validated in the VSL ^{60}Co beam and on-site in clinical MV-photon beams. Excellent agreement of 0.1 % was achieved with previous ^{60}Co field calibrations, i.e. well within the uncertainty of the previous calorimeter and with measurements performed in horizontal and vertical MV-photon beams. k_Q factors, determined for two PTW 30013 ionization chambers, agreed very well with available literature data. The relative combined standard uncertainty ($k = 1$) for D_w measurements in ^{60}Co and MV-photons is 0.37 %. Calibrations are carried out with a standard uncertainty of 0.42 % and k_Q factors are determined with a standard uncertainty of 0.40 %.

2.1. Introduction

In clinical reference dosimetry the aim is to establish the absorbed dose to water, D_w, under defined reference conditions. Novel radiotherapy modalities, such as those using flattening filter free photon beams (Georg *et al* 2011) and MRI-incorporated treatment equipment (Lagendijk *et al* 2014a), are being developed rapidly. Existing protocols for reference dosimetry do not cover these new modalities. For some modalities their application has been called into question (Dalaryd *et al* 2014) and for some modalities they cannot be applied without additional correction factors (Smit *et al* 2013). Therefore, development of measurement methods for these modalities is crucial, and it is strongly desired that D_w measurements with primary standards can be performed for these novel modalities to provide or validate input data for reference dosimetry protocols.

Since it is neither financially nor practically feasible for most primary standard dosimetry laboratories (PSDLs) to establish reference beam qualities for novel radiotherapy modalities in-house, there is an increasing need for on-site absorbed-dose measurements using transportable primary standards. Although some calorimeters have been designed to operate on-site (McEwen and Duane 2000, Krauss 2006a, Rapp *et al* 2013, Renaud *et al* 2013, 2015), only BIPM has reported on-site measurements with a transportable primary absorbed-dose standard (Picard *et al* 2009, 2010a). VSL has previously operated a transportable water calorimeter in clinical accelerator beams for direct use to the medical physics community (Aalbers *et al* 2008).

In the past years VSL has developed a new transportable water calorimeter as a primary absorbed-dose standard, replacing the current calorimeters (Aalbers 2003, de Prez 2008, de Prez and de Pooter 2008) for application in photon beams with energies between 100 kV and 25 MV including the application in magnetic fields with respect to MRI-incorporated treatment equipment. Its design and measurement procedures were in all aspects optimized for efficient on-site operation. In 2012 the calorimeter specifications and conceptual design were drafted. In 2013 the calorimeter was designed in detail and constructed. In the first half of 2014 it was commissioned in the VSL ^{60}Co beam and compared to dose-to-water values obtained with previous calorimeters. In August 2014 commissioning took place in horizontal and vertical beams of 6 MV and 10 MV in a clinical accelerator at Netherlands Cancer Institute in Amsterdam (The Netherlands). The new calorimeter participated in the EURAMET.RI(I)-S13 for medium energy x-ray beams (Büermann *et al* 2016) and ongoing BIPM key comparison BIPM.RI(I)-K6 (Picard *et al* 2017), described in Chapter 3. The latter comparison took place on-site at the accelerator facilities of the National Physical Laboratory in Teddington (United Kingdom).

Operation of an absorbed dose to water primary standard on-site calls for special demands on its construction and operation while maintaining the best possible uncertainty. Evidently the equipment needs to be compact, transportable, and quick to set-up. As beam time is often limited, the measurements need to be performed in a timely manner. Since the performance of the measurement equipment needs to be checked frequently, i.e. before and after the on-site measurements, components need to be calibrated and validated using standard procedures at the home laboratory. Due to the diversity of beam geometries such as orientation (vertical and horizontal), distances to the treatment machine and availability of space, the measurement phantom needs to be flexible in alignment. This study describes the new calorimeter design, construction, operation specific features, corrections and validation in ^{60}Co and MV-photon beams. In addition, the performance of the temperature sensors in the presence of a magnetic field was evaluated. Uncertainties are expressed as relative standard uncertainties ($k = 1$), in some cases represented between brackets as the least significant digits of the reported value.

2.2. Materials and methods

2.2.1. Water calorimetry

Water calorimetry is generally considered to be the most direct way of determining D_w (Seuntjens and Duane 2009, Andreo et al 2000). The water calorimetric determination of absorbed-dose requires a measurement of radiation-induced temperature rise in water, ΔT_w (~ 0.24 mK Gy^{-1}), multiplied by the specific heat capacity of water, c_p, and is given by the expression:

$$D_w = \Delta T_w \cdot c_p \cdot (1 - h)^{-1} \cdot k_p \cdot k_c \cdot k_R. \tag{2.1}$$

The chemical heat-defect, h, is caused by radiation-induced exo- or endothermic chemical reactions. For photon beams this effect is described by various authors such as e.g. Domen (1982), Klassen and Ross (1997), Seuntjens and Palmans (1999) and Krauss and Kramer (2003). The k-factors in equation (2.1) correct respectively for the perturbation due to the presence of non-water materials (mostly glass), k_p; conductive heat flow, k_C; and the deviation of the measurement conditions from the reference conditions, k_R (source detector distance SDD, measurement depth d and radial non-uniformity). Because the water calorimeter is operated at 4 °C, the temperature at which the density of water is maximal, it is assumed that no convection takes place (Domen 1988). Radiative heat transfer is insignificant for the small temperature differences generated in a water calorimeter (Seuntjens and Duane 2009).
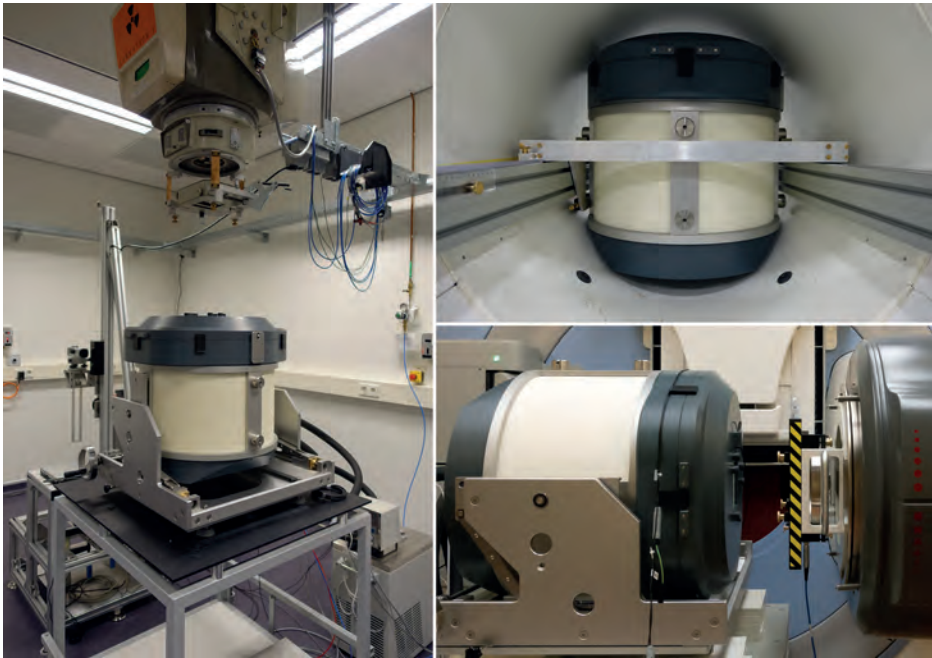
Figure 2-1. The calorimeter in the vertical VSL ^{60}Co beam (left), inside the bore of an Elekta Atlantic MRI-linac at UMC Utrecht in Utrecht, The Netherlands (top right) and a horizontal beam orientation in front of an Elekta Versa HD accelerator at the Netherlands Cancer Institute in Amsterdam, The Netherlands (bottom-right).

2.2.2. Design and construction

Key-features of the new calorimeter are its compact design without compromising the thermal characteristics, its compact measurement equipment, fast procedures and the ability to be operated in horizontal and vertical beams and treatment equipment with patient bore sizes larger than 70 cm (see Figure 2-1). Waterproof dosimeters can be calibrated and characterized directly inside the calorimeter phantom at various depths. Special attention is paid to the measurement methods of SDD and depth in water as well as beam output monitoring. To achieve these requirements all aspects were integrated in the design of the new water calorimeter. Non-ferromagnetic metals were used to facilitate the operation of the calorimeter in the magnetic field of MRI-incorporated treatment equipment.

The thermostat was designed and constructed after being thermally modelled using finite element software (COMSOL Multiphysics, version 4.3 at the time of these simulations used for engineering purposes). It was designed to reach a temperature background signal in the sub-µK s^{-1} range, limiting this signal to approximately less than 10 % of

the expected radiation-induced temperature drift. For the phantom and major thermostat parts, aluminium was chosen because of its convenient conductive, magnetic and mechanical properties and its relatively low Z-number in relation to reduced nuclear activation levels for future measurements in high energy particle beams.

The calorimeter, shown in Figure 2-2, consists of a cylindrical water phantom (diameter 302 mm, height 304 mm) with an aluminium wall (thickness 6 mm) surrounded by a temperature controlled thermostat (weighing 68 kg without water). The phantom is sealed with an aluminium lid containing a PMMA cylindrical support at which the detector (e.g. the water calorimeter high-purity cell or an ionization chamber) is suspended. This support contains a 2.8 mm thick PMMA radiation entrance window which is in direct contact with the water surface when the lid is closed. The calorimeter thermostat is supported by a compact positioning frame (shown on the left and bottom-right photo of Figure 2-1) which enables it to rotate 90° for application in horizontal and vertical beams while keeping the detector and beam geometry with respect to scatter and attenuation identical in both orientations. Measurement cables exit the phantom through an opening on the 'dry' top corner of the phantom lid. The thermostat, surrounding the water phantom, consists of two layers of polyurethane (PU) foam serving as thermal insulators and mechanical separators. Between the layers of PU foam an active thermostat heat-exchanger is present, consisting of liquid cooled polyethylene (PE) tubing mounted on an aluminium heat sink. Another heat-exchanger is placed in the bottom of the water phantom.

The beam enters the calorimeter in the centre of the removable lid through an 11 cm square radiation window and subsequently passes through 10 mm of PU foam and a laminar passive heat sink, illustrated in the expanded view of Figure 2-2. The laminar heat sink is thermally connected to the aluminium heat sink in the lid and consists of 5 layers of 0.1 mm thick aluminium and 4 layers of 2 mm thick PU foam. The design of the laminar heat sink is a trade-off between minimizing heat leakage through the entrance window, to meet the specifications of maximum allowed background temperature drift and minimizing the perturbation of the radiation beam. The presence of the entrance window is not expected to influence the beam quality significantly for ^{60}Co and MV-photon beams.

A liquid recirculation chiller (Lauda ProLine 845C) controls the active heat-exchanger temperature with a Pt-100 temperature probe mounted on it. During stabilisation, a stirrer blade at the bottom of the phantom is rotated electrically. For operation in a magnetic field the electric motor is replaced by a hydraulic vane motor, set in motion by the flow of the cooling liquid and a booster pump, both placed outside the MRI treatment room.
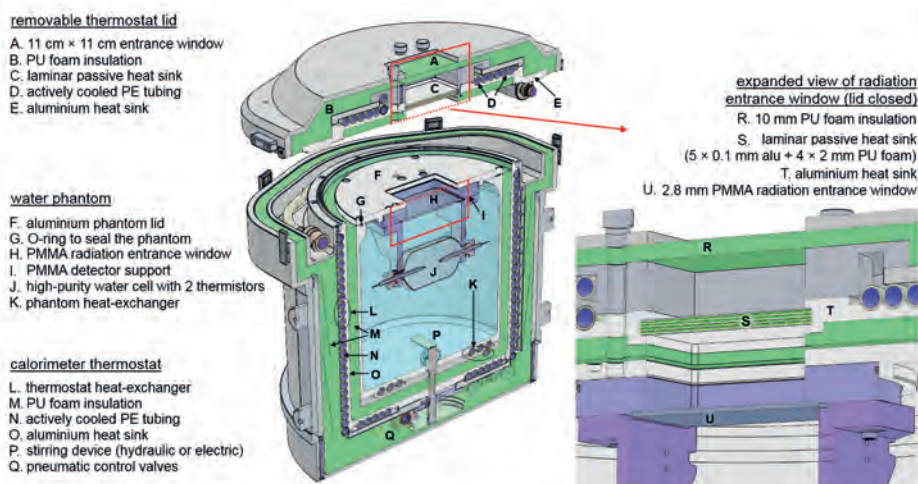
Figure 2-2. Cross-section of the calorimeter containing the high-purity cell at a measurement depth of 10 cm (left) including an expanded view of the radiation entrance window (right).

In conventional MV-photon beams, an external transmission monitor ionization chamber (PTW 34014) is positioned on the accelerator tray between the radiation source and the calorimeter. A 2 mm thick PMMA build-up plate is mounted on the monitor at the beam entrance side to reduce fluctuations in charge build-up as a result of changes in air density between the accelerator target and the thin window transmission monitor. On the monitor frame, at the calorimeter side, a removable PMMA plate is mounted that serves as the accelerator reference plane.

2.2.3. Thermistor probes and high-purity cell

A cylindrical high-purity water cell (HPC) contains two negative temperature coefficient (NTC) thermistors with a tip diameter of 0.3 mm (GE Sensing BR11KA432J-L70MM). A nominal NTC resistance of 10 kΩ at 4 °C was selected as an optimum in stability, sensitivity, and measurement resolution. The NTCs are used to measure the radiation-induced temperature change in water, ΔT_w in equation (2.1). According to the manufacturer, the thermistor consists of manganese, nickel and cobalt transition metal oxides. The thermistors are glued inside miniature glass pipettes with an outer diameter of 0.60 mm using epoxy adhesive (Araldite 2020). The thermistor bead is attached to 30 μm Pt-alloy wires electrically insulated by a capillary micro-tube (PI Mikro Kapilarschlauch). The wires are soldered to a high-quality PTFE-insulated, 4-wire cable.

The thermistor probes are mounted 10 mm apart inside the HPC filled with high-purity

water obtained from a commercially available system (Millipore Milli-Q Integral 3). The HPC is rinsed and filled while the water is kept out of contact with air. Subsequently, it is saturated with argon by a flow of argon gas (< 1 ppm impurities) during at least 1 hour to remove virtually all remaining impurities. A cylindrical HPC with a diameter of 72 mm and glass thickness between 0.9 mm in the centre and 1.4 mm on the sides is used. The glass thickness is measured by means of an ultrasonic precision thickness gauge (K&M Instruments KT-350).

2.2.4. Detector alignment

By mounting a removable alignment tripod on top of the *PMMA detector support* a calorimeter reference plane is introduced (see A in Figure 2-3). The PMMA detector support (B) is mounted on the phantom lid (see F in Figure 2-2) and provides a reproducible mechanical connection between the calorimeter reference plane and the detector or thermistors (D). The tripod can be re-positioned on top of the PMMA detector support with the calorimeter open and closed through a set of holes in the thermostat main lid (see centre picture in Figure 2-3). The distance, t, between the detector (D) and the calorimeter reference plane (A) is measured by means of a cathetometer (E, Nippon Optical Works NCM-D-300) operated with a small telescope containing cross-hairs. This is done by placing the calorimeter phantom lid on top of the sidewalls of a shallow water phantom (F in the upper-right picture in Figure 2-3) with HPC or the detector submerged in water and with the tripod surface (A) positioned on the PMMA detector support (B). The distance, r, between the accelerator reference plane and the calorimeter reference plane (A) is measured with an inside-micrometer, as is the distance, w, between the accelerator reference plane and the *PMMA entrance window* (C). This provides all the distances to trace the location of the detector, phantom surface and depth in water, not visible once the calorimeter lid is closed. Due to hygroscopic properties and potential expansion of the PMMA window, all distances measured after the absorbed-dose measurements, when the thermostat is opened are used for the final analyses.

The thermistor position (D) inside the glass cell and PMMA water phantom is optically measured with the cathetometer and affected by refraction through the tank wall, water and cell wall. For other detectors the PMMA tank wall and water affects the measurement of position D. A correction for the effect caused by the PMMA tank wall and water is determined on-site with a small desk-ruler placed vertical and by measuring with the cathetometer the difference between two respective ruler lines: one below the water surface, near position D, and one above the phantom, near position A. These measurements are repeated without the phantom, with the desk-ruler in the same position. Refraction resulting from the presence of the glass cell wall was optically measured at VSL.
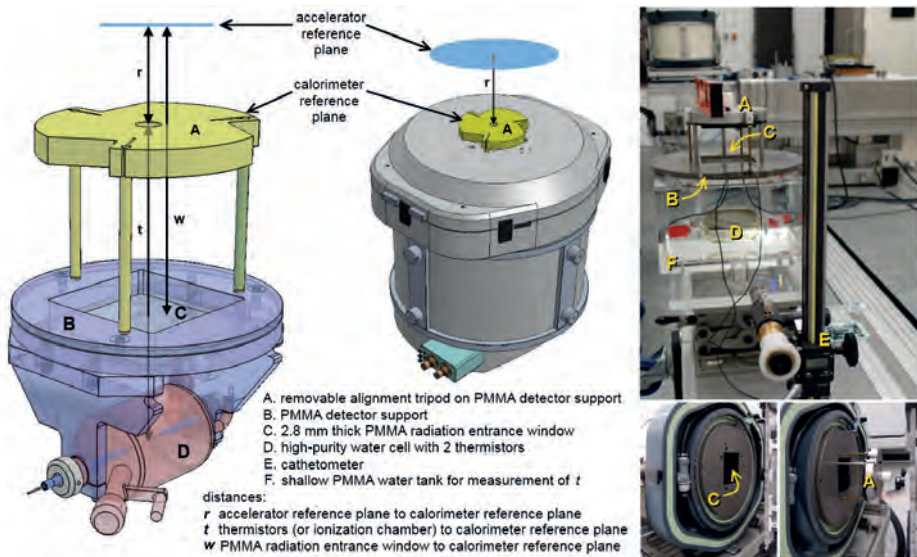
Figure 2-3. Illustrations of the removable alignment tripod (A) on top of the 'PMMA detector support' (B) with the thermistor inside the HPC placed at a depth of 10 cm (D). The photos on the right show the cathetometer (E, top photo) measurement set-up with PMMA water tank (F) and the calorimeter with thermostat lid open (bottom photos) at the accelerator facility of the National Physical Laboratory in Teddington (United Kingdom).

This was done for the worst-case-scenario with the cell in air with larger difference in material refractive indices than in water. These measurements were performed with a fixed in-house, laser-interferometer based cathetometer where a needle-pointer in air was repeatedly covered by the glass cell while the change in vertical tip position was optically measured. The effects of glass cell in air were found to be negligible within the Type A standard uncertainty of 10 μm. The standard uncertainty of both the measurement of the thermistor probe position to the source reference plane and depth in water is better than 0.10 mm.

2.2.5. Calorimeter corrections

2.2.5.1. Heat transfer correction
Heat transfer effects are caused by undesired heat flow due to radiation-induced temperature gradients and excess temperature rise of non-water materials. The latter is caused by differences in specific heat capacity, density and absorbed-dose between non-water materials and water. The total effect depends on materials and geometries, pre-drift, heat-drift, and post-drift times including the applied fit procedures. Heat transfer

effects are described by various authors (e.g. Domen 1994, Ross and Klassen 1996, Krauss and Roos 1998, Krauss 2002, 2006a) and can be described as a correction for conductive heat transfer, k_C, based on the relative excess temperature, R_{XS}:

$$k_C = (1 + R_{XS})^{-1}. \qquad (2.2)$$

R_{XS} is the ratio of excess temperature to the ideal (zero excess temperature, $R_{XS} = 0$, and conduction absent) radiation-induced temperature change (i.e. $D_w/c_{p,w}$) and is determined by finite element simulation of repeated calorimeter runs using COMSOL Multiphysics (version 5.0 at the time of these simulations used for the study of correction factors). The total excess temperature can be split into three components, excess temperature due to:

1. dose gradients (xy&pdd);
2. the non-water materials of the HPC (hpc);
3. the non-water materials of the probes (probes).

For each individual component the relative excess temperature is calculated, $R_{XS,xy\&pdd}$, $R_{XS,hpc}$ and $R_{XS,probes}$, which are treated separately before superimposing them, thus $R_{XS} = R_{XS,xy\&pdd} + R_{XS,hpc} + R_{XS,probes}$. For each component, the time dependent relative excess temperature is extrapolated to mid-run in the same way as a water calorimeter measurement (illustrated in Figure 2-5). Similar methods are described by various authors (e.g. Seuntjens and Palmans 1999, Palmans 2000, Krauss 2002, 2006a). Note that in this study, effects due to excess temperature rise outside the HPC as a result of the chemical heat defect are considered to be negligible.

Two different geometrical models have been defined; a quarter 3D model, which contains a water volume, a phantom wall, insulation and air spaces, a glass cell and a simplified thermistor probe (glass only), and a detailed 2D cylindrical symmetric model, which contains a partial water volume, the HPC and a detailed probe geometry, including thermistor, glue and Pt-alloy wires and. Both models are illustrated in Figure 2-4.

The 3D model is used to calculate the relative excess temperature effects due to lateral and depth-dose profiles, $R_{XS,xy\&pdd}$, based on measured relative dose distributions in a similar way as described by Krauss (2006a). The measured lateral profiles are scaled in size as a function of distance to the source, to account for beam divergence. The use of measured dose profiles is tailored for on-site measurements and allows for quick implementation of new beams without the need to obtain or validate input data from Monte Carlo calculations. In the model, the dose profiles are assumed to be unaffected

by perturbation due to non-water materials in the phantom. Excess temperature in the HPC and probe is switched off as explained below in equation (2.3) and (2.4).

The 2D model is used to calculate the relative excess temperature effects of HPC and probes, respectively $R_{XS,hpc}$ and $R_{XS,probes}$. By splitting up the problem into 3D and 2D models, a high geometrical detail in the small thermistor probes was obtained with sufficient accuracy and calculation time compared to a purely 3D model. k_C obtained with the 3D and the 2D model, both containing a simple probe (i.e. all glass), agreed within 0.03 % and confirmed agreement of the models despite the absence of detailed dose profiles in the 2D model.

The COMSOL model requires for each 2D or 3D grid point with coordinates $\vec{r}$ as an input parameter, the material's volumetric heat source, $Q_{V,m}$ in W m^{-3}, which depends on the water absorbed dose-rate, dD_w/dt in W kg^{-1}, the ratio of absorbed-dose material to water, D_m/D_w, and the material density, ρ_m in kg m^{-3}:

$$Q_{V,m}(\vec{r}) = \rho_m \cdot \frac{dD_w}{dt}(\vec{r}) \cdot \frac{D_m}{D_w}.$$ (2.3)

The temperature rise in material m is proportional to the ratios of absorbed doses material to water, D_m/D_w, and the ratio of specific heat capacities water to material, $c_{p,w}/c_{p,m}$ (equation (4) in Seuntjens and Duane 2009). No excess temperature rise in non-water materials, thus $R_{XS} = 0$, occurs in material m when D_m/D_w equals $c_{p,m}/c_{p,w}$ corresponding to a volumetric heat source $Q_{V,m,Rxs=0}$. In the 3D model, for calculation of $R_{XS,xy\&pdd}$, equation (2.3) is used as the volumetric heat source and the ratio D_m/D_w for non-water materials (i.e. in HPC and all-glass probes) is set to $c_{p,m}/c_{p,w}$ such that the non-water material's excess temperature rise is null. The volumetric heat, responsible only for the excess temperature rise in material m, $\Delta Q_{V,m}$, can then be expressed as:

$$\Delta Q_{V,m}(\vec{r}) = Q_{V,m}(\vec{r}) - Q_{V,m,(R_{XS}=0)}(\vec{r}) = \rho_m \cdot \frac{dD_w}{dt}(\vec{r}) \cdot \left(\frac{D_m}{D_w} - \frac{c_{p,m}}{c_{p,w}} \right).$$ (2.4)

In the 2D model, equation (2.4) is used as the volumetric heat source for $z \leq 5$ cm for calculation of $R_{XS,hpc}$ and $R_{XS,probes}$. The temperature rise in non-water materials then equals the excess temperature, without temperature rise in water.
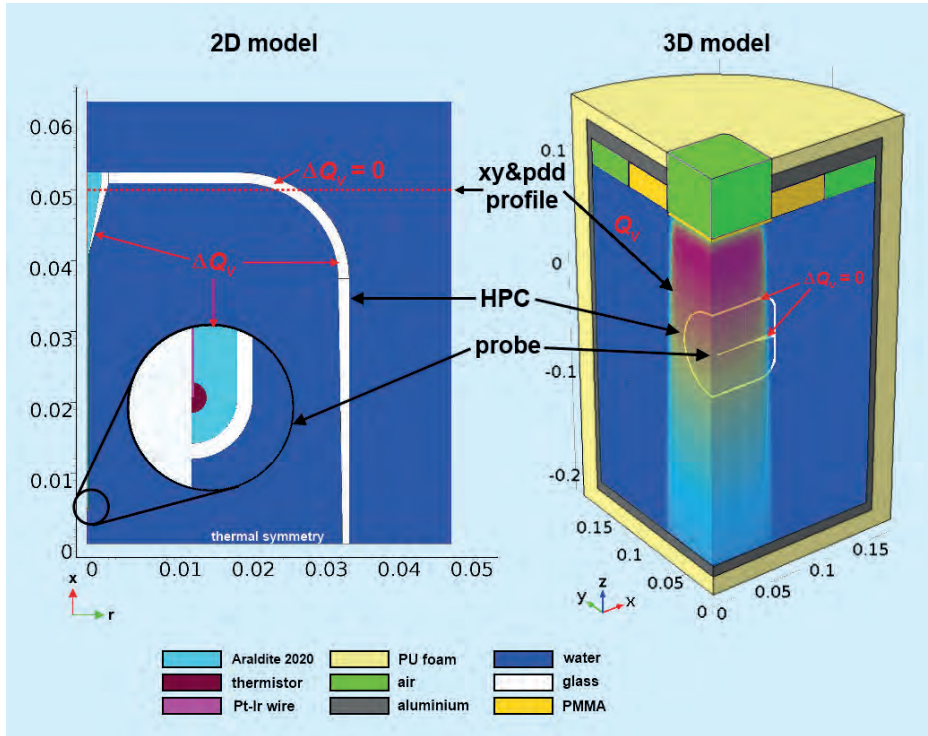
Figure 2-4. The 2D and 3D COMSOL models of the calorimeter with an example 3D dose input for 10 MV photon beams, based on measured lateral and depth dose profiles (right). Dimensions are in meters.

The value of D_m/D_w is based on the physical interaction processes with respect to the dose deposition in the materials. In this study D_m/D_w is estimated as the ratio of the mono-energetic mass stopping power ratios between material m and water, $(S/\rho)_m/(S/\rho)_w$, weighted over the ^{60}Co electron spectrum of the VSL ^{60}Co beam, which was obtained by Monte Carlo simulation. The mass stopping power ratios for mono-energetic electron energies between 0.1 MV and 10 MV were derived from tables available in the online NIST database (Berger *et al* 2005) for glass, PMMA and Pt-alloy and tables created with the PENELOPE Monte Carlo package (Salvat *et al* 2014) for thermistor material. The obtained values for the mass stopping power ratios are: 0.833 for glass, 0.743 for thermistor material, 0.971 for glue (modelled as PMMA) and 0.515 for Pt-alloy wire (90 % Pt - 10 % Ir, modelled as Pt). Repeating the 2D model calculations with both minimum values and maximum values for stopping power ratios in the electron energy range between 0.1 MeV and 10 MeV resulted in a k_C change of less than 0.05 %. This confirms the validity of the use of the ^{60}Co $(S/\rho)_m/(S/\rho)_w$ ratio as measure of D_m/D_w for photon beams with a higher energy. This method is preferred due to the time schedule

and availability of accelerator phase-space files with respect to on-site visits. Effects due to non-Bragg-Gray conditions near small structures are assumed to be negligible.

Heat transport simulations are performed corresponding to the calorimeter measurement sequences. R_{XS} is calculated for 20 subsequent calorimeter runs. The initial situation at the start of the first simulated run is a homogeneous 4 °C water phantom. The relative standard uncertainty on k_C is estimated to be better than 0.18 %. This uncertainty is based on variation of correction factors over the runs, the analyses of similar methods in other studies (Krauss 2006b, Seuntjens and Palmans 1999), data obtained from earlier heat transport calculations performed for the previous water calorimeter (de Prez 2008), difference between the used $(S/\rho)_m/(S/\rho)_w$ values (^{60}Co) and the actual $(S/\rho)_m/(S/\rho)_w$ values for the electron spectra in MV-photon beams and potential convective heat flow.

2.2.5.2. Perturbation corrections

The calorimeter allows for direct calibration of detectors inside its phantom. For this purpose, the only relevant perturbation corrections are those for the presence of HPC and probes, k_{HPC} and k_{probes}, besides the change in water depth, expressed in g cm^{-2}, due to the difference in water temperature. The HPC correction, k_{HPC}, is determined by measuring charge ratios of a small ionization chamber (PTW 31013) placed in a water phantom, repeatedly inside and in absence of the HPC. If k_{HPC} cannot be measured on-site it is determined by interpolation based on (previously) measured values at other beam qualities. k_{probes} is measured in a similar way, by repeatedly placing a thermistor probe near the ionization chamber inside the HPC. The uncertainties of both corrections relate to the relative standard uncertainty of the charge ratio measurements and are estimated to be 0.05 %.

A correction for perturbation and scatter due to the presence of the calorimeter lid and phantom, k_{ph}, is applied for field calibrations, i.e. when the beam's reference D_w per monitor unit is the quantity of interest. k_{ph}, is determined by subsequently measuring ionization chamber signals corrected for T, p, depth and SDD, inside the closed water calorimeter and inside an open calibration water phantom of $30 \times 30 \times 30$ cm^3. The standard uncertainty in k_{ph} is 0.07 %. However, for detector calibrations inside the VSL calorimeter phantom it does not apply.

2.2.6. Other calorimeter correction factors

Other correction factors involve beam radial non-uniformity, k_{rn}, to correct the dose at the position of the probes to that at the beam central axis and facility dependent corrections such as source start-stop effects, $k_{start-stop}$, the source timer error (Andreo *et*

al 2000). The contributing relative standard uncertainty of k_{rn} is based on the magnitude of radial non-uniformity, usually larger for accelerator beams than for ^{60}Co beams, respectively 0.05 % and 0.02 %. The uncertainty for the VSL ^{60}Co start-stop effect is based on repeated ionization chamber measurements and estimated to be better than 0.04 %. Furthermore, measurements are corrected for any small deviations from reference conditions with respect to SDD and depth in water, respectively k_{SDD} and k_d, based on the square law and the effective mass attenuation. Depth in water, in the unit g cm^{-2}, is obtained by taking the mass density of the PMMA entrance window and water at the measurement temperature into account. The uncertainties in both corrections are based on the geometrical standard uncertainty of 0.10 mm and water density. This results in respective contributions of 0.02 % and 0.04 %. The corrections described here are combined in factor k_R in equation (2.1).

The calorimeter heat defect, h, expressed in equation (2.1) for pure water saturated with Argon, is taken to be $-5 \cdot 10^{-4}$ with a standard uncertainty of $2 \cdot 10^{-3}$ based on a study performed by Seuntjens and Palmans (1999).

For a field calibration of the VSL ^{60}Co source in terms of $D_{w,ref}$, an additional correction for exponential source decay, k_{decay} is applied. The standard uncertainty in k_{decay} of 0.02 % is based on the ^{60}Co half-life, 1925.23 (29) days (LNHB 2010).

2.2.7. Radiation-induced temperature change

2.2.7.1. Thermistor resistance measurement.
One of the requirements for on-site measurements of the calorimeter is speed of set-up and operation. Therefore, two high-precision and high-resolution digital multi-meters, DMMs (Agilent 3458A opt 002), are used to measure the resistance of each thermistor. The DMMs are used in their 10 kΩ range and operated in the offset-compensated 4-wire mode, with an integration time of 10 power line cycles (200 ms) for a single resistance measurement. Measurements are triggered every 1000 ms via an external 1 Hz trigger source. The consequence of the DMM settings is that one resistance measurement takes 840 ms during which the first 420 ms the source current (100 µA) is switched off. The 10 kΩ resistance range was calibrated with a standard uncertainty of 10 ppm. Based on their linearity and noise performance (van den Brom *et al* 2007) the standard deviation of the respective DMMs was shown to be approximately 40 nV V^{-1} on the 1 Volt range, internally used for resistance measurements in the 10 kΩ range. When integration times are set optimally, the time between measured values is short and the results of multiple calorimeter runs can be averaged. With this approach a Type A standard uncertainty of
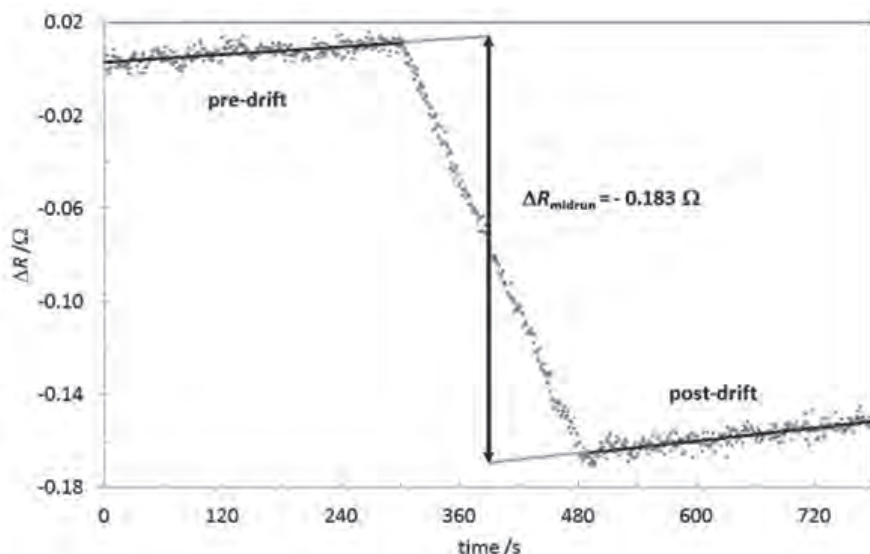
Figure 2-5. Example calorimeter resistance run in a ^{60}Co beam.

0.20 % is achieved over 15 to 100 repeated calorimeter runs, depending on the dose-rate. The overall Type B relative standard uncertainty originating from the DMM resistance calibration and resolution is better than 0.01 %.

A calorimetric measurement run consists of a pre-drift, heat-drift and a post-drift measurement of the thermistor resistance, illustrated in Figure 2-5 and described by e.g. Seuntjens and Duane (2009). Linear fits of the pre- and post-drifts are extrapolated to mid-run to determine the resistance change, ΔR. The post-drift fit starts 10 s after irradiation in order to reduce effects of thermistor excess temperature and overshoot due to fluctuations in beam output as described by (Domen and Domen 2001).

2.2.7.2. Radiation-induced temperature change.
The thermistors are calibrated at the VSL Contact Thermometry Department at 16 temperature points between 2 °C and 6 °C with a standard uncertainty of 2 mK in a calibration bath filled with alcohol. Measurement currents of 5 µA and 10 µA are applied to correct for thermistor self-heat during calibration. As a result of the calibration, an nth order polynomial relation between the thermistor inverse temperature, $1/T$, and the natural logarithm of its resistance, $\ln R$, is given by parameters a_i ($i = 0$ to n, with n equals 2 for this calibration). The material parameter β, in K, of a thermistor is represented by the slope of the $\ln R$ versus $1/T$ curve:

$$\beta = \frac{\mathrm{d}(\ln R)}{\mathrm{d}(1/T)} = -T^2 \cdot \frac{1}{R} \cdot \frac{\mathrm{d}R}{\mathrm{d}T}. \tag{2.5}$$

The individual thermistor β parameter is determined by solving $(\mathrm{d}(1/T)/\mathrm{d}(\ln R))^{-1}$. The thermistor coefficient, α in K^{-1}, is defined as the relative resistance change with thermistor temperature change as given in the following equation:

$$\alpha = \frac{1}{R} \cdot \frac{\mathrm{d}R}{\mathrm{d}T} = -\frac{\beta}{T^2}. \tag{2.6}$$

β is constant over the calorimeter operating temperature interval. To obtain the thermistor temperature an empirical equation based on two parameters (β and the thermistor resistance R_0, valid at a thermistor temperature T_0 of 277.15 K) is generally used:

$$\frac{1}{T} = \frac{1}{\beta} \cdot \ln R + \left(\frac{1}{T_0} - \frac{1}{\beta} \cdot \ln R_0 \right). \tag{2.7}$$

The thermistor radiation-induced temperature change to the first order follows from equation (2.6) and is determined by:

$$\Delta T = \frac{1}{\alpha} \cdot \frac{\Delta R}{R} = -\frac{T^2}{\beta} \cdot \frac{\Delta R}{R}. \tag{2.8}$$

Temperature T in equation (2.7), corrected for thermistor self-heat as explained in section 2.2.7.3, provides the water temperature, needed for determination of the specific heat capacity and density. Following from equation (2.8) the standard uncertainty in the thermistor temperature calibration of 2 mK affects the uncertainty in ΔT by less than 0.01 %. The standard uncertainty in the thermistor β-value is based on the number of temperature calibration points, the linearity of the calibration curve in this range and the β-value stability over the period between calibration and use in the calorimeter. It is estimated to be 0.07 %.

Furthermore, the uncertainty in $\Delta R/R$ is determined by the standard uncertainty contribution due to the DMM calibration and resolution and is smaller than 0.01 %. Internally the DMM measures a voltage-ratio over a well-known reference and the unknown thermistor resistor. The standard deviation of the 1 V-range calibrations between 0.95 V and 1.05 V is 42 nV V^{-1} and 59 nV V^{-1} when applied to the ratio measurement. For a $\Delta R/R$ measurement of $0.2/10^4$ Ω Ω^{-1} (for a typical irradiation of approximately 2 Gy) this results in an additional standard deviation of 0.3 % and a standard uncertainty of the average over 25 calorimetric measurements of 0.06 %, which is incorporated in the Type A uncertainty. Calorimetric measurements are usually repeated until the Type A relative standard uncertainty in $\Delta R/R$ at mid-run is smaller

than 0.20 %. A minimum of 10 calorimeter measurements is performed.

Since the calorimeter utilizes two thermistor probes, the individual D_w and mid-run temperatures can be independently determined for each probe serving as a performance and robustness check of the thermistor calibration and analysis method.

The thermistor temperature change, ΔT, is determined according to equation (2.8) based on a measured relative resistance change with the thermistors present in a magnetic field $B \geq 0$ T, $(\Delta R/R)_B$. Its temperature is elevated above that of the water due to thermistor self-heat, ΔT_{sh}, caused by a dissipated electrical power. A difference between the water radiation-induced temperature, ΔT_w, and ΔT is caused by a change of thermistor self-heat during irradiation. A self-heat correction, k_{sh}, is applied to correct for this effect. In the case of the presence of an external magnetic field, B, an additional correction, k_B, can be applied. The ΔT_w can be expressed as follow:

$$\Delta T_w = \frac{1}{\alpha} \cdot \left(\frac{\Delta R}{R}\right)_B \cdot (k_B \cdot k_{sh}). \tag{2.9}$$

Here, k_{sh} is the thermistor correction in the absence of magnetic field and k_B combines the thermistor magnetic field correction due to a change of thermistor coefficient, a, and its (small but) inherent effect on the thermistor self-heat.

2.2.7.3. Thermistor self-heat.

The difference between the thermistor temperature, T, and the water temperature, T_w, is caused by the thermistor self-heat, ΔT_{sh}. It depends on the power, P in μW, dissipated in the thermistor as illustrated in Figure 2-6. When self-heat induced convection, also referred to as a 'plume' (Domen and Domen 2001), is absent the self-heat is proportional to the dissipated power. This was shown to be valid for thermistor powers, $P < 120$ μW (Cen 2011, Mostert 2014). The thermistor specific self-heat parameter, C_{sh} in mK μW^{-1} is defined by:

$$\Delta T_{sh} = C_{sh} \cdot P. \tag{2.10}$$

C_{sh} is determined by measuring ΔT_{sh} as a function of P at a calorimeter temperature of 4 °C. P is varied by placing known resistors in parallel with the thermistor. The measurements were corrected for calorimeter background drifts. The self-heat parameter was measured with the DMM offset-compensation ON as well as OFF.
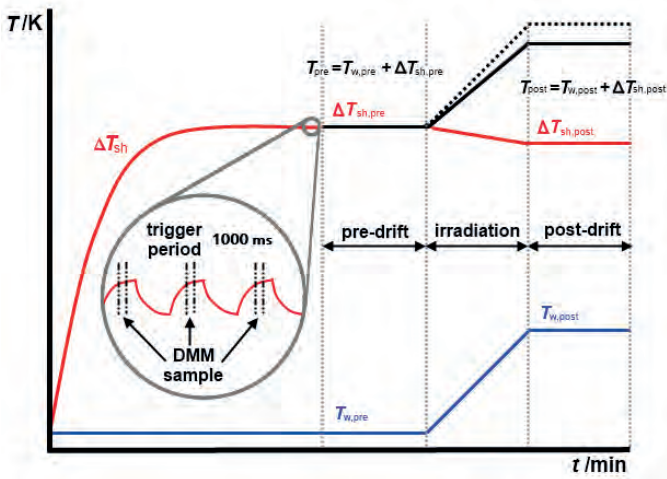
Figure 2-6. Qualitative illustration of thermistor self-heat. The thermistor self-heat, ΔT_{sh} (red line), is the elevation of the thermistor temperature, T (black line), above that of the water, T_w (blue line), as a result of dissipated electrical power, P. At a constant water temperature and after switching the measurement current on, at $t = 0$ min, the thermistor temperature starts to increase until it reaches a constant tem-perature. At this point calorimetric measurements can be started. During a constant pre-drift the self-heat is constant and amounts to: $\Delta T_{sh,pre} = T_{pre} - T_{w,pre}$. During the irradiation, however, with constant thermistor current, its resistance decreases, so does the dissipated power, causing the thermistor self-heat to change to a new value: $\Delta T_{sh,post} = T_{post} - T_{w,post}$. The black dotted line represents the thermistor temperature if the thermistor self-heat would not change.

At constant current, I (where $P = I^2 \cdot R$), the self-heat is proportional to the thermistor resistance and the change of self-heat during a calorimeter run is only caused by the thermistor resistance change during irradiation. Therefore, the thermistor temperature change, ΔT, and water temperature change, ΔT_w, are not equal. In the absence of a magnetic field and with a defined in equation (2.6), the self-heat correction, k_{sh}, is given by (see section 2.5):

$$k_{sh} = 1 - \Delta T_{sh} \cdot \alpha. \tag{2.11}$$

2.2.7.4. Thermistor magneto-resistance effect

When operated in MRI-incorporated treatment equipment, the application of a magnetic field over a thermistor resistance, R, results in a change in measured resistance, R_B, due to the known magneto-resistance (MR) effect, which can be expressed as a relative resistance change, δ_{MR}:

$$R_B = R \cdot (1 + \delta_{MR}). \tag{2.12}$$

With respect to water calorimetry this results in a potential error of the measured radiation-induced thermistor temperature change in the presence of a magnetic field, ΔT_B, when the thermistor's (null Tesla) calibration coefficients are used. The correction for the presence of a magnetic field, k_B, is given by (see section 2.5):

$$k_{\mathrm{B}} = \left(1 + \frac{1}{(1+\delta_{\mathrm{MR}})} \cdot \frac{1}{\alpha} \cdot \frac{\mathrm{d}\delta_{\mathrm{MR}}}{\mathrm{d}T}\right)^{-1}. \tag{2.13}$$

The magnitude of the MR effect for two thermistors was determined by measuring δ_{MR} in a 1.5 T field between the poles of an electro-magnet as a function of temperature between 0 °C and 23 °C. The orientations of the thermistor probes were perpendicular to the magnetic field. The measurements were performed by bringing the thermistor to a stable temperature (background drift smaller than 5 µK s⁻¹) while the electro-magnet was repeatedly switched on and off for short periods of time in order not to disturb the thermal stability by heat generated from the magnet. δ_{MR} and $\mathrm{d}\delta_{\mathrm{MR}}/\mathrm{d}T$ were determined from those measurements.

2.2.7.5. Water specific heat capacity at 4 °C
The specific heat capacity of water, c_p, 4207.5 J kg⁻¹ K⁻¹ at 4 °C (IAPWS 2014) used in equation (2.1) is based on data available in the NIST Chemistry Webbook (Lemmon *et al* 2015) and fitted as a function of temperature with a standard uncertainty of 0.03 %. Wagner and Pruß (2002) estimate the uncertainty of the heat capacity to be ±0.1 %. Interpreted a rectangular distribution, this results in a standard uncertainty of 0.06 % without further reduction as described by (Krauss 2006b). With the uncertainty in the fit, this leads to a combined standard uncertainty for c_p of 0.07 %.

2.2.8. Measurements and calorimeter commissioning

2.2.8.1. Calorimeter thermal characterization.
The calorimeter stabilisation time and basic thermal performance was commissioned by bringing the calorimeter temperature from 20 °C, $T_{\mathrm{w},0}$, down to its operating temperature of 4 °C by applying a temperature step of -16 °C, ΔT_{w}, to both heat exchangers while stirring the water phantom. The water temperature was simultaneously monitored by means of two calorimeter thermistors, mounted inside the HPC at a depth of 5 cm. The temperature response of such system can generally be described as a first order physical system with delay time δ, in h, and time constant τ, in h⁻¹ (see e.g. Cool *et al* 1991):

$$T_{\mathrm{w}} = T_{\mathrm{w},0} + \Delta T_{\mathrm{w}} \cdot \left(1 - e^{-\tau \cdot (t-\delta)}\right). \tag{2.14}$$

Stabilization of the calorimeter temperature is carried out after a working temperature of 4 °C is reached with a temperature drift smaller than 10 µK s^{-1}. To reach sufficient thermal stability for the measurements, the heat exchanger in the bottom of the phantom and the stirrer are switched off and the heat exchanger set-point is adjusted with -60 mK. Stabilization drifts were recorded with and without set-point adjustment and compared to the thermostat's COMSOL models, described in section 2.2.2.

2.2.8.2. Calorimeter measurements in ^{60}Co and MV-photon beams.
The ^{60}Co measurements performed with the new calorimeter were compared with the long-term dose-rate of the VSL ^{60}Co source obtained with the previous water calorimeter. During the first measurements with the new calorimeter, in March 2014, two 20 kΩ thermistors were connected in parallel to one DMM, according to the method of the previous water calorimeter (de Prez 2008). The two 20 kΩ thermistors effectively behave as a single thermistor of 10 kΩ. All other measurements described in this study were performed with two thermistors connected to their own DMM. The 20 kΩ thermistors, connected in parallel to one DMM received each a 50 µA pulsed measurement current (420 ms OFF; 580 ms ON), with a nominal average dissipated power of approximately 29 µW (50 µA at 20 kΩ during 58 % of the time). The 10 kΩ thermistors, connected each to their own DMM, received a 100 µA pulsed measurement current, with a nominal average dissipated power of approximately 58 µW (100 µA at 10 kΩ during 58 % of the time). The thermistor self-heat is based on the measured self-heat parameter, C_{sh}, and the dissipated power as a result of the calibrated DMM measurement current and thermistor resistance during the respective calorimeter run.

Two waterproof PTW 30013 ionization chambers (sn. 007120 and 006213) were calibrated in the VSL ^{60}Co beam and accelerator beams of 6 MV and 10 MV (TPR$_{20,10}$ 0.680 and 0.735). The same HPC filling was used for both calorimeter measurements in the accelerator beams and in ^{60}Co. Calorimeter and ionization chamber measurements in the Elekta Versa HD accelerator were performed in horizontal as well as vertical beams and compared.

Calibration coefficients and k_Q values were determined. k_Q values were compared to values available in existing literature. Ionization chamber measurements were corrected for polarity, saturation effects and beam radial non-uniformity due to the volume averaging effect of the beam over the ionization chamber based on measured lateral dose profiles. The k_Q values for the chambers were based on ^{60}Co and on-site MV-photon calibrations against calorimetric D_w measurements in the same period.
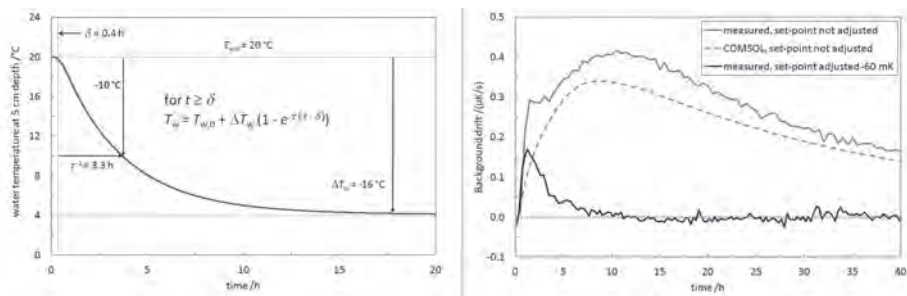
Figure 2-7. A measured calorimeter cooling curve starting at room temperature (left). A background temperature stabilization drift (in µK s^{-1}) at the set calorimeter operating temperature of 4 °C (right).

2.3. Results and uncertainties

2.3.1. Thermostat performance

The left graph of Figure 2-7 shows the measured calorimeter cooling curve from 20 °C to 4 °C (i.e. with heat-exchangers and stirrer switched on). Its response, described by equation (2.14) results in a time constant, τ, of 3.3 h^{-1} and a time delay, δ, of 0.4 h. This means that, in a realistic situation, when the cooling curve starts at approximately 8 °C (the calorimeter phantom is filled with cold water) a temperature drift smaller than 6 µK s^{-1} is reached within 14 hours (i.e. overnight).

Measured and modelled stabilization drifts, in µK s^{-1}, after the stirrer and the bottom heat exchanger were switched off, are shown in the right graph of Figure 2-7 (respectively continuous and dotted grey lines). The COMSOL model's initial conditions were: 4 °C calorimeter interior, including water phantom as a result of the stirrer motion and 20 °C exterior boundary. The stirrer was switched off at the start of the stabilization drift. In general, a good agreement between model and measurement is shown. The calorimeter thermal model predicted a small stabilization drift as a result of a small heat leakage through the thermostat entrance window (see A and C in Figure 2-2).

Based on this effect an improved stabilization drift measured and shown in the same graph (continuous black line) was obtained by adjusting the thermostat temperature with -60 mK just after the phantom heat exchanger and stirrer were switched off. Note that a 0.1 µK s^{-1} drift corresponds to an equivalent absorbed-dose-rate of 0.03 Gy min^{-1}. The right picture of Figure 2-7 shows that, depending on the expected dose-rate, for applications with dose-rates between 15 Gy h^{-1} and 200 Gy h^{-1}, a sufficiently low background drift (i.e. maximal 10 % of the expected radiation-induced temperature drift) is reached within 5 hours after switching off the stirrer.
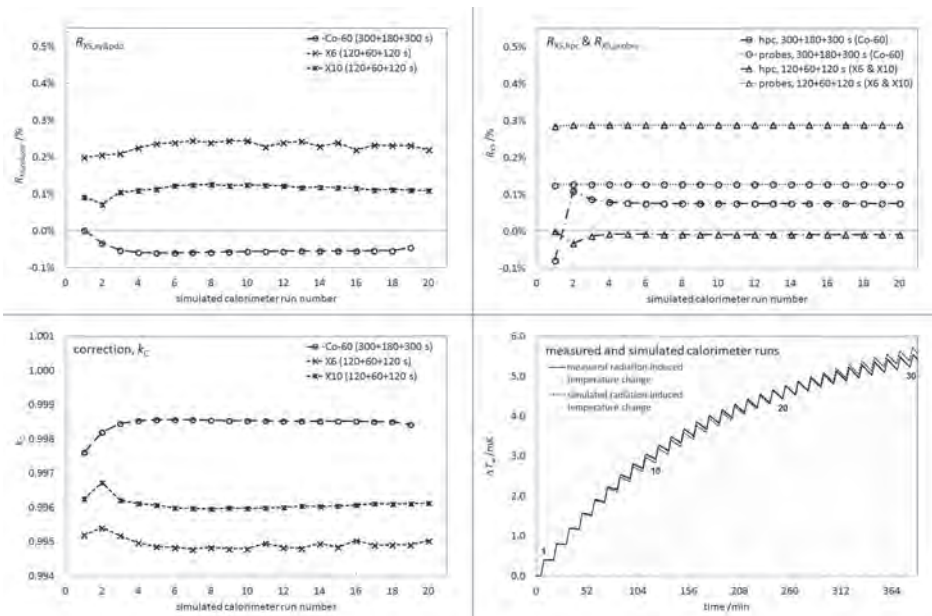
Figure 2-8. The relative excess temperature, R_{xs}, for beams of ^{60}Co (Co-60) at VSL and 6 MV (X6) and 10 MV (X10) at an Elekta Versa HD accelerator (top), and their resulting k_C (bottom left). Thirty simulated (dotted line) and measured (continuous line) calorimeter runs in ^{60}Co beams (bottom-right).

2.3.2. Calorimeter correction factors

The graphs of Figure 2-8 illustrate the relative excess temperature, $R_{XS,xy\&pdd}$ calculated with the 3D COMSOL model (top left), $R_{XS,hpc}$, $R_{XS,probes}$ calculated with the 2D model (top right) for 20 calorimeter runs in ^{60}Co beam and 6 MV and 10 MV-photon beams of an Elekta Versa HD accelerator. In ^{60}Co the simulated pre-drift, heat-drift and post-drift times are respectively 300 s, 180 s and 300 s while in the MV-photon beams the drift times are 120 s, 60 s and 120 s. A constant relative excess temperature due to the probes can be observed, while the effects due to dose profile and HPC become constant after the first four runs. The calorimeter heat transfer corrections are based on the average of the first 20 calculated runs by applying equation (2.2).

The results for heat transfer corrections, k_C, and glass cell perturbation correction, k_{HPC}, are given in Table 2-1. A value for the probe perturbation correction, k_{probes}, was measured in ^{60}Co and showed to be unity within the standard uncertainty of 0.05 %. Likewise, this value is assumed to be unity for MV-photon beams.

The bottom-right graph of Figure 2-8 illustrates a sequence of 30 measured and simulated

^{60}Co calorimeter runs of each 780 s (300 s + 180 s + 300 s). The initial situation at the start of the first simulated run is a homogeneous 4 °C water phantom, which results in a constant temperature drift during the pre-drift of the first run. It shows good agreement between simulated and measured calorimeter runs which support the confidence in the heat transfer calculations and resulting heat transfer corrections. Furthermore, both simulations and measurements appear to evolve to a stable (reasonably flat) pattern.

Table 2-1: Calorimeter correction factors. The relative excess temperature at mid-run, R_{XS}, was averaged over 20 simulated runs.

beam ID	$R_{\mathrm{XS,xy\&pdd}}$ /%	$R_{\mathrm{XS,hpc}}$ /%	$R_{\mathrm{XS,probes}}$ /%	k_C	k_{HPC}
^{60}Co[a]	−0.05	0.07	0.13	0.9985(18)	1.0018(5)
X6[b]	0.23	−0.01	0.29	0.9949(18)	1.0013(5)
X10[b]	0.11			0.9961(18)	1.0011(5)

[a] pre-drift, heat-drift, post-drift times: 300 s, 180 s, 300 s; SDD = 1000 mm; depth = 50 mm
[b] pre-drift, heat-drift, post-drift times: 120 s, 60 s, 120 s; SDD = 1000 mm; depth = 100 mm

2.3.3. Thermistor calibration and correction factors

The calibration parameters and corrections of the thermistors at 4 °C (277.15 K) are presented in Table 2-2. The measurement of the self-heat parameter, C_{sh} at continuous measurement current, resulted in values between 1.61 mK μW^{-1} and 1.90 mK μW^{-1}, similar in magnitude as reported in other studies (Domen and Domen 2001, Krauss 2006b). The ratio in C_{sh} of the offset-compensated versus non-offset-compensated 10 kΩ thermistors was 0.92. This means that during the 200 ms period of the DMM measurement sample, 220 ms after the start of the current 'pulse', the average thermistor self-heat for the same current magnitude is 92 % of the self-heat, reached with a continuous current, i.e. ΔT_{sh} between 155 mK and 172 mK. These values are used to determine the calorimeter self-heat correction, k_{sh}, respectively 1.0063 and 1.0070. The lower power in the parallel connected 20 kΩ thermistors, resulted in a self-heat correction of 1.0031. The relative standard uncertainty in the self-heat correction, k_{sh}, of the 10 kΩ thermistors, is estimated to be 0.07 % and mainly resulting from the uncertainty in the determination of the self-heat parameter, C_{sh}, which is currently estimated to be about 10 % (Mostert 2014).

The results of the measurement of the MR effect, δ_{MR}, as a function of temperature for thermistors VSL13T026 and VSL13T032 is illustrated on the left of Figure 2-9. Values at 4 °C are given in Table 2-2. The right side of Figure 2-9 shows a thermistor background drift, in Ω, at 23 °C where the electro-magnet (1.5 T) was switched on and off repeatedly. No significant increase in temperature due to power dissipated in the electro-magnet was
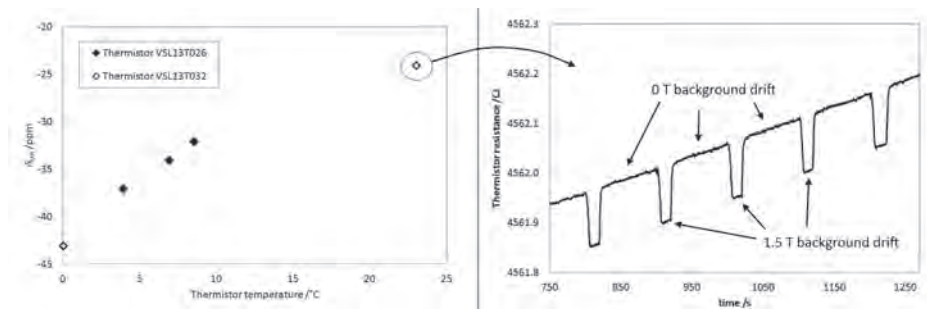
Figure 2-9. The measured magneto-resistance effect of two thermistors, expressed as δ_{MR} in ppm at temperatures between 0 °C and 23 °C (left) and an illustration of the measurements at room temperature (right).

observed at those short intervals. The δ_{MR} was derived from the differences in background drifts. The measurements resulted in a negligible magnetic field correction, k_B, of 1.00002 for both thermistors in a 1.5 T magnetic field, perpendicular to the direction of the probe. The relative standard uncertainty in k_B is estimated to be smaller than 0.01 %. It is expected that also for other field strengths this value is small, however further investigation is needed to confirm this finding.

Table 2-2: Thermistor calibrations and correction factors interpolated for a temperature of 4 °C (277.15 K).

VSL thermistor ID	R_0 [a] /Ω	β [a] /K	DMM offset-compensation[b]				β_{MR} [c] /ppm	$d\delta_{MR}/dT$ [t] /(ppm K^{-1})	k_B [c]
			OFF	ON					
			C_{sh} /(mK μW^{-1})	ΔT_{sh} /mK	k_{sh}				
05T065//067	9773.6	3299.8	1.61	–	72	1.0031	–	–	–
13T023	9700.2	3112.0	1.75	1.60	155	1.0063	–	–	–
13T026	9845.3	3101.8	1.90	1.75	172	1.0070	−36	1.0	1.000
13T032	9393.5	3111.6	–	–	–	–	−40	0.8	1.000

[a] R_0 and β and δ_{MR} at 4 °C (277.15 K), applied according to equation (2.7)
[b] OFF: continuous source current; ON: pulsed source current (100 μA per 580/1000 ms ms^{-1})
[c] interpolated data for a 1.5 T magnetic field perpendicular to the probe direction

2.3.4. Uncertainties

The combined standard uncertainty is determined according to the Guide to the Expression of Uncertainty in Measurement (JCGM 2008). Table 2-3 gives a summary of the uncertainty budget for beam calibrations of ^{60}Co and MV-photons expressed in absorbed dose to water per monitor unit, D_w/MU. The monitor units in ^{60}Co beams are

based on the source timer, in the unit second. The monitor units in MV-photon beams are based on the external transmission monitor ionization chamber. The uncertainty budget presented in Table 2-3 applies for a D_w measurement in the calorimeter phantom. Table 2-4 gives a summary of the uncertainty budget for determination of an ionization chamber calibration coefficient, $N_{D,w,Q}$ in terms of absorbed dose to water at beam quality Q (i.e. ^{60}Co or MV-photons). Table 2-5 gives a summary of the uncertainty budget for determination of a beam quality correction factor, k_Q with beam quality Q_0 being ^{60}Co. Due to correlations, Table 2-3 contributes to the uncertainty in k_Q, shown in Table 2-5. The uncertainty contributions listed in Table 2-3 to Table 2-5 are of type B unless otherwise stated.

2

Table 2-3. Uncertainty budget of an absorbed dose to water measurement in beams of ^{60}Co and MV-photons including MRI-incorporated treatment equipment, applicable inside the calorimeter phantom.

source of uncertainty		u /%	
		^{60}Co	MV
ΔT_w	DMM resistance calibration and resolution, R		< 0.01
	repeated measurement of $\Delta R/R$ per monitor unit, Type A[a]		0.20
	thermistor temperature (at $T = 277.15$ K), T[a]		< 0.01
	thermistor β-value and long-term (1 y) stability[b]		0.07
specific heat capacity of water, c_p			0.07
heat defect, h			0.20
Correction factors	thermistor self-heat, k_{sh}		0.07
	thermistor response in a magnetic field up to 1.5 T, k_B	–	< 0.01
	high-purity cell perturbation, k_{HPC}		0.05
	probes perturbation, k_{probes}		0.05
	heat transfer due to conduction, k_C		0.18
	reference source detector distance (100 cm), k_{SDD}[a,b]		0.02
	reference depth in water, k_{depth}[b]		0.04
	radial non-uniformity at position of probes, k_{rn}[a,b]	0.02	0.05
combined: absorbed dose to water per monitor unit, D_w/MU		0.37	0.37
combined: contribution to k_Q measurements, input for Table 2-5[a]		0.20	0.21

[a] uncertainties contributing to the uncertainty in k_Q, input for Table 2-5
[b] part of the correction to reference conditions, k_R, in equation (2.1)

Table 2-4. Uncertainty budget for the calibration coefficient of a reference type ionization chamber such as the PTW 30013 (McEwen 2010) in ^{60}Co and MV-photons.

source of uncertainty	u /%	
	[60]Co	MV
D_w/MU, combined standard uncertainty from Table 2-3	0.37	0.37
charge measurement, M, per monitor unit (M/MU), Type A		0.10
ion chamber correction for saturation and polarity, k_s and k_p		0.07
correction for p, T, $k_{p,T}$ and relative humidity		0.15
correction to reference SDD (at 100 cm), k_{SDD}		0.02
correction to reference depth in water, k_{depth}		0.04
combined: absorbed dose to water calibration coefficient, $N_{D,w,Q}$	0.42	0.42

Table 2-5: Uncertainty budget for k_Q factors of reference type ionization chamber such as the PTW 30013 (McEwen 2010) in MV-photons of beam quality Q.

source of uncertainty	u /%	
	[60]Co	MV
D_w/MU, contribution to k_Q measurements from Table 2-3	0.20	0.21
charge measurement, M, per monitor unit (M/MU), Type A		0.10
ion chamber correction for saturation and polarity, k_s and k_p		0.07
correction for p, T, $k_{p,T}$ and relative humidity		0.15
correction to reference SDD (at 100 cm), k_{SDD}		0.02
correction to reference depth in water, k_{depth}		0.04
combined: contributions from ^{60}Co and MV-photon calibrations	0.28	0.29
combined: beam quality correction factor, k_Q		0.40

2.3.5. Commissioning measurements

Between March and September 2014 five calorimeter measurements were performed in the VSL ^{60}Co beam. In August 2014, measurements were performed in 6 MV and 10 MVphoton beams of an Elekta Versa HD clinical accelerator at the Netherlands Cancer Institute in Amsterdam (The Netherlands). All measurements were done with new fillings of the high-purity cell except for the measurements before, during and after the measurements at Netherlands Cancer Institute, where the same cell filling was used for the benefit of the k_Q measurements.

In this study, the dose-to-water measurements in ^{60}Co consisted of between 100 and 400 calorimeter runs, resulting in a statistical standard uncertainty (based on the

standard deviation of the mean, SDOM) between 0.13 % and 0.06 % for a single thermistor. The measured ΔT_{w}, with the probes agreed in all cases within 2 statistical standard uncertainties. The mid-run water temperatures, T_{w} (i.e. after application of the thermistor self-heat, ΔT_{sh}) always agreed within 5 mK, which is well within the estimated 16 mK uncertainty of a single probe temperature measurement, mainly caused by the uncertainty in the thermistor self-heat parameter, C_{sh}, see equation (2.10).

Table 2-6 gives the calorimetric absorbed dose-rate to water for ^{60}Co measurements, $D_{w,ref}$ in mGy s^{-1}, obtained with the previous water calorimeter, WCM-01 (November 2002 until December 2013), and the new water calorimeter, WCM-02 (March until September 2014). Measurements WCM-01 contains the earlier heat conduction correction, k_{C} of 0.9984, for WCM-01 calculated with the heat transfer model described by de Prez (2008), which is similar in approach to the model described by Seuntjens and Palmans (1999), and shows excellent agreement with the heat conduction correction k_{C} of 0.9985 calculated in this study despite the fact that the previous model was limited by the defined cylindrical symmetric geometry and absence of lateral and depth dose profiles. This is partly due to the fact that the $R_{XS,xy\&pdd}$ for a sequence of 300 s + 180 s + 300 s as applied for ^{60}Co is very small, shown in this study (see Table 2-1).

Table 2-6 gives the ratio between $D_{w,ref}$ obtained with the new calorimeter WCM-02 and WCM-01. The presented relative standard uncertainties of $D_{w,ref}$, u, for WCM-02 are given in Table 2-3 and for WCM-01 is reported by Kessler *et al* (2009). Additionally, the Type A relative standard uncertainties, u_{A}, of measurements WCM-01 (0.05 % for n = 17) and WCM-02 (0.05 % for n = 5) are given in Table 2-6. An excellent agreement, i.e. within 0.1 %, is shown between the measurements with the new and the previous water calorimeter.

Table 2-7 gives the results of the absorbed dose and ionization chamber measurements in horizontal and vertical beams of the Elekta Versa HD accelerator at Netherlands Cancer Institute (see bottom-right photo of Figure 2-1). Between 10 and 14 calorimeter runs and 5 ionization chamber measurements were performed at each energy. Only for determination of $N_{D,w,Q}$ and k_{Q}, ionization charge readings were corrected for temperature and pressure, $k_{p,T}$, saturation, k_{s}, and polarity, k_{p}, as well as for chamber volume-averaging effect due to beam non-uniformity, k_{v}. No humidity correction was applied since the relative humidity was always within the range 20 % - 80 %. All measurements were corrected to geometrical reference conditions with respect to SDD and depth. The standard uncertainty in the ratios, u, presented between brackets, is based on the statistical standard uncertainty of the measurements including an additional uncertainty for positioning (i.e. the combined uncertainty for two SDD and two depth measurements

amounts to a total of 0.06 %). In the case of ionization chambers, variation in ambient temperature and pressure gradients is estimated to be 0.07 %. The results show good agreement between horizontal and vertical measurements with the calorimeter, in all cases within 2 standard uncertainties and in many cases within 1 standard uncertainty.

The measured k_Q factors are based on the average of the horizontal and vertical measurements and given in Table 2-3. They are compared with available measured values (McEwen 2010) and calculated values (McEwen et al 2014, Andreo et al 2000). From the data in the table it can be concluded that good agreement is reached between the available k_Q values and the values obtained in this study. It must be noted that values reported by McEwen (2010) were measured at slightly different beam quality, $TPR_{20,10}$, however, in both cases this introduces a difference with the values from this study of less than 0.1 %, based on data by McEwen et al (2014).

Table 2-6. D_w measurements in the VSL ^{60}Co beam between 2002 and 2014. The standard uncertainty, u, is of Type A and based on the standard deviation of the mean (SDOM).

calorimeter	period[a]	$D_{w,ref}$[b] $/(mGy\ s^{-1})$	u_A /%	u /%	ratio of WCM−02 to WCM−01
WCM−01	2002 − 2013	10.407	0.05	0.39	1.0009
WCM−02	this study	10.416	0.05	0.37	

[a]17 WCM-01 measurement (2002 until 2013) 5 WCM-02 measurements (2014)
[b] reference date: 1st of January 2015

Table 2-7: Ratios between measurements in horizontal and vertical beams of MV-photons at The Netherlands Cancer Institute in Amsterdam (The Netherlands).

beam	instrument	quantity	ratio horizontal / vertical
	WCM−02	$D_w\ MU^{-1}$	1.0017(24)
6 MV	PTW30013 − 007120	$Q_c\ MU^{-1}$	1.0016(10)
		$N_{D,w,Q}$	1.0001(27)
	PTW30013 − 006213	$Q_c\ MU^{-1}$	0.9991(10)
		$N_{D,w,Q}$	1.0026(26)
	WCM−02	$D_w\ MU^{-1}$	1.0029(26)
10 MV	PTW30013 − 007120	$Q_c\ MU^{-1}$	1.0014(10)
		$N_{D,w,Q}$	1.0015(29)
	PTW30013 − 006213	$Q_c\ MU^{-1}$	1.0002(10)
		$N_{D,w,Q}$	1.0028(26)

Table 2-8. PTW 30013 k_Q values based on the average of two chambers (sn. 007120 and 006213) compared with calculated and measured k_Q values available in literature.

	this study[b]	(Andreo *et al* 2000)[a]	McEwen et al. 2014[a]	McEwen 2010[b]	
$TPR_{20,10}$	k_Q	k_Q IAEA TRS-398	k_Q AAPM TG-51	$TPR_{20,10}$	k_Q
0.680	0.986(4)	0.990(10)	0.990(4)	0.681	0.989(3)
0.735	0.976(4)	0.981(10)	0.981(4)	0.731	0.979(3)

[a] calculated k_Q values; [b] measured k_Q values

2.4. Discussion and conclusion

At VSL, Dutch Metrology Institute, a new transportable water calorimeter was developed as an absorbed dose to water primary standard for ^{60}Co and MV-photon beams including application in MRI-incorporated treatment equipment. The calorimeter is replacing the previous water calorimeter used since 2002. During the design and construction process, between March 2012 and December 2013, special attention was paid to transportability, operation in various beam geometries (e.g. horizontal, vertical beams and patient bores from 70 cm), different beam modalities and application in strong magnetic fields. Thermal models of the calorimeter thermostat were developed to assess its required thermal characteristics before it was built. This process resulted in an innovative compact design with excellent thermal performance, optimally suited for efficient on-site measurements in the radiotherapy clinic. A strong asset of the new calorimeter is its ability to characterize and calibrate detectors in terms of the quantity absorbed dose to water, D_w. For future applications, parts of the calorimeter design can be modified according to purpose (e.g. for application in new beam modalities).

Due to the choice of measurement equipment (two 10 kΩ thermistors each connected to a high-stability DMM) the correction for thermistor self-heat needed to be assessed in detail. A simple relation was established between the thermistor self-heat and the corresponding correction factors. A similar approach was followed for the (less influential) thermistor correction factor to correct the thermistor temperature response for the presence of a 1.5 T magnetic field. The correction for undesired heat flow due to conductive effects was derived using thermal models with relative lateral and depth-dose profile input data.

The calorimeter was commissioned in the VSL ^{60}Co beam and on-site in horizontal and vertical beams of MV-photons. Although the design changed significantly compared to the previous water calorimeter, the agreement between both calorimeters in ^{60}Co was shown to be within 0.1 %, well within the uncertainty of the individual calorimeters. The measurement

results in vertical and horizontal clinical MV-photon beams also showed very good agreement in relation to the reported uncertainty, better than 0.3 %. Additionally, its performance in on-site beams of MV-photons was studied in the key comparison BIPM.RI(I)-K6 and will be reported elsewhere (Picard *et al* 2017). Two waterproof ionization chambers were calibrated directly in the calorimeter. Obtained k_Q factors all showed to agree within 0.5 % with values found in literature, which is within the reported uncertainties.

The uncertainty for absorbed dose measurements in ^{60}Co and MV-photon beams is 0.37 %. Direct calibration of detectors can be carried out with a standard uncertainty of 0.42 % and k_Q factor can be determined with a standard uncertainty of 0.40 %.

In conclusion, a new VSL calorimeter has been developed suitable for on-site measurement in horizontal and vertical beams of ^{60}Co and MV-photons with the unique property that it can be used in the presence of magnetic fields such as are applied in MRI-incorporated treatment equipment.

2.5. Appendix

This appendix gives a derivation for the thermistor corrections due to the presence of a magnetic field and due to the thermistor self-heat, respectively k_B and k_{sh} in equation (2.9). The corrections are used to obtain the water radiation-induced temperature change, ΔT_w, from the measured thermistor's relative resistance change in a magnetic field $B \geq 0$ T, $(\Delta R/R)_B$. In the remainder it is assumed that the R depends only on the thermistor temperature, T. To improve readability, $R(T)$ is written as R, $R_B(T_B)$ is written as R_B and $\delta_{MR}(T)$ is written as δ_{MR}. ΔT_w can be written as:

$$\Delta T_{\mathrm{w}} = \frac{1}{\alpha} \cdot \left(\frac{\Delta R}{R}\right)_B \cdot \left(\frac{\alpha}{\alpha_B} \cdot \frac{\mathrm{d}T_{\mathrm{w}}}{\mathrm{d}T_B}\right). \tag{2.15}$$

Here, α_B is the thermistor coefficient in a magnetic field. α_B can only be obtained by calibration of the thermistor in a magnetic field. However, α is obtained during calibration in the absence of a magnetic field. $\mathrm{d}T_w/\mathrm{d}T_B$ is the thermistor self-heat correction, represented as the derivative of water temperature, T_w, to the thermistor temperature in the presence of the magnetic field, T_B.

Substituting equation (2.6) for a and a_B in the last term on the right-hand side of equation (2.15) yields:

$$\left(\frac{\alpha}{\alpha_B} \cdot \frac{dT_\mathrm{w}}{dT_B} \right) = \left(\frac{\frac{1}{R}\frac{dR}{dT}}{\frac{1}{R_B}\frac{dR_B}{dT_B}} \cdot \frac{dT_\mathrm{w}}{dT_B} \right),$$

$$\left(\frac{\alpha}{\alpha_B} \cdot \frac{dT_\mathrm{w}}{dT_B} \right) = \frac{R_B}{R} \cdot \frac{\frac{dR}{dR_B}\frac{dR_B}{dT_B}\frac{dT_B}{dT}\frac{dT_\mathrm{w}}{dT_B}}{\frac{dR_B}{dT_B}}, \tag{2.16}$$

$$\left(\frac{\alpha}{\alpha_B} \cdot \frac{dT_\mathrm{w}}{dT_B} \right) = \left(\frac{R_B}{R} \cdot \frac{dR}{dR_B} \right) \cdot \frac{dT_\mathrm{w}}{dT}.$$

The product of correction factors k_B and k_sh in equation (2.9) and equation (2.16) leads to the following choice of definition:

$$k_\mathrm{B} \cdot k_\mathrm{sh} = \left(\frac{R_B}{R} \cdot \frac{dR}{dR_B} \right) \cdot \frac{dT_\mathrm{w}}{dT}. \tag{2.17}$$

Where the term between brackets represents k_B: the overall correction for the presence of a magnetic field. dT_w/dT represents the self-heat correction, k_sh, in the absence of a magnetic field. k_B now only depends on the ratio of R_B/R and the ratio of dR/dR_B at a given temperature, i.e. during a calorimeter run. Taking the derivative with respect to R_B for both sides of equation (2.12) and multiplying both sides with R_B/R, results in:

$$\frac{R_B}{R} = \frac{R_B}{R} \cdot R \cdot \frac{d\delta_\mathrm{MR}}{dR_B} + \frac{R_B}{R} \cdot \frac{dR}{dR_B} \cdot (1 + \delta_\mathrm{MR}). \tag{2.18}$$

Substituting R_B from equation (2.12) on the left side of equation (2.18), substituting k_B from equation (2.17) and inserting a from equation (2.6) leads to:

$$(1 + \delta_\mathrm{MR}) = \frac{R_B}{R} \cdot R \cdot \frac{d\delta_\mathrm{MR}}{dR} \cdot \frac{dR}{dR_B} + k_B \cdot (1 + \delta_\mathrm{MR}),$$

$$(1 + \delta_\mathrm{MR}) = k_\mathrm{B} \cdot R \cdot \frac{d\delta_\mathrm{MR}}{dR} + k_\mathrm{B} \cdot (1 + \delta_\mathrm{MR}), \tag{2.19}$$

$$(1 + \delta_\mathrm{MR}) = k_\mathrm{B} \cdot \left(\frac{d\delta_\mathrm{MR}}{dT} \cdot \frac{dT}{dR} \cdot R + 1 + \delta_\mathrm{MR} \right),$$

$$(1 + \delta_\mathrm{MR}) = k_\mathrm{B} \cdot \left(\frac{d\delta_\mathrm{MR}}{dT} \cdot \frac{1}{\alpha} + 1 + \delta_\mathrm{MR} \right),$$

which leads to equation (2.13).

Using, $T_w = T - \Delta T_{sh}$ and inserting a from equation (2.6) the general form of the thermistor self-heat correction, k_{sh}, is given by:

$$k_{sh} = \frac{dT_W}{dT} = 1 - \frac{d(\Delta T_{sh})}{dT} = 1 - \frac{d(\Delta T_{sh})}{dP} \cdot \frac{dP}{dR} \cdot R \cdot \alpha. \qquad (2.20)$$

In this study a constant current is applied through the thermistor to measure its resistance change. In this specific case, the dissipated power equals $P = I^2 \cdot R$ thus $dP/dR = I^2$. Additionally,

$$C_{sh} = \frac{d(\Delta T_{sh})}{dP}. \qquad (2.21)$$

From equation (2.20), (2.21) and (2.10) it follows that with a constant measurement current, the self-heat correction can be expressed as:

$$k_{sh} = 1 - C_{sh} \cdot P \cdot \alpha = 1 - \Delta T_{sh} \cdot \alpha. \qquad (2.22)$$

3

Key comparison BIPM.RI(I)-K6 of the standards for absorbed dose to water of the VSL, Netherlands and the BIPM in accelerator photon beams

Abstract

A comparison of the dosimetry for accelerator photon beams was carried out
between the Dutch Metrology Institute (VSL) and the Bureau International des Poids
et Mesures (BIPM) from 23 September to 20 October 2014. The comparison was
based on the determination of absorbed dose to water for three radiation qualities
of the medical accelerator facilities of the National Physical Laboratory, Teddington
(United Kingdom). After establishing the Draft B, the VSL discovered an error in the
calculation of the correction factor for excess-heat linked to the VSL glass vessel used
in the measurements at the NPL. The comparison results for the revised standard,
reported as ratios of the VSL and the BIPM evaluations (and with the combined
standard uncertainties given in parentheses), are 0.9959(54) at 6 MV, 0.9958(64) at
10 MV and 0.9991(75) at 25 MV. This result is part of the on-going BIPM.RI(I)-K6
series of comparisons.

3.1. Introduction

To compare the absorbed dose to water determinations of the National Metrology Institutes (NMIs) for accelerator photon beams, the Bureau International des Poids et Mesures (BIPM) has developed a transportable standard for absorbed dose to water based on a graphite calorimeter (Picard *et al* 2009, 2010a). A comparison programme was adopted in 2008, currently proposed for twelve NMIs, and is registered in the BIPM key comparison database (BIPM 2019) as BIPM.RI(I)-K6; the comparison protocol (ADWG(I) 2017) is also available in the KCDB. The CCRI decided in 2013 to adopt the value of absorbed dose to water as determined by the BIPM on-site at the NMI as the key comparison reference value (CCRI 2013, Picard *et al* 2013a).

All previous comparisons of BIPM.RI(I)-K6 have been carried out using a calorimetric standard belonging to the same NMI as that providing the accelerator beams. However, the VSL have recently developed a new transportable water calorimeter primary standard (de Prez *et al* 2016a) but has no accelerator at the institute. Therefore, within this framework, a BIPM.RI(I)-K6 VSL comparison was carried out in the accelerator facilities of the National Physical Laboratory (NPL) in Teddington (United Kingdom). The BIPM measurements were made from 23 September to 7 October 2014. In conjunction with the NPL comparison (Picard *et al* 2015a) and VSL calorimeter measurements as well as measurements using the VSL reference standard were made from 7 to 20 October 2014. The VSL calorimeter equipment and electronics were shipped in advance; the BIPM equipment was already on site for the preceding comparison with the NPL.

The comparison between an NMI primary standard and that of the BIPM is established by the determination of absorbed dose to water by each standard at several accelerator radiation qualities. The BIPM absorbed-dose determination, $D_{w,BIPM}$, is made directly at the NMI using the transportable BIPM standard. The NMI determination, $D_{w,NMI}$, is realized during the comparison using one or more NMI reference ionization chambers calibrated in advance. In the case of the VSL, the chamber calibrations were made in conjunction with the other measurements that were carried out in the NPL accelerator beam as described in the following sections. The comparison result for each quality is the ratio and its associated uncertainty $u_c(R)$:

$$R = \frac{D_{w,NMI}}{D_{w,BIPM}}. \tag{3.1}$$

After the establishment of the Draft B comparison report, VSL discovered an error in their calculation of the correction for conductive heat flow, k_C. A detailed description of

the error and its correction is given in section 3.7. The results presented in this report have been corrected for this error.

In view of the nature of the error and the explanation given by the VSL, it was decided in this particular case to seek approval for the revised report. All the previous participants in this ongoing comparison received the modified report and confirmed their acceptance of the new result of VSL, as prescribed in the document Measurement comparisons in the CIPM-MRA (CIPM 2016). Further agreement was also requested and received from the KCWG(I), the CCRI(I) and from the CCRI.

3.2. Description of standards and measurements

3.2.1. The VSL determination of absorbed dose to water

The Dutch standard for absorbed dose to water is a water calorimeter, recently re-designed and described in (de Prez *et al* 2016a). The calorimeter consists of a cylindrical aluminium water phantom with an internal diameter of 308 mm and a wall thickness of 6 mm, surrounded by a temperature thermostat. Designed for use in both vertical and horizontal beams, it is first positioned as for vertical use before being rotated if necessary. It is closed by an aluminium lid containing a 2.8 mm thick PMMA entrance window in contact with the water surface. A high-purity water cell, containing ultra-pure argon-saturated water and two thermistor probes, is suspended from the phantom lid. The temperature thermostat surrounding the water phantom maintains a background temperature drift below 1 μK s^{-1}. The rotation of the thermostat and phantom through 90° for use in horizontal beams preserves the detector position, beam geometry, scatter and attenuation. The calorimeter high-purity cell can be replaced by an ionization chamber when transferring the measured absorbed dose to a secondary standard.

The beam enters the calorimeter in the centre of the removable lid through a 110 mm square entrance window (see Figure 3-1) and subsequently passes through several layers of polyurethane (PU) foam (in total 18 mm) and several layers of aluminium (in total 0.5 mm). No correction is applied for the entrance window on the assumption that it does not significantly influence the beam quality (that is, they do not significantly change the ionization chamber calibration coefficient).

The reference point of the water calorimeter is positioned on the beam axis at a depth of 10 g cm^{-2} (i.e. passing through 2.8 mm of PMMA with a density of 1.19 g cm^{-2}, then 96.7 mm of water) and the absorbed dose is determined by measuring the radiation-induced temperature rise in water, ΔT_w. The absorbed dose to water $D_{w,VSL}$ is expressed as:

$$D_{w,VSL} = \Delta T_w \cdot c_{p,w} \cdot (1-h)^{-1} \cdot k_P \cdot k_C \cdot k_R, \qquad (3.2)$$

where $c_{p,w}$ represents the specific heat capacity of water at constant pressure and h the chemical heat-defect caused by radiation-induced exo- or endo-thermic chemical reactions. Correction factors compensate for the perturbation due to the presence of non-water materials (mostly glass) k_P, and for deviations from the reference conditions k_R. A correction for conductive heat flow, k_C, was determined using finite element methods applied to a simplified geometry. The calculations included information on measured lateral dose profiles provided by the NPL and depth dose profiles generated from $TPR_{20,10}$ data. The water calorimeter is operated at 4 °C, the temperature providing maximum water density and hence for which convective effects are negligible. The transfer chamber is measured in the calorimeter phantom at room temperature. These measurements are corrected for a change in water depth, in units g cm^{-2}, due to the temperature difference.

The radiation-induced temperature change is measured by means of two thermistor probes connected to commercially available high accuracy, high stability digital multi-meters (DMMs), calibrated and characterized in the VSL Electricity Department. Corrections are applied for self-heating due to the power dissipated by the DMMs in both thermistors.

3.2.2. The BIPM determination of absorbed dose to water

3.2.2.1 Description of the calorimeter system
The BIPM absorbed-dose graphite calorimeter is described by Picard *et al* (2009, 2010a). No electrical heating is employed, but rather the specific heat capacity of the graphite core, $c_{p,c}$, has been determined previously in a separate experiment (Picard *et al* 2007). Quasi-adiabatic conditions are achieved by irradiating the core in a graphite jacket that is smaller than the radiation field, resulting in a relatively uniform dose distribution in the jacket. This arrangement is mounted in a PMMA vacuum container with graphite build-up plates to centre the core at the reference depth of 10 g cm^{-2}. The mean absorbed dose, D_c, in the graphite core is determined using:

$$D_c = c_{p,c}(T) \cdot \Delta T \cdot k_{imp}, \qquad (3.3)$$

where ΔT is the temperature rise in the core and k_{imp} corrects for non-graphite materials in the core.
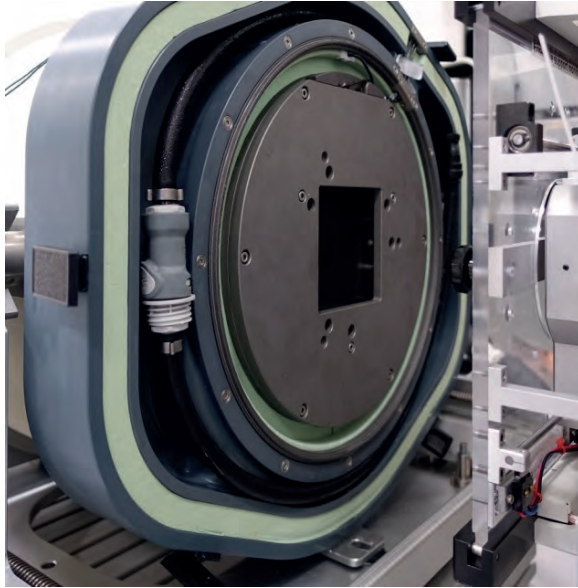
Figure 3-1. The VSL water calorimeter placed in the NPL accelerator beam. Its outer thermostat cover has been removed to determine the position of the VSL PMMA phantom window. The position of the thermistor probes in relation to the phantom surface was measured outside the calorimeter.

Two nominally identical parallel-plate ionization chambers with graphite walls and collector, similar in design to the existing BIPM standards for air kerma and absorbed dose to water, were fabricated for the determination of the absorbed dose to water from the measured absorbed dose to the graphite core. The first chamber is housed in a graphite jacket, nominally identical to the calorimeter jacket, and is irradiated in the same PMMA support and phantom arrangement, albeit without evacuating the phantom. The second chamber is mounted in a waterproof sleeve and irradiated at the reference depth in water. These measurement arrangements are represented schematically in Figure 3-2.

The method adopted by the BIPM combining calorimetric and ionometric measurements with Monte Carlo simulations to determine the absorbed dose to water is described in detail in (Burns 2014) and has been applied in a number of previous comparisons (Picard *et al* 2010a, 2011b, 2013b, 2013c, 2014, 2015a, 2015b). The absorbed dose to water, $D_{w,BIPM}$, is evaluated as:

$$D_{w,BIPM} = D_c \cdot \frac{Q_w}{Q_c} \cdot \left(\frac{D_w}{D_c}\right)^{MC} \cdot \left(\frac{D_{cav,c}}{D_{cav,w}}\right)^{MC} \cdot k_{r\,n,BIPM}, \tag{3.4}$$
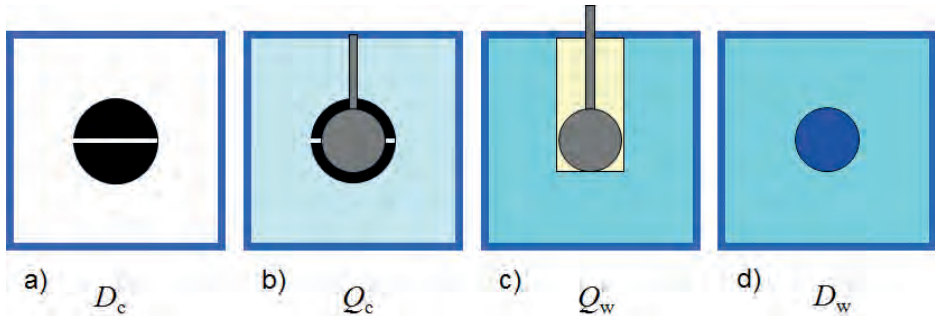
Figure 3-2. Schematic representation of the three different measurement situations (a, b and **c**) and four Monte Carlo models (a, b, c and d). All measurements are made in a cubic PMMA phantom, here represented by the dark blue square. a) The calorimeter is used in vacuum and D_c is both measured and calculated. b) The graphite core is replaced by the transfer ionization chamber at atmospheric pressure. The ionization charge in graphite, Q_c, is measured and the corresponding cavity dose, $D_{cav,c}$ calculated. c) The ionization chamber is placed in a waterproof sleeve inside a similar phantom filled with water. The ionization charge in water, Q_w, is measured and the corresponding cavity dose, $D_{cav,w}$, calculated. For calculation of d), the mean absorbed dose to water, $D_{w,BIPM}$, in the absence of the chamber and sleeve is calculated for a water detector with the same dimensions as the cavity. It follows that a correction factor $k_{r\,n,BIPM}$ is required for the radial non-uniformity of the radiation field over this dimension, measured for a homogeneous water phantom.

where

D_c	-	measured absorbed dose to the graphite core;
Q_c	-	ionization charge measured when the transfer chamber is positioned in the graphite jacket, replacing the core;
Q_w	-	ionization charge measured when the transfer chamber is positioned in water;
$\left(\dfrac{D_w}{D_c}\right)^{MC}$	-	calculated ratio of absorbed dose to water and to the graphite core using Monte Carlo simulations;
$\left(\dfrac{D_{cav,c}}{D_{cav,w}}\right)^{MC}$	-	calculated ratio of cavity doses in graphite and in water using Monte Carlo simulations;
$k_{r\,n,BIPM}$	-	measured correction for radial non-uniformity in water.

In abbreviated form, $D_{w,BIPM}$ can be expressed as:

$$D_{w,BIPM} = D_c \cdot \frac{Q_w}{Q_c} C_{w,c} \cdot k_{r\,n,BIPM}, \qquad (3.5)$$

where $C_{w,c}$ represents the total Monte Carlo conversion factor.

Table 3-1. Results of the calculations of the conversion factor $C_{w,c}$ for the BIPM calorimeter using the Monte Carlo code PENELOPE (Salvat *et al* 2009), calculated using the phase-space files supplied by the NPL. Also given are the measured and calculated values for the $TPR_{20,10}$. The values in parenthesis represent the combined standard uncertainty of the calculations based on (Burns 2014).

beam quality	measured $TPR_{20,10}$	calculated $TPR_{20,10}$	$C_{w,c}$ [a]
6 MV	0.682	0.683(1)	1.1218(22)
10 MV	0.733	0.732(1)	1.1301(25)
25 MV	0.800	0.804(1)	1.1428(27)

[a] These values for $C_{w,c}$ include the use of chamber calo-5 in water, which has a different design of PMMA sleeve from chamber calo-6 used for previous comparisons in the series. Consequently, the values are lower than those calculated for previous comparisons by the factor 0.9989 at 6 MV and 10 MV and by 0.9995 at 25 MV.

3.2.3.1. Monte Carlo simulations

The Monte Carlo calculations are described in detail in (Burns 2014) and make use of the PENELOPE code (Salvat *et al* 2009). As noted in the preceding section, four geometries are simulated, and the accuracy of the method relies on the symmetry of the geometries. A novel aspect of this is the use of a disc-shaped transfer chamber whose total graphite thickness on-axis is the same as that of the calorimeter core. Very few of the geometrical bodies appear in only one of the four simulations so that the fine details should not need to be simulated. Nevertheless, a very detailed geometrical model was constructed. Similarly, although detailed electron transport should not be essential for the same reasons, sufficient detail was used to permit the cavity dose to be calculated in a way that gives the same results as a full calculation using event-by-event electron transport, as demonstrated in an earlier work (Burns 2006). Reference (Burns 2014) includes a detailed uncertainty analysis for the calculation of the conversion factor $C_{w,c}$.

The phase-space files of incident photons at 80 cm from the source were supplied to the BIPM by the NPL, calculated using the EGSnrc system (V4-r2.3.2) and associated BEAM user-code (Kawrakow *et al* 2019, Rogers *et al* 2015). In total, 2.4×10^7 independent photons were used, distributed for convenience in 24 files in the format specified in Appendix VI of the comparison protocol (ADWG(I) 2017). The multiple use of each photon until the statistical uncertainty is optimized is also discussed in the protocol.

The phase-space files are used to calculate $C_{w,c}$ and the corresponding $TPR_{20,10}$, calculated for a detector of radius 3 mm. To account for any difference between the calculated $TPR_{20,10}$ and the measured value, the following procedure is adopted. The calculated values for $C_{w,c}$ accumulated so far for the BIPM.RI(I)-K6 comparison series (17 beam

qualities in total) are plotted as a function of the corresponding calculated $TPR_{20,10}$ (see Figure 3-7). A quadratic fit to these data shows an r.m.s. deviation within the standard uncertainty of each calculation (typically 0.06 %). Using this quadratic fit, the value for $C_{w,c}$ corresponding to the measured $TPR_{20,10}$ is extracted and used for the BIPM determination of absorbed dose in this beam. Any significant difference between the measured and calculated values for the $TPR_{20,10}$ is included as an uncertainty component.

The results for $C_{w,c}$ are listed in Table 3-1 along with the measured and calculated $TPR_{20,10}$. The figures in parentheses for the calculated parameters represent the combined standard uncertainty in the trailing digits based on the analysis presented by Burns (2014), including components arising from the simulation geometries, input spectra, radiation transport mechanisms and cross-section data used. The statistical standard uncertainty for each value for $C_{w,c}$ is around 0.05 %.

3.2.4. Measurements in the MV-photon irradiation facility at the NPL

3.2.4.1. Experimental set up for the key comparison
The comparison was carried out at the NPL accelerator facility, housing an Elekta Synergy linear accelerator. The gantry was fixed for horizontal irradiation for all the measurements for this comparison. The SDD was set using a graduated rod and the centre of the front face of the graphite calorimeter core; the ionization chambers were aligned with the centre of the beam using two laser systems. The VSL calorimeter and ionization chamber were positioned at the same SDD using a separate positioning device associated with the VSL calorimeter. The accelerator head is equipped with a multi-leaf collimator, used to define the radiation field. Accelerator stability and beam uniformity checks are performed routinely as part of the quality assessment plan for the accelerator.

The comparison measurements were made in three of the seven photon beams available on the accelerator: 6 MV, 10 MV and 25 MV, whose measured tissue-phantom ratios $TPR_{20,10}$ are given in Table 3-1. The absorbed dose rate was chosen around 2 Gy min^{-1} at the depth of maximum dose and the pulse repetition frequency was 200 Hz at 6 MV and 100 Hz at 10 MV and 25 MV, i.e. the same parameters as used for the BIPM comparison with the NPL (Picard *et al* 2015a).

All measurements were made at 10 g cm^{-2}, in line with the Dutch code of practice adopted for high-energy photon beams (Aalbers *et al* 2008). Except for the VSL phantom, a cubic PMMA phantom of side length 30 cm was used for measurements made in water. The reference point for each ionization chamber was positioned at an SDD of 100 cm;

the density of the 3.81 mm PMMA entrance window and of the water were taken into account. The field size in the detector plane was 10×10 cm².

The ionization chamber readings were normalized to the reference temperature of 20 °C and pressure of 101.325 kPa chosen for the comparison. No correction was made for air humidity; the relative humidity in the accelerator laboratory remained within the interval 20 % to 80 % throughout the comparison measurements. An irradiation time of 60 s was used for all measurements with the BIPM calorimeter, the BIPM transfer chambers and the VSL reference chamber.

A mechanical table designed by the NPL for its accelerator laboratory was used as support for the BIPM and VSL calorimeter phantoms, and the water phantom in turn. It was adjustable in three dimensions with a reproducibility better that 0.2 mm.

3.2.4.2. Beam monitoring and measurement system
The indicated dose from a clinical accelerator is not normally sufficiently stable in time for comparisons of primary standards when used with its internal transmission monitor alone. For this reason, the BIPM used a commercial parallel-plate transmission chamber to serve as a monitor during irradiation and a reference class thimble chamber (type NE 2571 serial number 2106) to determine the stability of the transmission monitor. All ionization chamber current measurements are ultimately normalized to the reading of the thimble chamber.

The regular use of the thimble monitor chamber to calibrate the transmission monitor, as well as the need to pre-irradiate all chambers, presents a problem when the BIPM calorimeter is in place because the calorimeter must be shielded during these measurements to avoid unnecessary heating of the core. This was achieved for previous comparisons by manually positioning a lead block, 5 cm in thickness, between the calorimeter and the external transmission monitor when calibrating the transmission monitor or pre-irradiating the chambers. This block produces significant backscatter into the external monitor, increasing its response by up to 40 % depending on how close it is to the transmission chamber. Therefore, to maintain the consistency of the measurements and correctly determine the ratio D_c/Q_c, this shielding block is also positioned during the corresponding monitoring for the measurement of Q_c. The block is removed when not calibrating the transmission monitor or pre-irradiating the chambers.

However, manual positioning of the block introduces some variation in backscatter, as well as the need to enter the irradiation area many times. For this reason, the BIPM

transmission and thimble monitor chambers, and a 3 cm thick tungsten block, replacing the previous in lead, were mounted on a newly-developed motorized and remote-controlled support, fixed to a shadow tray, cf. Figure 3-3. This device allows the thimble chamber and tungsten block to be moved into the beam when the transmission monitor is to be calibrated and moved out again for calorimetry or ionometric measurements. This system was shown not only to enable a very high reproducibility of positioning, but also to save time by avoiding repeated entry into the irradiation area. The new support incorporates a probe to measure the temperature close to the chambers.

The monitoring procedure was as follows. Before, and in some cases after, each series of measurements made by the BIPM or the VSL, the thimble chamber, with its Delrin (Polyoxymethylene, POM) build-up cap, was positioned in the beam about 1 cm downstream from the external transmission monitor and used to calibrate the latter. In effect, the transmission chamber serves as monitor during each series of measurements while the thimble chamber is used to transfer the monitoring between series of measurements. In this way the uncertainty associated with the monitoring is included in the reproducibility of the repeated measurements for each device, that is, in the statistical standard uncertainties (see Table 3-5, Table 3-6 and Table 3-7).

It follows that it is the thimble chamber that is used to link the BIPM and VSL dose measurements. That is, over the course of the comparison, this chamber was calibrated using both the BIPM graphite calorimeter and the VSL water calorimeter (de Prez *et al* 2016a). The thimble chamber was also used for a robust determination of the charge ratio Q_w/Q_c for the BIPM and VSL transfer chambers.

All measurements using the VSL transfer standard in the BIPM phantom were made using the VSL measurement system but using the BIPM measurements of air temperature and pressure. The VSL ionization measurements were synchronized with the BIPM external transmission chamber measurements. For the BIPM transfer chambers, the BIPM data acquisition system was used, air pressure and temperature being measured using the BIPM detectors.

No shield is needed during the monitoring for measurements in the water phantom, that is, for the measurement of Q_w using the BIPM chamber and for the realization of $D_{w,VSL}$ using the VSL reference chambers. Nevertheless, the tungsten block was systematically inserted for all thimble chamber monitoring measurements in order to correctly determine the ratio of cavity doses, Q_w/Q_c.
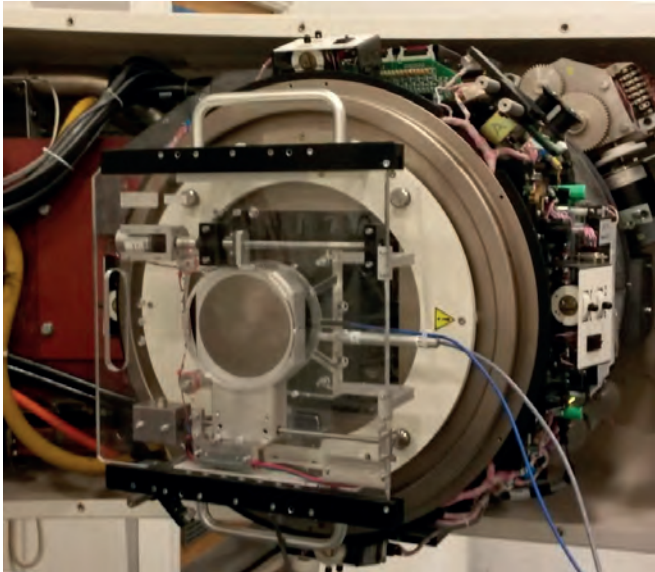
Figure 3-3. The BIPM monitoring and shielding assembly fixed on a shadow tray. This device allows remote and simultaneous movement of the thimble chamber and tungsten block in or out of the beam, resulting in high reproducibility of positioning. The reduced need to enter the irradiation area saves time and improves radiation protection.
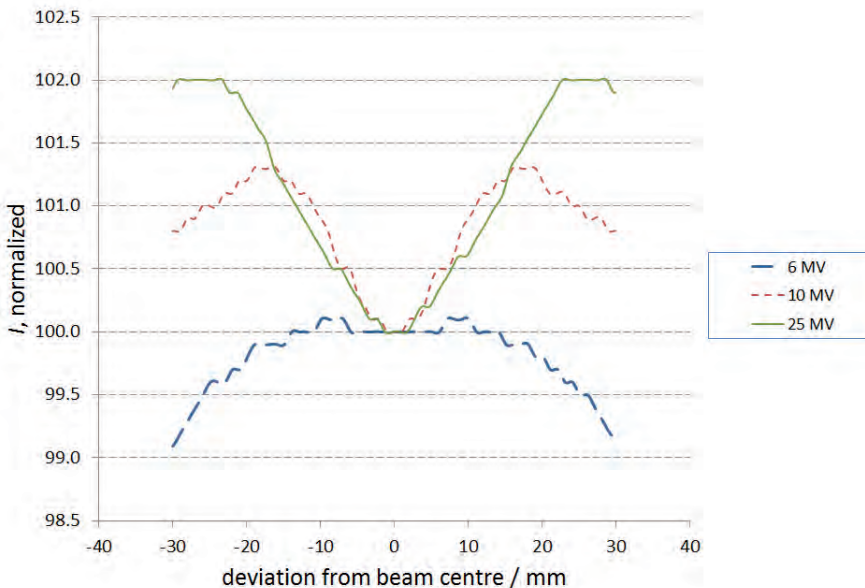
Figure 3-4. Beam profile in the vertical direction measured by the NPL at 6 MV, 10 MV and 25 MV. The measured current I is normalized to the dose at the centre.

3.2.4.3. VSL calibration of reference chamber

One PTW 30013 thimble ionization chamber, serial number 007120, was chosen as the VSL reference standard for the realization of the absorbed dose to water. The chamber was calibrated at each beam quality against the VSL water calorimeter, by placing the chamber into the VSL water calorimeter phantom. Additional measurements were also carried out by the VSL in the NPL accelerator beam to determine the correction factors for recombination and polarity effects. An irradiation time of 60 s was used for all measurements with the VSL calorimeter and the VSL reference chamber.

3.2.4.4. Beam profile

The BIPM calorimeter core is 45 mm in diameter and, depending on the beam profile, the correction factor for radial non-uniformity $k_{\mathrm{r\,n,BIPM}}$ can be significant. This is particularly true for clinical accelerators where the uniformity over a 10 cm × 10 cm field can be compromised somewhat so that uniformity specifications are met for all field sizes. The NPL had previously determined the beam profile in the horizontal and vertical directions for each beam quality using an IBA Blue Phantom 2 with a pinpoint chamber. The vertical profiles of the three beams are shown in Figure 3-4. The observed non-uniformity of the profiles is not unusual for clinical accelerator beams.

The beam profiles measured by the NPL were used to determine the values for $k_{\mathrm{r\,n,BIPM}}$ used for this comparison. A cubic spline was fitted to each of the NPL horizontal and vertical profiles. The correction factor $k_{\mathrm{r\,n,BIPM}}$ for a given curve is determined by dividing the calculated (fitted) response at the centre by the mean response (weighted by radius) over a diameter of 45 mm. Each value for $k_{\mathrm{r\,n,BIPM}}$ listed in Table 3-2 is the mean of the evaluations in the horizontal and vertical directions. The stated standard uncertainty is an estimate including the difference between the horizontal (cross-line) and vertical (in-line) scans.

**Table 3-2.** Correction factors for radial non-uniformity, $k_{\mathrm{r\,n,BIPM}}$, measured for a diameter of 45 mm at a depth of 10 g cm^{-2} and for a source-to-detector distance of 100 cm. The standard uncertainty in the last digits is indicated in parenthesis. The VSL correction $(k_{\mathrm{r\,n,horizontal}}/\,k_{\mathrm{r\,n,vertical}})_{\mathrm{VSL}}$ reflects the difference in projected beam profile on the chamber depending on its orientation.

nominal accelerating voltage / MV	$k_{\mathrm{r\,n,BIPM}}$	$(\,k_{\mathrm{r\,n\,,horizontal}}/\,k_{\mathrm{r\,n\,,vertical}})_{\mathrm{VSL}}$
6	1.0019(14)	1.0002(6)
10	0.9918(33)	1.0011(7)
25	0.9915(51)	1.0024(9)

The beam profiles measured by the NPL were also used to determine the corrections in respect to radial non-uniformity applied by the VSL for the determination of a) the VSL chamber calibration factor in horizontal orientation versus b) the BIPM comparison measurements where the chamber was positioned in vertical orientation. The value of the inline non-uniformity corrections for the 6 MV, 10 MV and 25 MV NPL beams, determined for the VSL reference chamber were respectively 1.0000(4), 0.9952(5) and 0.9964(6).

3.3. Results and uncertainties

Typically, after setting up a given BIPM device (calorimeter, transfer chamber in graphite or water) and selecting the radiation quality, the monitors were pre-irradiated. Then the BIPM thimble monitor was used to calibrate the transmission monitor, the BIPM device was measured and finally the transmission monitor re-calibrated. Each measurement series normally involved between seven and ten measurements. For a given BIPM device, the radiation quality was interchanged between 6 MV, 10 MV and 25 MV and this cycle was repeated three times before switching to a new BIPM device. This entire procedure, including setting up, was repeated for each device at a later date to determine the degree of reproducibility. Thus, in total each quality was measured typically five times for each device. For calorimetric measurements, when possible, the calorimeter was set up on a Friday evening to benefit from the weekend for temperature stabilization and to obtain an adequate vacuum.

When the BIPM measurements in water were to be made to determine Q_w in equation (3.5), the ionization chamber placed in a waterproof PMMA sleeve (identified as calo-6) failed. Fortunately, a well-characterized back-up chamber in a different PMMA sleeve (identified as calo-5) was available for these measurements. The Monte Carlo conversion factor $C_{w,c}$ was subsequently re-calculated to include this change to the sleeve.

3.3.1. Estimation of uncertainties

3.3.1.1. Uncertainty in the determination of $D_{w,VSL}$
The relative standard uncertainties for the VSL determination of the calibration coefficient $N_{D,w,VSL}$ are outlined in Table 3-3 and Table 3-4. These are established for one selected reference ionization chamber used as a transfer standard, based on measurements in water using the VSL primary standard water calorimeter. The combined standard uncertainty of the determination of $D_{w,VSL}$, normalized to the thimble monitor charge Q_{th}, is given in Table 3-5. The Type A uncertainty, attributed to reproducibility, is the

standard deviation of the mean of 5 runs for each chamber at each beam quality. Each run consisted usually of 10 exposures of 60 s duration.

3.3.1.2. Uncertainties in the determination of $D_{w,BIPM}$

The uncertainties for the determination of D_c, normalized to the thimble monitor charge Q_{th}, are listed in Table 3-6. The Type A standard uncertainty of D_c/Q_{th} depends on the time devoted to measurements at the NMI, the temperature stability of the NMI laboratory and the stability of the beam and beam monitoring. The uncertainties associated with the determination of the ratio Q_w/Q_c are listed in Table 3-7. The chamber orientation corrections noted in Table 3-7 were determined in the BIPM ^{60}Co reference beam. The polarity effect for the parallel plate chambers was determined in a previous work where the correction factor for recombination losses in pulsed beams was determined for the BIPM transfer chambers (Picard *et al* 2011a).

Table 3-3: Uncertainties associated with the determination of $D_{w,VSL}$ using the VSL water calorimeter.

uncertainty component	$u(y)/y$ / 10^{-3}
determination of temperature rise (ΔT_w)	2.3
specific heat capacity of water ($c_{p,w}$) at 4 °C	0.7
water heat defect (h)	2.0
corrections for of non-water materials, conductive heat flow and deviations of the measurement conditions from the reference conditions ($k_P \cdot k_C \cdot k_R$)	2.1
combined relative standard uncertainty [$u_c(y)/y$] / 10^{-3}	3.8

Table 3-4. Uncertainties associated with the determination of the calibration coefficient $N_{D,w,VSL}$ of the reference ionization chamber in the accelerator photon beams using the VSL water calorimeter.

uncertainty component	$u(y)/y$ / 10^{-3}
realization of absorbed dose to water, $D_{w,VSL}$	3.8
ionization measurement	0.4
pressure, temperature and relative humidity	1.5
positioning	0.5
radial non-uniformity of beam	0.5
recombination	0.5
combined relative standard uncertainty [$u_c(y)/y$] / 10^{-3}	4.2

Table 3-5. Standard uncertainty components for the determination of the comparison measurement, $D_{w,VSL}/Q_{th}$, in the BIPM phantom in the 6 MV, 10 MV and 25 MV accelerator photon beams. The data are derived using the external transmission monitor.

Type A relative standard uncertainty component	$u_A(y)/y$ / 10^{-3}		
	6 MV	10 MV	25 MV
$Q_{w,VSL}/Q_{th}$ (n = 5)	0.5	1.6	0.6
Type B relative standard uncertainty component	$u_B(y)/y$ / 10^{-3}		
	6 MV	10 MV	25 MV
$N_{D,w,VSL}$ (Table 3-4)	4.2	4.2	4.2
positioning	0.5	0.5	0.5
temperature and pressure correction	0.4	0.4	0.4
combined relative standard uncertainty [$u_c(y)/y$] / 10^{-3}	4.3	4.5	4.3

Table 3-6. Standard uncertainty components for the determination of D_c/Q_{th} at 6 MV, 10 MV and 25 MV. The statistical uncertainty is based on n = 5 determinations for each radiation quality, each one the result of 10 irradiations of 60 s. The data are derived using the external transmission monitor.

Type A relative standard uncertainty component	$u_A(y)/y$ / 10^{-3}		
	6 MV	10 MV	25 MV
typical standard uncertainty of the mean ($n = 5$) including the transfer using the external transmission monitor	0.7	0.5	0.5
Type B relative standard uncertainty component	$u_B(y)/y$ / 10^{-3}		
specific heat capacity of graphite (Picard *et al* 2007)	0.9		
impurity correction	0.2		
temperature calibration	0.5		
linear model for temperature extrapolation	0.7		
axial position of calorimeter	0.5		
combined relative standard uncertainty [$u_c(y)/y$] / 10^{-3}	1.5	1.4	1.4

Table 3-7. Standard uncertainty components for the determination of Q_w/Q_c at 6 MV, 10 MV and 25 MV. The statistical uncertainty is based on n = 5 determinations for each radiation quality, each one the result of 7 irradiations of 60 s. The data are derived using the external transmission monitor and the thimble monitor.

Type A relative standard uncertainty component	$u_A(y)/y$ / 10^{-3}		
	6 MV	10 MV	25 MV
typical standard uncertainty of the mean (n = 5) including the transfer using the external transmission monitor	0.8	0.7	0.7
Type B relative standard uncertainty component	$u_B(y)/y$ / 10^{-3}		
difference in graphite jackets of core and transfer chamber		0.1	
chamber orientation for Q_c		0.1	
chamber orientation for Q_w		0.4	
volume correction k_V for the BIPM chambers		0.3	
temperature and pressure correction		0.3	
axial position of chamber		0.7	
combined relative standard uncertainty [$u_c(y)/y$] / 10^{-3}	1.2	1.2	1.2

3.3.2. Combined uncertainty

The significant uncertainties in the determination of $D_{w,VSL}/Q_{th}$ and $D_{w,BIPM}/Q_{th}$ in high-energy photon beams are listed in Table 3-1 to Table 3-7. The combined uncertainties are listed in Table 3-8. Determination of D_c, Q_w, and Q_c

3.3.3 Determination of D_c, Q_w, and Q_c

The absorbed dose to graphite D_c was obtained by taking the mean of the temperature rises detected by two thermistor bridges and applying equation (3.3) with its correction for impurities, k_{imp} = 1.0004.

The mean values of D_c, Q_c and Q_w, each normalized to the thimble monitor charge Q_{th}, are listed for each beam quality in Table 3-9 along with the statistical standard uncertainties in parentheses. For practical reasons, the BIPM method to convert to absorbed dose to water uses different transfer chambers in water and in graphite. While nominally identical, the two chambers have slightly different volumes and an appropriate correction is made to the measured charge ratio. The stated values for Q_c and Q_w in Table 3-9 are normalized to the reference air density and Q_w is corrected for the difference in volume (k_V = 0.9955).

3.3.4 Comparison results

The VSL determination of the absorbed dose to water was transferred to one transfer chamber (positioned in the VSL water calorimeter phantom) in the form of a calibration coefficient for each beam quality, determined under the reference conditions for the comparison. The use of this chamber in the BIPM water phantom under the same reference conditions resulted in the determination of $D_{w,VSL}$ used for the comparison result.

After the establishment of the Draft B comparison report, an error was discovered in the calculation of the correction for conductive heat flow, k_C. The results presented in this report have been corrected for this error. A detailed description of the error and its correction are given in section 3.7.

Table 3-11 summarizes hence the final numerical results for the BIPM and the VSL. The results and the associated standard uncertainties are shown in graphical form as a function of the measured $TPR_{20,10}$ in Figure 3-5.

Table 3-8. Standard uncertainty components in the determination of the comparison ratio $D_{w,VSL}/D_{w,BIPM}$.

relative standard uncertainty component	$u(y)/y$ / 10^{-3}		
	6 MV	10 MV	25 MV
calibration of thimble monitor in terms of $D_{w,VSL}$ (Table 3-3 to Table 3-5)	4.3	4.5	4.3
$(k_{r\,n,horizontal}/k_{r\,n,vertical})_{VSL}$ for VSL reference chamber (Table 3-2)	0.6	0.7	0.9
calibration of thimble monitor in terms of $D_{c,BIPM}$ Table 3-6	1.5	1.4	1.4
Q_w/Q_c for BIPM chambers in NPL beams Table 3–7	1.2	1.2	1.2
$C_{w,c}$ for BIPM standard in NPL beams Table 3–1	2.2	2.5	2.7
$k_{r\,n,BIPM}$ for BIPM standard in NPL beams Table 3-2	1.4	3.3	5.1
combined relative standard uncertainty $[u_c(y)/y]$ / 10^{-3}:	5.4	6.4	7.5

Table 3-9. Experimental results obtained for the BIPM calorimeter and transfer chambers, normalized to the thimble monitor charge, Q_{th}. Values in parentheses represent the standard uncertainty of the mean.

nominal accelerating voltage / MV	D_c/Q_{th} /(Gy μC^{-1})	Q_c/Q_{th}	Q_w/Q_{th}
6	17.992(13)	4.4388(30)	4.3108(23)
10	20.193(10)	5.0084(28)	4.8475(21)
25	23.124(11)	5.9056(5)	5.7561(43)

Table 3-10. Absorbed dose to water determined by the BIPM, $D_{w,BIPM}$. The dose values are given relative to the charge, Q_{th}, measured by the thimble monitor using the external transmission monitor. Also given are the determined values for D_c/Q_c, Q_w/Q_{th} and $k_{rn,BIPM}$ as well as the total BIPM Monte Carlo conversion factors $C_{w,c}$.

nominal accelerating voltage / MV	D_c/Q_c /(Gy μC^{-1})	Q_w/Q_{th}	$k_{rn,BIPM}$	$C_{w,c}$	$D_{w,BIPM}/Q_{th}$ /Gy μC^{-1})
6	4.0533	4.3108	1.0019	1.1218	19.638
10	4.0319	4.8475	0.9918	1.1301	21.906
25	3.9156	5.7561	0.9915	1.1428	25.538

Table 3-11. Absorbed dose to water determined by the VSL, $D_{w,VSL}$ and the BIPM, $D_{w,BIPM}$, and the quotient $D_{w,VSL}/D_{w,BIPM}$. The dose values are given relative to the charge, Q_{th}, measured by the thimble monitor using the external transmission monitor. The comparison result R and associated uncertainty is also listed for each radiation quality.

nominal accelerating voltage /MV	measured TPR$_{20,10}$	$D_{w,VSL}/Q_{th}$ /(Gy μC^{-1})	$D_{w,BIPM}/Q_{th}$ /(Gy μC^{-1})	$D_{w,VSL}/D_{w,BIPM} = R$	$u_c(R)/R$
6	0.682	19.559	19.638	0.9959	0.0054
10	0.733	21.815	21.906	0.9958	0.0064
25	0.800	25.516	25.538	0.9991	0.0075
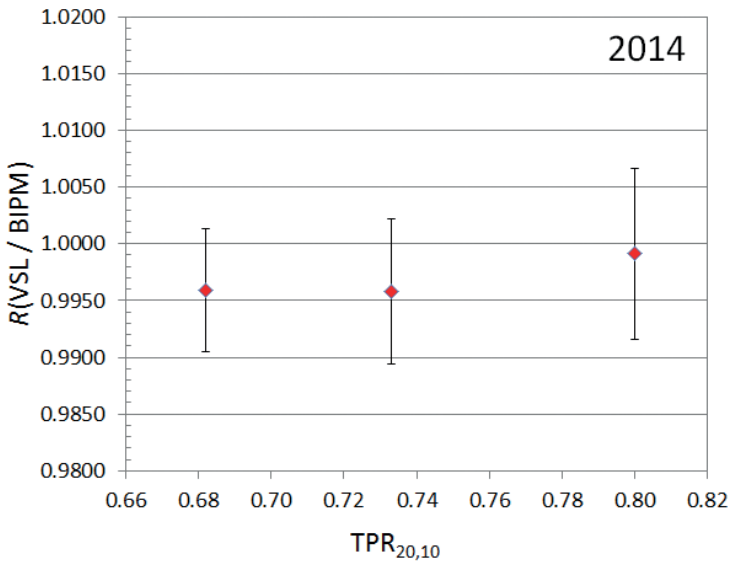
Figure 3-5. Results of the 2014 comparison at high energies of the calorimetric absorbed dose to water standards of the VSL and the BIPM, shown as a function of the measured TPR$_{20,10}$. The uncertainty bars represent the combined standard uncertainty of each comparison result.
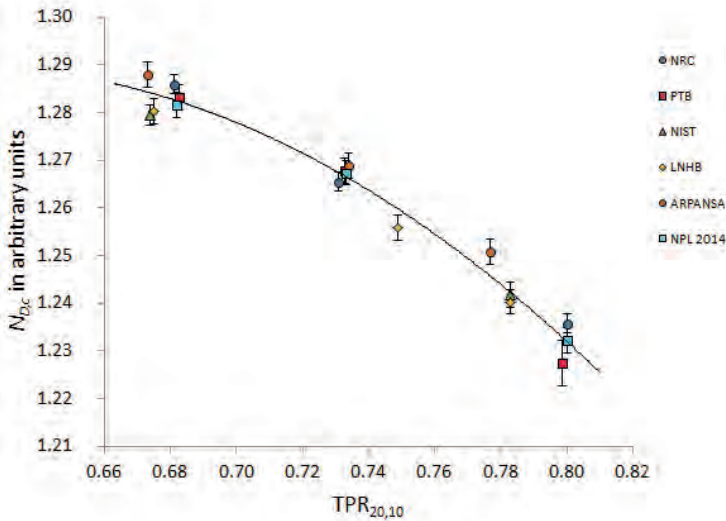
Figure 3-6. The measured calibration coefficient $N_{D,c} = D_c/Q_c$, corrected for recombination, for the accelerators of the NRC, PTB, NIST, LNE-LNHB, ARPANSA and the NPL as a function of measured TPR$_{20,10}$.

3.4. Discussion

The present comparison presented no major technical problems. A failure of one of the BIPM components (calo-6) was discovered in the beginning of the comparison and was easily overcome as a result of the recent implementation of a back-up system for key BIPM devices.

All measurements were carried out under the reference conditions normally used by the VSL.

Following receipt of the Draft A, the VSL made an update of the correction factors for heat transfer and for perturbations linked to the VSL glass vessel used in the measurements at the NPL. After the establishment of the Draft B comparison report, a numerical error was discovered in the calculation of the correction for conductive heat flow, k_C. The results presented in this report have been corrected for these errors. A detailed description of the modifications involved is given in section 3.7.

The Draft B report stated the following comparison results: 0.9980(54) at 6 MV, 0.9977(64) at 10 MV and 1.0010(75) at 25 MV. The final results are: 0.9959(54) at 6 MV, 0.9958(64) at 10 MV and 0.9991(75) at 25 MV. The final results are hence all smaller by 0.2 % compared to the initial results. The final result at 25 MV is close to unity. This is despite the fact that the calculated horizontal and vertical values for the non-uniformity correction at 25 MV differ by 0.8 %, a difference taken into account in the estimated uncertainty of k_{rn} at 25 MV. Given the limited data available to characterize beam uniformity in two dimensions and its potential variation over the duration of the comparison, the stated uncertainties for k_{rn} might be under estimated.

The correction for recombination losses in pulsed beams was determined for the BIPM transfer chambers in a separate series of measurements (Picard *et al* 2011a). While this effect will cancel for the measured ratio Q_c/Q_w, the correction of Q_c for recombination allows the calibration coefficient $N_{D,c}$ measured at different NMIs using the same chamber (calo-3) to be directly compared. These results, shown in Figure 3-5, serve as an additional check on the BIPM measurements during a comparison and include the National Research Council (NRC) Canada, Physikalisch-Technische Bundesanstalt (PTB) Germany, the National Institute of Standards and Technology (NIST), the Laboratoire National de Métrologie et d'Essais – Laboratoire National Henri Becquerel (LNE-LNHB), the Australian Radiation Protection and Nuclear Safety Agency, and the present work (Picard *et al* 2010b, 2011b, 2013b, 2013c, 2014), all determined at a reference depth of 10 g cm^{-2}.

3

Monte Carlo calculations of the conversion factor $C_{w,c}$ for different beam qualities have now been made using phase-space files generated by the NRC, PTB, NIST, LNHB, ARPANSA and the NPL, all determined at 10 g cm^{-2}. The results are shown in Figure 3-7 along with a weighted quadratic fit to the data. The deviations about this line are consistent with the typical statistical standard uncertainty of 5 parts in 10^4. Note that, for consistency, the results for the NPL are those calculated for calo-6 and its waterproof sleeve, as used for all previous comparisons. The actual values for $C_{w,c}$ used for the present comparison (using calo-5) are those given in Table 3-1 and are slightly lower, as noted in the footnote to the table. Assuming that the relative response of calo-5 and calo-6 follow this predicted change, there should be no effect on the BIPM D_w determination.

Three nominal ranges of radiation qualities are defined for the BIPM.RI(I)-K6 key comparison (ADWG(I) 2017). The comparison results obtained to date in these three ranges are shown in Figure 3-8. The uncertainty bars represent the standard uncertainty of each comparison and are therefore correlated through the common use of the BIPM standard (as well as any correlation that might exist between any of the NMI standards).

It may be noted that the results of the NPL at 10 g cm^{-2} and the results of the VSL presented here refer to the same BIPM measurement and are hence more strongly correlated than the other NMI measurements. However, the NPL results at 10 g cm^{-2} are not included in the list of Degrees of Equivalences (conform section 3.5), as such depth is not yet defined by the UK dosimetry protocol (Lillicrap *et al* 1990).

3.5. Degrees of Equivalence

Following a decision of the CCRI, the BIPM calorimetric determination of absorbed dose to water as determined by the BIPM on the NMI site is taken as the key comparison reference value (CCRI 2013, Picard *et al* 2013a). It follows that for each NMI$_i$ having a BIPM comparison result R_i, with a combined standard uncertainty u_i, the degree of equivalence with respect to the KCRV is given by a pair of terms D_i and U_i:

$$D_i = R_i - 1 \qquad\qquad (3.6)$$

$$U_i = 2\,u_i. \qquad\qquad (3.7)$$

These terms represent the relative difference and the expanded uncertainty ($k = 2$) of this difference.
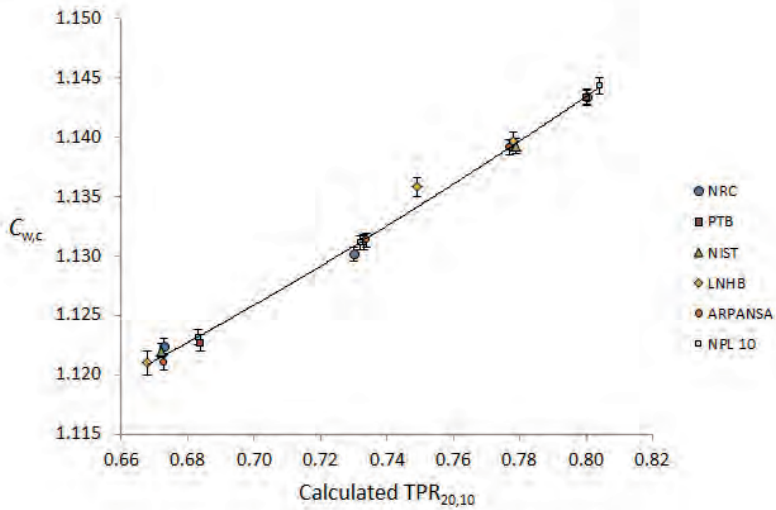
Figure 3-7. The measured calibration coefficient $N_{D,c} = D_c/Q_c$, corrected for recombination, for the accelerators of the NRC, PTB, NIST, LNE-LNHB, ARPANSA and the NPL as a function of measured $TPR_{20,10}$.
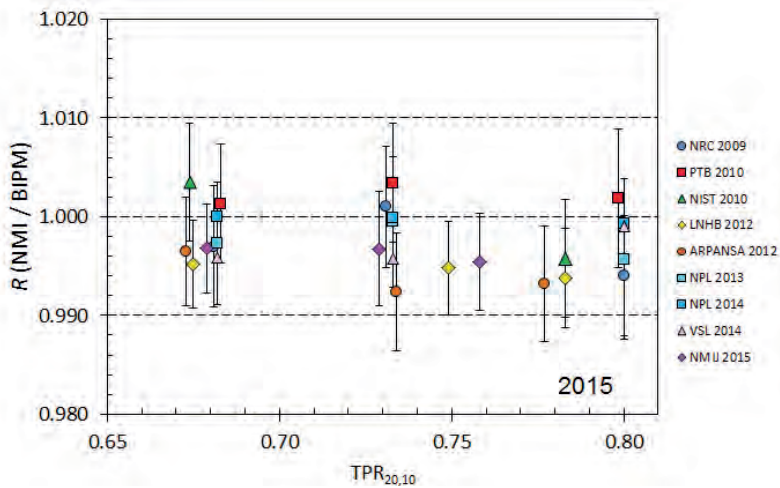
Figure 3-8. Results of the comparisons of accelerator dosimetry to date, reported as a ratio of the NMI and the BIPM evaluations of absorbed dose to water for the NRC, PTB, NIST, LNE-LNHB, ARPANSA, NPL (at 5 g cm^{-2} and 7 g cm^{-2}, and at 10 g cm^{-2}, respectively), NMIJ and the VSL (this work), as a function of the measured $TPR_{20,10}$. The uncertainty bars represent the standard uncertainty of each comparison result. Abreviations: National Research Council (NRC) Canada, Physikalisch-Technische Bundesanstalt (PTB) Germany, the National Institute of Standards and Technology (NIST), the Laboratoire National de Métrologie et d'Essais – Laboratoire National Henri Becquerel (LNE-LNHB), the Australian Radiation Protection and Nuclear Safety Agency, National Physics Laboratory (NPL) United Kingdom, VSL (VSL) Netherlands and National Metrology Institute of Metrology (NMIJ) (Picard *et al* 2010b, 2011b, 2013b, 2013c, 2014, 2015a).

The degrees of equivalence, D_i and U_i, for each of the NMIs having participated until December 2015 are listed and represented graphically in section 3.8, as they will appear in the KCDB.

3.6. Conclusion

This result is the ninth in the on-going BIPM key comparison BIPM.RI(I)-K6. The results, reported as ratios of the VSL and the BIPM evaluations (and with the combined standard uncertainties given in parentheses), are 0.9980(54) at 6 MV, 0.9977(64) at 10 MV and 1.0010(75) at 25 MV. The results for BIPM.RI(I)-K6 are available in the BIPM key comparison database (BIPM 2019).

3.7. Appendix 1

After the comparison measurements, i.e. between establishment of the Draft A and the final comparison report, VSL updated the water calorimeter correction factors for the perturbation due to the presence of non-water materials (mostly glass) k_P, and for conductive heat flow, k_C. The reasons and consequences of these changes are described in this appendix.

3.7.1. Changes in perturbation correction

The Draft A values reported for k_P were based on measurements made in a ^{60}Co beam for the high-purity cell (HPC02) that was used for the comparison, scaled to higher energies, i.e. 6 MV, 10 MV and 25 MV. This scaling is based on measured values of k_P of the previous cell (HPC01). The Draft B values reported for k_P (HPC02) were obtained by measurement in 6 MV and 10 MV beams at the Netherlands Cancer Institute (Amsterdam). However, the 25 MV value for k_P was obtained from extrapolation of the values at 6 MV and 10 MV based on the beam quality specifier $\text{TPR}_{20,10}$. Changes in the perturbation correction are reported in Table 3-13.

3.7.2. Changes in excess-heat correction

Shortly after the comparison measurements, the VSL re-assessed the magnitude of the perturbation correction factors of the water cell. As a result of an improved heat transport model, the correction for conductive heat flow, k_C, in the VSL water calorimeter needed to be updated. The original values were based on a 2D cylindrical symmetric model for conductive effects with simplified geometries for glass cell and probe without consideration of lateral and depth dose profiles. The cylindrical glass cell was modelled with a diameter of 73 mm and a wall thickness of 0.7 mm at the centre, increased to 1 mm after 30 mm from the centre. The probe was modelled as pure glass

with a diameter of 0.6 mm over its complete length. The updated model consisted of a quarter 3D geometry of the calorimeter phantom with realistic geometries of glass cell, probes (with thermistor bead) and calorimeter wall, including full lateral and depth dose profiles. The cylindrical glass cell was modelled with a diameter of 72 mm and a wall thickness between 0.9 mm in the centre, gradually increasing to 1.4 mm at the sides. The probe was modelled as glass with a diameter of 0.6 mm, including a 0.3 mm diameter spherical thermistor bead in the tip. The probe diameter was extended to 6 mm towards the base of the probe, near the connection to the cell. Hence, after establishing the Draft A, corrected values were reported which were incorporated in the Draft B report.

However, during the review process of the submitted Draft B report, an error was discovered in the updated model: wrong values for the specific heat capacity and density of glass and thermistor material were used. The values for specific heat capacity and material density were reversed, for both glass and the thermistor material, due to a numeric error in the table of an internal VSL report. This led to erroneous volumetric heat sources in the respective bodies of the HPC and the thermistor probes. The results presented in this report are corrected for this error. The erroneous and correct values for heat capacity and density are listed in Table 3-12.

To ensure that the new model is based on a proper understanding of the physical behaviour, a considerable refinement was made by separating the relative excess temperature for the lateral and depth dose profile in a 3D model and for the cell and probes (including thermistor bead, Pt-alloy wire and glue) in a 2D model, in detail described by de Prez et al (2016). As a supplementary benefit, the VSL was able to model the probes with greater detail with sufficient accuracy and calculation time. Changes in the excess-heat correction are reported in Table 3-13.

3.7.3. Results

The Draft A and former Draft B values for k_p and k_C are given in Table 3-13 as well as the values currently reported. The change in reported values for k_p since Draft A is between 0.01 % at 6 MV and 0.03 % at 25 MV. The relative standard uncertainty for k_p remains the same and is 0.07 % ($k = 1$). The change in reported values for k_C since Draft A is between 0.20 % at 6 MV and 0.26 % at 25 MV. The reported relative standard uncertainty for k_C remains the same and is 0.18 % ($k = 1$).

An error linked to the application of the correction for the radial non-uniformity of the beam was also discovered and corrected for, between the Draft A and Draft B. Finally, small errors in the calculated thermistor self-heating, ion recombination and polarity effects

in the VSL system were also rectified. These corrections are summarized in Table 3-14.

The numerical values of the comparison results following from the changes in the VSL correction factors, and the appropriate application of the correction for non-radial uniformity of the beam between draft A and B and between draft B and the present report are summarized in Table 3-15.

Table 3-12. Values for specific heat capacity and density of glass and thermistor material in the erroneous and correct heat transfer simulations.

| | erroneous values | | correct values | |
| | c_p | ρ | c_p | ρ |
material	/(J kg^{-1} K^{-1})	/(kg m^{-3})	/(J kg^{-1} K^{-1})	/(kg m^{-3})
glass	2400	836	836	2400
thermistor	5130	836	836	5130

Table 3-13. VSL changes in correction factors for perturbation and excess-heat, k_P and k_C since the Draft A comparison report.

| nominal accelerating voltage /MV | k_P | | | k_C | | |
	Draft A	Draft B	this report	Draft A	Draft B	this report
6	1.0012	1.0013	1.0013	0.9955	0.9995	0.9974
10	1.0008	1.0011	1.0011	0.9955	0.9998	0.9979
25	1.0004	1.0007	1.0007[9]	0.9955	0.9997	0.9978

Table 3-14. Corrections for influencing factors since the Draft A comparison report.

| nominal accelerating voltage /MV | k_{rn} (VSL) | | | $k_{sh} \cdot k_s \cdot k_{pol}$ (VSL) | | |
	Draft A	Draft B	this report	Draft A	Draft B	this report
6	1.0000	1.0003	1.0003	1.0030	1.0040	1.0040
10	1.0000	0.9963	0.9963	1.0041	1.0043	1.0043
25	1.0000	0.9988	0.9988	1.0041	1.0043	1.0043

Table 3-15. Numerical values of the comparison results following corrections made between draft A and B and between draft B and the present report.

| nominal accelerating voltage /MV | Comparison result | | |
	Draft A	Draft B	this report
6	0.9926(54)	0.9980(54)	0.9959(54)
10	0.9968(64)	0.9977(64)	0.9958(64)
25	0.9975(75)	1.0010(75)	0.9991(75)

---

9   This value is based on scaling of the perturbation correction with the old high purity cell HPC01.

3.8. Appendix 2

Key comparison BIPM.RI(I)-K6

MEASURAND : Absorbed dose to water

The key comparison reference value is the BIPM determination of absorbed dose to water in an accelerator beam

The degree of equivalence of each laboratory i with respect to the key comparison reference value is given by a pair of terms: the relative difference D_i and $U_i = 2u_i$, its expanded uncertainty (k = 2), both expressed in mGy/Gy.

When required, the degree of equivalence between two laboratories i and j can be evaluated by a pair of terms:

$D_{ij} = D_i - D_j$ and $U_{ij} = 2u_{ij}$, its expanded uncertainty (k = 2), both expressed in mGy/Gy.

In evaluating u_{ij}, account should be taken of correlation between u_i and u_j.
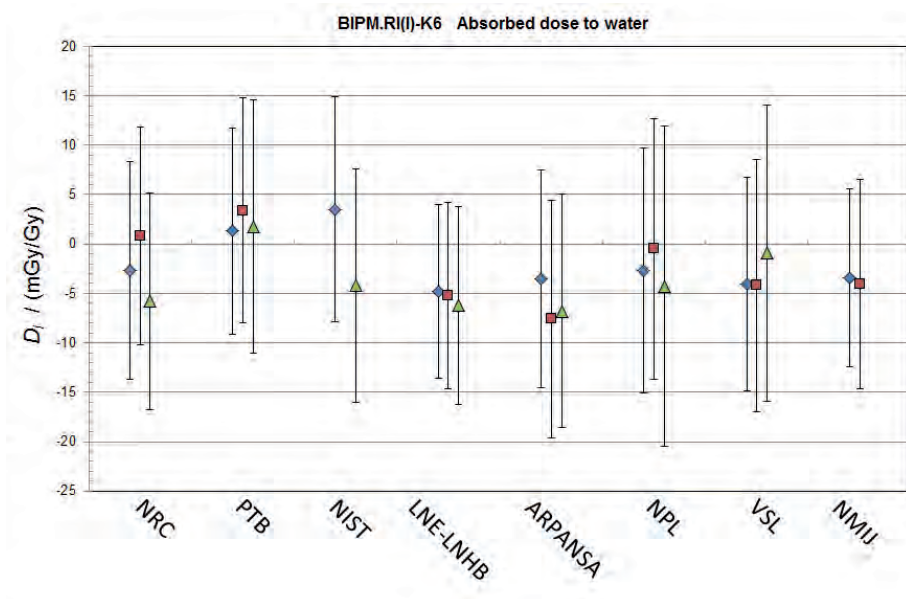
Figure 3 9. Abreviations: National Research Council (NRC) Canada, Physikalisch-Technische Bundesanstalt (PTB) Germany, the National Institute of Standards and Technology (NIST), the Laboratoire National de Métrologie et d'Essais – Laboratoire National Henri Becquerel (LNE-LNHB), the Australian Radiation Protection and Nuclear Safety Agency, National Physics Laboratory (NPL) United Kingdom, VSL (VSL) Netherlands and National Metrology Institute of Metrology (NMIJ) (Picard et al 2010b, 2011b, 2013b, 2013c, 2014, 2015a).

Graph of degrees of equivalence D_i with the KCRV for each of the NMIs having participated until end of 2014.

4

Comparison of k_Q factors measured with a water calorimeter in flattening filter free (FFF) and conventional flattening filter (cFF) photon beams

Abstract

Recently flattening filter free (FFF) beams became available for application in modern radiotherapy. There are several advantages of FFF beams over conventional flattening filtered (cFF) beams, however differences in beam spectra at the point of interest in a phantom potentially affect the ion chamber response. Beams are also non-uniform over the length of a typical reference ion chamber and recombination is usually larger. Despite several studies describing FFF beam characteristics, only a limited number of studies investigated their effect on k_Q factors. Some of those studies predicted significant discrepancies in k_Q factors (0.4 % up to 1.0 %) if $TPR_{20,10}$ based codes of practice (CoPs) would be used. This study addresses the question to which extent k_Q factors, based on a $TPR_{20,10}$ CoP, can be applied in clinical reference dosimetry. It is the first study that compares k_Q factors measured directly with an absorbed dose to water primary standard in FFF-cFF pairs of clinical photon beams. This was done with the transportable water calorimeter described in Chapter 2 (de Prez *et al* 2016a). The measurements corrected for recombination and beam radial non-uniformity were performed in FFF-cFF beam pairs at 6 MV and 10 MV of an Elekta Versa HD for a selection of three different Farmer-type ion chambers (8 serial numbers). The ratio of measured k_Q factors of the FFF-cFF beam pairs were compared with the $TPR_{20,10}$ CoPs of the NCS and IAEA and the $\%dd(10)_x$ CoP of the AAPM. For the $TPR_{20,10}$ based CoPs differences less than 0.19 % were found in k_Q factors between the corresponding FFF-cFF beams with standard uncertainties smaller than 0.35 %, while for the $\%dd(10)_x$ these differences were smaller than 0.42 % and within the expanded uncertainty of the measurements. Based on the measurements made with the equipment described in this study the authors conclude that the k_Q factors provided by the NCS-18 and IAEA TRS-398 codes of practice can be applied for flattening filter free beams without additional correction. However, existing codes of practice cannot be applied ignoring the significant volume averaging effect of the FFF beams over the ion chamber cavity. For this a corresponding volume averaging correction must be applied.

4.1. Introduction

High-energy photon beams from clinical linear accelerators operating in flattening filter free (FFF) mode have been available since the early 1980's (Brahme *et al* 1980). They have been applied and characterized for application in radiosurgery (O'Brien *et al* 1991). Recently FFF beams became available for application in other radiotherapy techniques such as intensity-modulated radiotherapy (IMRT) and volumetric-modulated arc therapy (VMAT) (Georg *et al* 2011, Paynter *et al* 2014). The main advantages of FFF compared to conventional flattening filtered (cFF) beams are the increased dose rate, resulting in reduced treatment time, reduced lateral beam quality variation and a reduced out of field dose to the patient (Robar *et al* 2002, Titt *et al* 2006, Vassiliev *et al* 2006).

Differences between cFF and FFF beams, their consequences and relevant literature have been described by working groups of the American Association of Physicists in Medicine (Xiao *et al* 2015) and the Institute of Physics and Engineering in Medicine (Budgell *et al* 2016). The modifications of FFF beams compared to cFF beams result in a greater low-energy spectral component, which is partly reduced by the backscatter plate and, in some cases, an added thin filter. FFF beams are also non-uniform over the length of a typical ion chamber used in reference dosimetry, and can have a significantly higher dose rate in the chamber volume (Lye *et al* 2016). Despite a number of studies describing differences in beam characteristics between FFF and cFF beams only a limited number of studies investigated the effect of FFF beams on k_Q factors in reference dosimetry. These were based on Monte Carlo simulations, and none of them performed direct k_Q measurements with a primary standard in a clinical linear accelerator[10]. One of these studies is a Monte Carlo study by Xiong and Rogers (2008), who calculated restricted stopping power ratios where flattening filters of conventional linac beams were removed. Other corrections were not taken into account. This study concluded that differences between k_Q factors determined for FFF and cFF beams could lead up to 0.4 % errors when applying $\%dd(10)_x$, 0.2 % with a new $\%dd(10)_x$ fit, or 1 % when applying $TPR_{20,10}$ for photon energies up to 25 MV. The AAPM TG-51 addendum (McEwen *et al* 2014) implemented the new $\%dd(10)_x$ fit proposed by Xiong and Rogers (2008). A similar Monte Carlo study reported by Dalaryd *et al* (2014) was based on more realistic clinical FFF beams. Their study showed smaller differences for $TPR_{20,10}$ than predicted by Xiong and Rogers. Lye *et al* (2016) found differences smaller than 0.2 % comparing absorbed dose measurements based on the $TPR_{20,10}$ based code of practice IAEA TRS-398, or the $\%dd(10)_x$ based code of practice, AAPM TG-51 for FFF-cFF beam pairs of 6 MV and 10 MV in different accelerator beams.

---

10   Budgell *et al* (2016) reported directly measured k_Q factors with the National Physical Laboratory (NPL, Teddington, UK) primary standard in lightly filtered non-clinical research linac formerly used at NPL.

Despite the relevance of these studies, Monte Carlo studies are limited by the use of models for both ion chambers and accelerator beams. Direct measurement of k_Q factors with primary standards are essential to understand the individual behaviour of physical chambers in real clinical accelerators. This study aims to answer the question to which extent k_Q factors based on a $TPR_{20,10}$ and $\%dd(10)_x$ protocol for cFF beams can be applied in clinical reference dosimetry for FFF beams. In contrast to previous studies, this is done by direct comparison of k_Q factors measured with a primary standard in clinical FFF and cFF beams of 6 MV and 10 MV for a single accelerator for a selection of eight ion chambers of three types.

4.2. Materials and methods

4.2.1. Measurement of k_Q

The most direct way to determine absorbed dose to water, D_w, and k_Q in various photon beams is a carefully conducted measurement (Andreo *et al* 2000, Seuntjens and Duane 2009). This is done by calibrating the ion chamber in beam quality Q, resulting in a calibration coefficient $N_{D,w,Q}$, and in the reference beam quality Q_0, N_{D,w,Q_0}. It involves two absorbed dose to water measurements with a primary standard, and two ion chamber measurements, M, under the same reference conditions in beam quality Q and Q_0 (Hohlfeld 1988, Andreo 1992, Rogers 1992):

$$k_Q = \frac{N_{D,w,Q}}{N_{D,w,Q_0}} = \frac{(D_w/M)_Q}{(D_w/M)_{Q_0}}. \tag{4.1}$$

Generally, k_Q is expressed as a function of a beam quality specifier, $\%dd(10)_x$ or $TPR_{20,10}$, respectively applied in the AAPM TG-51 code of practice and its addendum (Almond *et al* 1999 and McEwen *et al* 2014) and the codes of practice of the International Atomic Energy Agency (IAEA) TRS-398 (Andreo *et al* 2000), IPEM (Lillicrap *et al* 1990), Deutsche Industrie Norm 6800-2 (DIN 2008) and Nederlandse Commissie voor Stralingsdosimetrie (NCS) report 18 (Aalbers *et al* 2008). The results of this study will be compared with the codes of practice of the NCS, IAEA and AAPM, further referred to as NCS-18, TRS-398 and TG-51, respectively.

4.2.2. Measurement of k_Q for FFF-cFF beam pairs

The comparison of k_Q factors in FFF and cFF beam pairs of 6 MV and 10 MV is done in a similar fashion as expressed by equation (4.1), where the beam quality specifiers of both FFF and cFF beams have the same value Q, and cFF is considered the reference beam. This can be expressed as a ratio:

$$\frac{k_Q^{\text{FFF}}}{k_Q^{\text{cFF}}} = \frac{N_{D,\text{w},Q}^{\text{FFF}}}{N_{D,\text{w},Q}^{\text{cFF}}} \cdot \tag{4.2}$$

Note that the value of Q depends on the selected beam quality specifier (i.e. $\text{TPR}_{20,10}$ or $\%dd(10)_x$). However, unless the FFF and cFF beams are matched with respect to the selected beam quality specifier, such that the values of Q for both beams are the same, the measured k_Q of the cFF beam quality, here Q', needs to be normalized to its value at beam quality of the FFF beam, Q. Hence, the ratio, R, of calibration coefficients for FFF and cFF beams, normalized to the beam quality value of the FFF beam becomes:

$$R = \frac{N_{D,\text{w},Q}^{\text{FFF}}}{N_{D,\text{w},Q'}^{\text{cFF}}} \cdot k_{Q',Q}^{\text{cFF}} \cdot \tag{4.3}$$

The first term on the right-hand side is the measured ratio of k_Q factors in the FFF and cFF beams with beam qualities Q and Q', respectively. The second term on the right-hand side is the normalization of the cFF $k_{Q'}$ with beam quality Q' to the beam with the beam quality, Q, of the FFF beam. This normalization depends on the choice of chamber type with code of practice, CoP (i.e. k_Q dataset and beam quality specifier). It is determined by applying the values of Q' and Q with respect to the chamber type according to the respective CoP:

$$k_{Q',Q}^{\text{cFF}} = \left\{ \frac{k_{Q'}}{k_Q} \right\}_{\text{CoP}}^{\text{chambertype}} \tag{4.4}$$

The difference between k_Q of an FFF beam compared to a cFF beam can then be expressed as:

$$\Delta k_{\text{FFF,cFF}} = R - 1. \tag{4.5}$$

In this study, uncertainties are expressed as relative standard uncertainties ($k = 1$), in some cases represented between brackets as the least significant digits of the reported value.

4.2.3. Choice of ion chambers and beam qualities

Eight ion chambers of three types (2 × PTW 30013; 3 × PTW 30012 and 3 × NE2571, from PTW Freiburg GmbH Freiburg, Germany and Phoenix Dosimetry Ltd Sandhurst, UK, respectively) were calibrated in two FFF-cFF beam pairs. The choice of chambers was based on their availability at the time of the measurements and the availability

of k_Q datasets in the applied CoPs. At least one of the chamber types needed to be waterproof to be measured directly inside the calorimeter phantom. NCS-18, based on $TPR_{20,10}$, provides measured k_Q data for two of the chamber types used in this study, the PTW 30012 and the NE2571 among other chambers, but not for the waterproof PTW 30013 chamber. For all chambers used in this study, k_Q data is available in TRS-398 using $TPR_{20,10}$ and in TG-51 using $\%dd(10)_x$.

All measurements were performed in four beams of an Elekta Versa HD (Elekta AB, Stockholm, Sweden) at the Netherlands Cancer Institute. In FFF mode the beams include a 2 mm steel thin filter in the same position where the flattening filter is in cFF mode. The Elekta FFF beams are *energy-matched*; i.e., accelerator parameters have been adjusted such that the percentage depth dose at 10 cm depth, PDD(10), of the FFF beams match those of the cFF beams for a 10 cm × 10 cm field (Paynter *et al* 2014, Xiao *et al* 2015). $TPR_{20,10}$ is measured according to the method described in TRS-398 while $\%dd(10)_x$ is taken to be equal to PDD(10), measured at an SSD of 100 cm and a field size of 10 × 10 cm², and were shown to be adequate for both FFF and cFF beams according to Lye *et al* (2016) without additional correction for recombination and volume averaging due to beam radial non-uniformity. For determination of the beam quality no additional correction was applied for the 'reduced equivalent square field size' of the FFF beams compared to the cFF beams (Palmans *et al* 2017).

Table 4-1 shows the beam qualities used in this study and $k_{Q',Q}{}^{cFF}$ from equation (4.3) and (4.4) with respect to NCS-18 and TRS-398. Note that $k_{Q',Q}{}^{cFF}$ for application of $\%dd(10)_x$ is unity because the beams are energy matched with respect to PDD(10), resulting in equal values for $\%dd(10)_x$.

Table 4-1: Beam qualities applied in this study and the $k_{Q',Q}{}^{cFF}$ with respect to the NCS-18 and TRS-398 CoP and chamber types. Note that $k_{Q',Q}{}^{cFF}$ for $\%dd(10)_x$ based TG-51 is unity and therefore not reported.

beams	$\%dd(10)_x$	$TPR_{20,10}$	chamber type	$k_{Q',Q}{}^{cFF}$	
				NCS-18[a]	TRS-398
6 MV cFF	67.5 %	0.680	PTW 30013	–	0.9994
6 MV FFF		0.675	PTW 30012	0.9994	0.9997
			NE2571		0.9997
10 MV cFF	73.0 %	0.735	PTW 30013	–	0.9969
10 MV FFF		0.720	PTW 30012	0.9968	0.9977
			NE2571		0.9977

[a]NCS-18 makes no distinction between reported 0.6 cm³ Farmer-type chambers
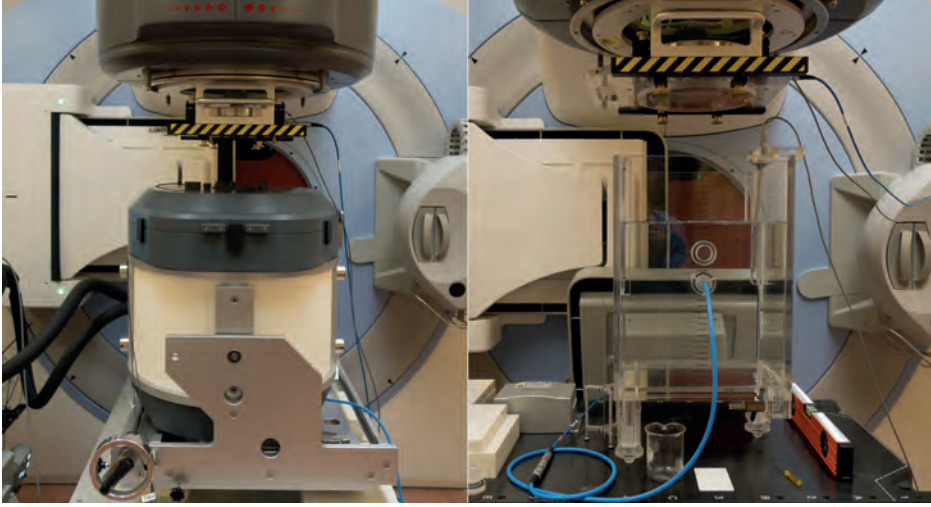
Figure 4-1. The VSL calorimeter (left) and the calibration phantom (right) in the facility of an Elekta Versa HD clinical accelerator at the Netherlands Cancer Institute.

4.2.4. Water calorimetric determination of absorbed dose

The water calorimetric determination of absorbed-dose, D_w, requires a measurement of radiation-induced temperature rise in water, ΔT_w, multiplied by the specific heat capacity of water, c_p, and is given by the expression:

$$D_w = \Delta T_w \cdot c_p \cdot (1 - h)^{-1} \cdot k_C \cdot k_{HPC} \cdot k_{nu}.$$

$$(4.6)$$

The chemical heat-defect, h, is caused by radiation-induced exo- or endothermic chemical reactions. For photon beams this effect is described by various authors, e.g. Domen (1982), Klassen and Ross (1997), Seuntjens and Palmans (1999) and Krauss and Kramer (2003). The k-factors in equation (4.6) correct for: the conductive heat flow, k_C, caused by relative excess temperature rise, R_{XS}, due to non-water materials and the non-uniform 3D-dose distributions (Krauss 2006b); the perturbation due to the presence of non-water materials (mostly glass), k_{HPC}; and the deviation of the measurement conditions from the reference conditions, radial non-uniformity, k_{nu}. Because the water calorimeter is operated at 4 °C, the temperature at which the density of water is maximal, it is assumed that no convection takes place (Domen 1988). The energy dependence of k_C due to stopping power ratios material-water, between ^{60}Co and 30 MV is less than 0.1 % as shown, for instance, by Seuntjens *et al* (2000). Radiative heat transfer is insignificant for the small temperature differences generated in a water calorimeter (Seuntjens and Duane 2009).

The VSL calorimeter, described in detail by de Prez *et al* (2016) and shown in Figure 4-1, consists of a cylindrical water phantom made of aluminium and surrounded by a temperature-controlled thermostat. The beam enters the calorimeter at the centre of a removable lid through a square radiation window and passes through several thin layers of material. A PMMA radiation entrance window is in contact with the water surface. A cylindrical high-purity water cell (HPC) made of glass with a thin wall contains two negative temperature coefficient (NTC) thermistors embedded in miniature glass pipettes. These are used to measure the radiation induced temperature change in water, ΔT_w in equation (4.6). The thermistor probes are mounted 10 mm apart inside the HPC filled with argon saturated ultra-pure water.

With respect to FFF and cFF beams, special attention was paid to the modelled heat conduction correction, k_C, the radial non-uniformity of the field at the position of the thermistors, k_{nu}, and the measured correction due to perturbation and scatter of the glass cell, k_{HPC}. The perturbation and scatter effect due to the presence of the thermistor probes was measured previously in ^{60}Co and showed to be negligible within the uncertainty of 0.05 %. k_C was determined with finite element simulation according to the heat transfer models described by de Prez *et al* (2016). This correction depends on lateral and depth dose profiles and the radiation induced temperature increase of materials, which in turn depend on material specific heat capacity and electron stopping power ratios of those materials to water. The calorimeter correction for beam radial non-uniformity, k_{nu}, at the position of the probe tips, 5 mm off-axis, was based on the in-line measured lateral dose profile and determined by the measured ratio at beam centre and 5 mm off-axis. The influence of the presence of the calorimeter thermostat (i.e. calorimeter phantom and lid) was measured to quantify potential changes in beam qualities. It was measured with the waterproof chambers inside the calorimeter thermostat (directly in water) and inside a 1 mm PMMA sleeve in the calibration water phantom ($30 \times 30 \times 30$ cm^3).

4.2.5. Ion chamber calibration
Two waterproof PTW 30013 ion chambers were calibrated directly inside the calorimeter thermostat without waterproofing sleeve. Subsequently, the other six non-waterproof chambers were cross-calibrated against the two waterproof chambers inside the PMMA sleeve in the calibration phantom placed on the treatment couch as shown in Figure 4-1. The chambers were positioned in-line with the accelerator in both measurement setups. The measurements were done according to NCS-18 at a nominal source surface distance (SSD) of 90 cm and depth of 10 g cm^{-2}. Water depth was corrected for water density due to the different temperatures applied during calorimetry at 4 °C and ion chamber measurements at room temperature. The field size at the isocentre was 10×10 cm^2. The

chambers were calibrated with a bias voltage supplied by the electrometer (Keithley 6517B, Tektronix Ltd. Bracknell, UK) with the thimble connected to ground. Bias and polarity were either -300 V, collecting positive charge (CEN) or +350 V collecting negative charge (CEP), depending on the bias convention used by the chamber owner (VSL or the Netherlands Cancer Institute). The leakage corrected raw ion chamber measurements, M_{raw}, were corrected for electrometer calibration, k_{elec}, air density inside the cavity as a result of actual temperature and pressure, $k_{p,T}$, polarity, k_{pol} and saturation, k_s in agreement with NCS-18 and TRS-398. For these corrections, difference in reference conditions and methods described by TG-51 are not expected to affect the k_Q values.

Additionally, a correction was applied for beam radial non-uniformity due to the volume averaging effects of the dose over the ion chamber, k_v. This was determined using a simple 1D integration of the beams lateral dose profiles along the thimble chamber dimension positioned in-line with the accelerator similar to the method described by Lye *et al* (2016) and Palmans *et al* (2017). The diameter (6 mm) of the thimble is considerably smaller than the length (23 mm) therefore, despite the relative large lateral dose gradient in FFF beams, the non-uniformity along the direction of the radius (i.e. in cross-line direction) was found to be smaller than 0.01 % in all cases and therefore neglected.

No correction was applied for humidity of the air inside the chamber cavity since all measurements were performed at a humidity close to 50 % ($\pm$ 10 %). The applied formalism for the ion chamber measurements was (Andreo *et al* 2000, Almond *et al* 1999):

$$M = M_{raw} \cdot k_{elec} \cdot k_{p,T} \cdot k_{pol} \cdot k_s \cdot k_v. \tag{4.7}$$

Just as with the calorimeter measurements, no correction was applied for the presence of the calorimeter thermostat, $k_{phantom}$, and the presence of the calorimeter entrance window was not expected to influence the beam quality significantly for any of the measured photon beams.

It must be noted that the calibration coefficients of the non-waterproof chambers in beam quality Q were determined without the effect of the waterproof sleeve, generally considered to be small (Ross and Shortt 1992). After all, during the cross-calibration both waterproof and non-waterproof chambers were placed inside the sleeve and the effect cancels. This has no effect on the results of this study, however, it must be considered when comparing k_Q between studies.

The calorimeter measurements took place over several days prior to the measurements

of the waterproof ion chamber inside the calorimeter phantom. This was followed by the cross calibration of the non-waterproof chambers in the standard calibration phantom using an *intermediate working standard ionization chamber* as described by (McEwen 2010). The calibration coefficient of the *intermediate working standard ionization chamber* is determined according to:

$$N_{D,w} = \frac{(D_w/\text{MU})}{(M/\text{MU})}.$$ (4.8)

Here D_w is the absorbed dose to water, measured inside the water calorimeter thermostat and M the corrected ion chamber reading. Both D_w and M are normalized to an independent transmission monitor ion chamber (PTW 34014) with signal MU, mounted on the accelerator tray.

The ratio of calibration coefficients of FFF and cFF beams, combining equation (4.2) (4.6) and (4.7), can be expressed as a ratio of measurements and their relevant correction factors:

$$
\begin{aligned}
\frac{N_{D,w,Q}^{\text{FFF}}}{N_{D,w,Q}^{cFF}} = &\frac{\left[\left(\frac{\Delta T_w}{\text{MU}}\right) \cdot c_p \cdot (1-h)^{-1} \cdot k_C \cdot k_{\text{HPC}} \cdot k_{\text{nu}}\right]^{\text{FFF}}}{\left[\left(\frac{\Delta T_w}{\text{MU}}\right) \cdot c_p \cdot (1-h)^{-1} \cdot k_C \cdot k_{\text{HPC}} \cdot k_{\text{nu}}\right]^{cFF}} \\
&\times \frac{\left[(M_{\text{raw}}/\text{MU}) \cdot k_{\text{elec}} \cdot k_{\text{p,T}} \cdot k_{\text{pol}} \cdot k_s \cdot k_v\right]^{cFF}}{\left[(M_{\text{raw}}/\text{MU}) \cdot k_{\text{elec}} \cdot k_{\text{p,T}} \cdot k_{\text{pol}} \cdot k_s \cdot k_v\right]^{\text{FFF}}}
\end{aligned}
$$ (4.9)

4.3. Results and uncertainties

4.3.1. Water calorimetric determination of absorbed dose

Calorimeter correction factors can be found elsewhere (Picard *et al* 2017, de Prez *et al* 2016a). Specific correction factors, relevant for this study, are k_C, k_{HPC} and k_{nu}, given in Table 4-2 and equation (4.6). The influence of the presence of the calorimeter thermostat, was measured and was always smaller than 1.6 %, confirming insignificant effects on the beam qualities.

k_C is based on the average relative excess temperature rise, R_{XS}, simulated for the first 10 calorimeter runs. The excess temperature effects from the presence of the high-purity cell, HPC ($R_{\text{XS,HPC}}$), and probes ($R_{\text{XS,probes}}$) were the same for all cFF and FFF beams
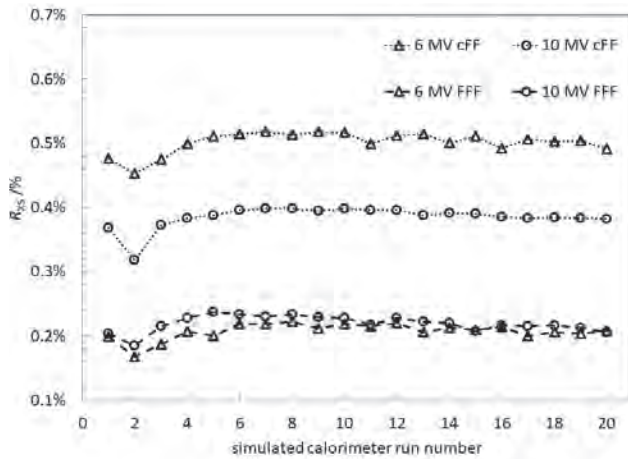
Figure 4-2. The relative excess temperature, R_{xs}, as a result of the 3D-dose profile for the 6 MV cFF, 6 MV FFF, 10 MV cFF and 10 MV FFF photon beams.

within 0.01 %, with values of $R_{XS,HPC}$ = -0.01 % and $R_{XS,probes}$ = 0.28 %, respectively. Differences in R_{XS} due to variations in dose profiles, i.e. $R_{XS,xy\&pdd}$, were significantly larger (Figure 4-2). Thus, k_C mainly varies with the beam dose profiles and its effect is strongest for the flat cFF beams.

The results of the absorbed dose to water measurements are presented in Table 4-2. The accelerator monitor units and dose rate were chosen such that the irradiation time was close to 60 s, one of the input variables of the heat transport calculations. For the VSL ^{60}Co source a start-stop effect resulted in a longer irradiation than the setting of the source timer, also referred to as the timer error (Andreo *et al* 2000).

Table 4-2. Water calorimeter correction factors and measurements.

beam ID	correction factors				calorimeter measurements			
	k_C	k_{HPC}	k_{nu}	set # MU[a]	time /s	runs	D_w /Gy	u_A /%
[60]Co	0.9985	1.0018	1.0000	180	181.0	192	1.94	0.10
6 cFF	0.9950	1.0013	0.9999	575	61.1	24	4.61	0.17
6 FFF	0.9979	1.0013	1.0019	720	61.7	27	5.78	0.18
10 cFF	0.9962	1.0011	0.9999	435	61.9	21	3.79	0.11
10 FFF	0.9978	1.0006	1.0031	1000	58.6	18	8.80	0.11

[a] for ^{60}Co the irradiator timer setting in seconds; for MV x-rays the institute D_{max} in cGy at an SSD of 100 cm; the accelerator dose rate was not always set to its maximum value

The number of runs per beam was chosen such that the Type A standard uncertainty of the repeated calorimeter runs ($\Delta R/R$) was smaller than 0.20 %. The dose per pulse, DPP in mGy, was based on the measured absorbed dose to water and the accelerator pulse rate frequency. The indicated absorbed dose to water, D_w, is the average absorbed dose per calorimeter run.

4.3.2. Ion chamber results

The ion chamber correction factors, specifically relevant for this study are: k_{pol}, k_s and k_v. The other chamber correction factors can be found elsewhere (Andreo *et al* 2000, Almond *et al* 1999). All chamber corrections are applied per individual chamber but in Table 4-4 reported as average per chamber type. It turned out that differences in k_{pol}, k_s and k_v for PTW 30013 and PTW 30012 chamber types, which have identical dimensions, were indistinguishable within their respective standard deviations. These chamber types are reported together. Table 4-3 gives the ^{60}Co ion chamber calibration coefficients averaged per chamber type and their $k_{Q,Q0}$ values. Note that these values are reported as if all chambers were measured directly in water, i.e. without the use of a waterproof sleeve.

Table 4-3: Ion chamber calibration coefficient in ^{60}Co and $k_{Q,Q0}$ factors as if measured directly in water (i.e. without the use of a waterproof sleeve). Values between brackets are the standard deviations, for the individual chambers (2 × PTW 30013, 3 × PTW 30012 and 3 × NE2571).

	N_{D_w,Q_0}	$k_{Q,Q0}$			
%$dd(10)_x$		67.5 %		73.0 %	
TPR$_{20,10}$		0.680	0.675	0.735	0.720
	^{60}Co	6 cFF	6 FFF	10 cFF	10 FFF
PTW 30013	53.34(20)	0.9848(10)	0.9850(10)	0.9747(12)	0.9758(16)
PTW 30012	52.00(60)	0.9870(9)	0.9879(10)	0.9789(7)	0.9809(13)
NE2571	45.07(19)	0.9873(11)	0.9891(12)	0.9797(7)	0.9838(12)

Table 4-4. Ion chamber correction factors. Values between brackets are the standard deviations for the individual chambers (2 × PTW 30013, 3 × PTW 30012 and 3 × NE2571).

		^{60}Co	6 cFF	6 FFF	10 cFF	10 FFF
	DPP / mGy	–	0.19	0.47	0.31	0.75
k_s	PTW 30013/30012	1.0004(1)	1.0028(2)	1.0061(1)	1.0045(2)	1.0101(4)
	NE2571	1.0010(1)	1.0035(1)	1.0075(2)	1.0051(2)	1.0127(4)
k_{pol}	PTW 30013/30012	1.0004(1)	1.0005(1)	1.0006(2)	1.0005(3)	1.0008(3)
	NE2571	0.9991(2)	0.9992(2)	0.9993(3)	0.9994(3)	0.9991(2)
k_v	PTW 30013/30012	1.0000	0.9999	1.0033	0.9998	1.0054
	NE2571	1.0000	0.9999	1.0036	0.9998	1.0059

The polarity correction was measured for all chambers and is reported for negative potential applied to the central electrode (regardless of the actual potential used). The values obtained in this study confirmed that k_{pol} is independent of photon beam quality or dose rate for these chamber types (McEwen 2010, Seuntjens *et al* 2000). The reported uncertainty on k_{pol} per chamber type is estimated to be 0.06 %. and based on the quadratic sum of the largest standard deviation of the values for the individual chambers, 0.03 %, and the uncertainty in the charge measurements, 0.05 %.

Figure 4-3 shows the recombination correction as a function of dose per pulse, DPP in mGy. Values are given in Table 4-4. k_s was measured for the applied chamber voltage, i.e. 300 V (CEN) for the chambers owned by VSL and 350 V (CEP) for the chambers owned by the Netherlands Cancer Institute. To enable comparison of all chambers the measured k_s of the chambers owned by the Netherlands Cancer Institute were normalized to 300 V as follows. k_s was determined with the method described by Weinhous and Meli (1984) and also, using the same two points, by applying a Jaffé plot as described by, e.g. Burns and McEwen (1998) and Bruggmoser *et al* (2007). The agreement of k_s determined with both methods was always better than 0.05 % and, in most cases, better than 0.02 %. Using a two-point Jaffé plot k_s values of the chambers measured at a negative bias of 350 V were normalized to k_s at 300 V such that k_s could be compared between the chambers. The reported uncertainty on the k_s per chamber type is estimated to be 0.08 %, based on the quadratic sum of largest standard deviation of the values for the individual chambers, 0.04 %, and the uncertainty in the charge measurements, 0.07 %.

The correction for volume averaging, k_v, is given in Table 4-4 The dimensions of the chamber air cavity are taken from Andreo *et al* (2000) neglecting any reduction in dose response near the chamber stem (Butler *et al* 2015). The uncertainty on k_v is estimated to be 0.10 % and based on the chamber geometry, positioning, and the measured lateral profiles in the direction of the thimble. Contribution in the direction of the chamber's diameter, always smaller than 0.01 %, was neglected and added to the uncertainty.

4.3.3. Uncertainties in $k_{FFF,cFF}$
The combined standard uncertainty is determined according to the Guide to the Expression of Uncertainty in Measurement (JCGM 2008). Uncertainty budgets for absorbed dose to water calibrations in ^{60}Co and MV-photon beams are given elsewhere (de Prez *et al* 2016a, Picard *et al* 2017). The uncertainty budget for *R* determined with equation (4.3) is given in Table 4-5. Uncertainty budgets for *R* in equation (4.3) of ion chambers in MV-photons beams in this study.
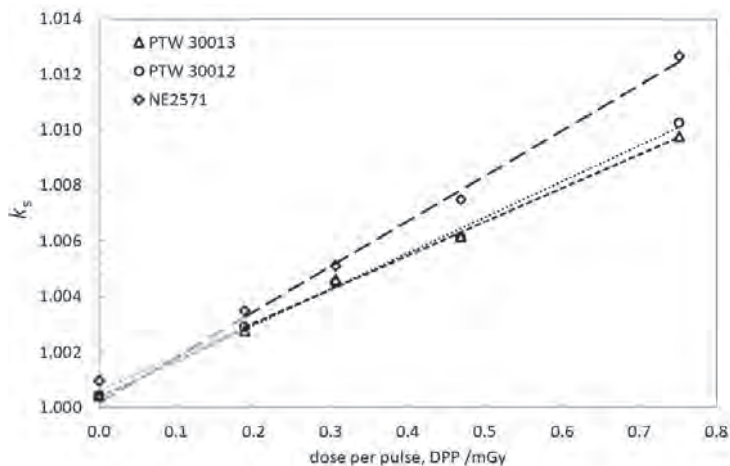
Figure 4-3. Recombination correction, k_s, for the three chamber types used in this study as a function of dose per pulse, DPP in mGy (see Table 4 4). The black dotted lines are linear fits through the points measured in the accelerator beams, extrapolated in grey to the vertical axis. The points at the vertical axis are k_s measured for ^{60}Co and assumed only to be a result of initial recombination.

Most uncertainty contributions cancel (partially) due to correlations in the measured and calculated quantities found in both the nominator and denominator of equation (4.9). Most of these correlations result from the use of the same instruments for the measurements in the cFF and the FFF beams. The main remaining contributions are the Type A uncertainty of the calorimeter measurements, D_w/MU, and ion chamber measurements including their corrections. The effect on the input data for the heat transport model, used to calculate k_C (from $R_{XS,xy\&pdd}$) is estimated to be smaller than 0.10 %. An additional uncertainty contribution for the cross-calibration of the chambers inside the calibration phantom was estimated to be 0.07 %. Uncertainties for SSD and depth variations inside the calibration phantom were considered negligible.

The reproducibility of the calorimetric D_w measurements in ^{60}Co before and after the measurements at the Netherlands Cancer Institute was better than 0.1 %, providing confidence on the performance of the HPC preparation and the long-term stability of the water calorimeter measurements. However, this was not taken into account since we are only interested in the short term D_w determination performed during a couple of days.

Uncertainty contributions for the normalization of the cFF k_Q to the FFF beam quality (equation (4.3) and Table 4-1) was omitted because this normalization is based on convention by the published values of the relevant Codes of Practice.

Table 4-5. Uncertainty budgets for R in equation (4.3) of ion chambers in MV-photons beams in this study.

source of uncertainty	6 MV		10 MV	
	cFF	FFF	cFF	FFF
D_w/MU, Type A (Table 4-2)	0.17	0.18	0.11	0.11
ratio of calorimeter k_C (heat conduction)	< 0.10			
ratio of calorimeter k_{nu} (radial non-uniformity)	0.05			
charge measurement (M_{corr}/MU), Type A	0.07			
ratios of k_s (saturation) and k_p (polarity)	0.07			
ratio ion chamber k_v (volume averaging)	0.05			
ratio of ion chamber $k_{p,T}$ and $k_{\%RH}$	0.05			
cross-calibration charge measurement (M_{corr}/MU), Type A	0.07			
combined: ratio measurement in the MV-photon beams	0.25	0.25	0.21	0.21
combined: ratio of k_Q in FFF-cFF beams R from eq. (4.3)	0.35		0.30	

4.3.4. Comparison of k_Q factors within FFF-cFF beam pairs

Table 4-6 gives the results for $\Delta k_{FFF,cFF}$ according to equation (4.5). Differences between cFF and FFF beam pairs are always smaller than the standard uncertainty, except for NE2571 at the 10 MV beam for %$dd(10)_x$, for which $Q = Q'$ in equation (4.4) and $k_{Q',Q}^{cFF} = 1$ (see Table 4-1). In all cases, differences are smaller than two standard uncertainties. In addition, differences between FFF-cFF beam pairs are smaller than the standard uncertainties ($k = 1$) reported by the protocols mentioned in Table 4-6: for the TPR$_{20,10}$ based CoPs this is 0.4 % for NCS-18 (Aalbers *et al* 2008), 1.0 % for TRS-398 (Andreo *et al* 2000). The comparison based on %$dd(10)_x$ is independent of the protocol used since the Elekta FFF-cFF beam pairs are energy-matched with respect to this beam quality specifier.

Table 4-6: $\Delta k_{FFF,cFF}$ conform equation (4.5) for the FFF-cFF beam pairs in an Elekta Versa HD accelerator.

chamber type	$\Delta k_{FFF,cFF}$ /%, 6 MV			u_k	$\Delta k_{FFF,cFF}$ /%, 10 MV			u_k
	%$dd(10)_x$	TPR$_{20,10}$		/%	%$dd(10)_x$	TPR$_{20,10}$		/%
		NCS-18	TRS-398			NCS-18	TRS-398	
PTW 30013	0.02	−[a]	-0.04		0.12	−[a]	-0.19	
PTW 30012	0.09	0.03	0.06	0.35	0.21	−0.11	−0.02	0.30
NE2571	0.18	0.12	0.15		0.42	0.10	0.19	

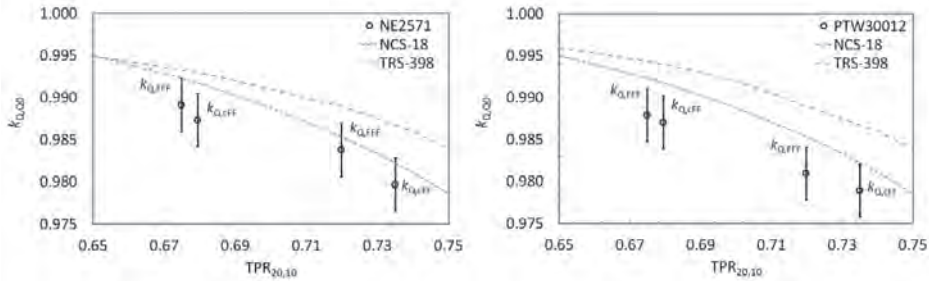[a] NCS-18 doesn't provide k_Q data for this chamber type.

Figure 4-4. Measured k_Q factors for the two NE2571 (left) and PTW 30012 (right) type chambers in relation to the $\text{TPR}_{20'10}$ based CoPs applied in this study. The error bars represent the standard uncertainties ($k = 1$) given in Table 4 5. Note that both the TRS-398 and NCS-18 k_Q factors include a correction for the presence of the PMMA sleeve which is smaller than 0.1 %, while the measured k_Q factors obtained in this study do not. The standard uncertainty of the k_Q factor on the NCS-18 and TRS-398 curve are 0.4 % and 1.0 %, respectively.

Figure 4-4 shows the k_Q factors obtained in this study in relation to the k_Q factors provided by NCS-18 and TRS-398. k_Q values provided in this study were measured without the influence of a PMMA sleeve. However, NCS-18 and TRS-398 provide k_Q factors for Farmer-type chambers including a 1 mm and 0.5 mm PMMA sleeve, respectively. The effect of a 1 mm PMMA sleeve at ^{60}Co, 6 MV and 10 MV is known to be small and between -0.05 % and -0.10 % for Farmer-type chambers (Ross and Shortt 1992, Andreo *et al* 2000). These effects have not been corrected for the measurements shown in Figure 4-4.

4.4. Discussion and conclusion

The application of existing k_Q factors for flattening filter free (FFF) photon beams based on existing codes of practice, using different beam quality specifiers is not trivial. Some Monte Carlo studies assumed a sole dependence on stopping power ratios and disagreed depending on the used beam models (Xiong and Rogers 2008, Dalaryd *et al* 2014). Lye *et al* (2016) showed good agreement in measurements between $\%dd(10)_x$ and $\text{TPR}_{20,10}$ based codes of practice (McEwen *et al* 2014, Almond *et al* 1999, Andreo *et al* 2000) and confirmed this with Monte Carlo simulations for realistic chambers and beams. In all cases the volume averaging effect of chambers in the FFF beams was treated independently from k_Q. In the Monte Carlo studies it was either ignored by only considering stopping power ratios (Xiong and Rogers 2008) or included in both the calculated dose to the chamber cavity and dose to an equivalent water volume (Lye *et al* 2012). However, when performing ion chamber measurements it is essential that the volume averaging correction is applied as a separate correction in addition to the existing code of practice in a similar way as implemented by the TG-51 addendum (McEwen *et al* 2014). A recent publication

by the IAEA (Palmans *et al* 2017) implemented k_v as an integral part of the FFF beam's k_Q. The approach in the current study assumes that the chamber perturbation, excluding volume averaging effects, in FFF beams compared to cFF beams remains unchanged and that the volume averaging effect for cFF beams is negligible.

Despite the relevance of the mentioned Monte Carlo studies and other methods, they are limited by the models for both ion chambers and accelerator beams. Therefore, direct measurement of k_Q factors with primary standards are essential to understand the individual behaviour of physical chambers in real clinical accelerators. This is the first study that directly measured and compared k_Q factor of ion chambers in clinical flattening filter free (FFF) and conventional flattening filter (cFF) MV-photon beams. This was done with a transportable absorbed dose to water primary standard, a water calorimeter, described elsewhere (de Prez *et al* 2016a, Picard *et al* 2017). The measurements were performed in energy-matched FFF-cFF beam pairs of 6 MV and 10 MV-photon beams of an Elekta Versa HD accelerator with a selection of three Farmer-type chambers of in total 8 serial numbers. Measured k_Q factors in the beam pairs were corrected for volume averaging in the direction of the cavity length and normalized to the FFF beam quality, expressed in $TPR_{20,10}$, in combination with either NCS-18, based on measured k_Q factors (Aalbers *et al* 2008), or IAEA TRS-398, based on calculated k_Q factors (Andreo *et al* 2000). Differences between k_Q of the FFF and cFF beams were smaller than 0.19 % for $TPR_{20,10}$ based protocols NCS-18 and TRS-398 and within the standard uncertainties of 0.35 % for 6 MV and 0.30 % for 10 MV beams. In contrast to the study by Xiong and Rogers, the biggest difference of 0.42 % was found for the NE2571 chambers at 10 MV for k_Q when $\%dd(10)_x$ was applied, however within the expanded uncertainty of the measurements. Therefor the difference is not considered significant.

This study was not able to reproduce the differences of 0.5 % to 0.7 % between k_Q factors in two pairs of FFF and cFF beams when applying $TPR_{20,10}$ as a beam quality specifier, predicted by the Monte Carlo study of Xiong and Rogers (2008). However, it confirms the results reported by Lye *et al* (2016) who performed ion chamber measurements based on TRS-398, TG-51 and Monte Carlo calculations. Lye *et al* concluded that, despite a change in stopping power ratios for FFF beams compared to cFF beams, the addition of a thin metal filter, at the position of the flattening filter, produces a beam that is similar enough in spectra compared to cFF beams.

Based on measurements in this study and specifically for the combination of accelerator type, beams and ion chambers, the authors conclude that the k_Q factors for cFF beams based on $TPR_{20,10}$ and based on $\%dd(10)_x$ can be applied for FFF beams within the specified measurement uncertainties of 0.7 % ($k = 2$). In addition, the user must be aware of the volume averaging effect due to radial non-uniformity and correct for this accordingly.

4

5

Commissioning of a water calorimeter as a primary standard for absorbed dose to water in magnetic fields

Abstract

MRI guided radiotherapy (MRgRT) devices are currently in clinical use. Detector responses are affected by the magnetic field and need to be characterized in terms of absorbed dose to water, D_w, against primary standards under these conditions. The aim of this study was to commission a water calorimeter, accepted as the Dutch national standard for D_w in MV-photons and to validate its claimed standard uncertainty of 0.37 % in the 7 MV-photon beam of a pre-clinical MRI-linac in a 1.5 T magnetic field. To evaluate the primary standard on a fundamental basis, realisation of D_w at 1.5 T was evaluated parameter by parameter. A thermodynamic description was given to demonstrate potential temperature effects due to the magneto-caloric effect (MCE). Methods were developed for measurement of depth, variation in detector distance and beam output in the bore of the MRI-linac. This resulted in D_w measurements with a magnetic field of 1.5 T and, after ramp-down, without magnetic field. It was shown that the measurement of ΔT_w and calorimeter corrections are either independent of or can be determined in a magnetic field. The chemical heat defect, h, was considered zero within its stated uncertainty, as for 0 T. Evaluation of the MCE and measurements done during magnet ramp-down, indicated no changes in the specific heat capacity of water. This study confirmed that the uncertainty for measurement of D_w with a water calorimeter in a 1.5 T magnetic field is estimated to be the same as under conventional reference conditions. The VSL water calorimeter can be applied as a primary standard for D_w in magnetic fields and is currently the only primary standard operable in a magnetic field that provides direct access to the international traceability framework.

5.1. Introduction

Several, integrated MRI guided radiotherapy (MRgRT) devices are under development or in clinical use (Keall *et al* 2014, Fallone 2014, Mutic and Dempsey 2014, Lagendijk *et al* 2014b). Dosimetry in the presence of a magnetic field, *B*, is not trivial because the energy deposition changes the secondary electrons trajectories that are influenced by the Lorentz force. Dose distributions change e.g. in build-up and penumbra regions, in the central beam region and at material or tissue interfaces (Raaijmakers *et al* 2008, Raaymakers *et al* 2004, Woodings *et al* 2018, Oborn *et al* 2010). The magnitude of these dose effects depends on the magnetic field strength and its orientation relative to the photon beam, material differences and density inhomogeneities. Not only the dose distribution is affected but also the response of commonly used dosimeters in terms of their calibration coefficient as e.g. described by van Asselen *et al* (2018). Traditionally photon beams in radiotherapy are calibrated by collecting charge inside the air cavity of an ion chamber (Andreo *et al* 2000, McEwen *et al* 2014, Aalbers *et al* 2008). Ion chamber response is affected by the magnetic field and depends on the magnetic field direction and the direction of the photon beam in relation to the orientation of the ion chamber (Meijsing *et al* 2009, Reynolds *et al* 2013, Smit *et al* 2013). The quantity of absorbed dose to water, D_w, in the unit J kg^{-1} (Seltzer *et al* 2011), is defined as *the mean energy imparted*, $d\bar{\varepsilon}$, *by ionizing radiation to water of mass* d*m*:

$$D_{\mathrm{w}} = \frac{d\bar{\varepsilon}}{dm}. \tag{5.1}$$

Where the energy imparted, $d\bar{\varepsilon}$ is the sum of all energy deposits in the volume of mass d*m*. As photons do not have electrical charge and the interaction coefficients of photons and electrons with matter is unaffected by the magnetic field (Szymanowski *et al* 2015) only the electron fluence is affected by the magnetic field. The definition of the D_w in equation (5.1) therefore only depends on the total energy imparted by radiation and is suited to define the quantity of absorbed dose also in the presence of a magnetic field.

The goal in reference dosimetry is to determine D_w at a reference point in a homogeneous water phantom. This D_w value is subsequently used as a starting point for accelerator calibration and commissioning, usually by means of ion chambers. The most fundamental and direct method to calibrate ion chambers for reference dosimetry in terms of D_w in a magnetic field is against a *primary standard*[11] which is modified and characterized for

5

---

11 *primary standard*: a measurement standard obtaining a measurement result without relation to a measurement standard for a quantity of the same kind (OIML 2007).

application in a magnetic field. Alternatively, a detector is needed with a response that is not affected by the magnetic field or can be characterized accordingly, so it can be calibrated without magnetic field and used to calibrate ion chambers in a magnetic field. However, methods applying these detectors also need to be validated against a primary standard. This emphasises the need of a primary standard for ionizing radiation in the presence of magnetic fields.

Methods used in primary D_w determination in high-energy photon beams, described e.g. by (Seuntjens and Duane 2009, Andreo *et al* 2000), are: (1) standards using ionization chambers, (2) standards using ferrous sulphate (Fricke) solution, (3) standards based on either graphite or water calorimetry. Water calorimetry is based on the underlying assumption that energy imparted by ionizing radiation per unit of mass ($d\bar{\varepsilon}/dm$) is transferred to specific heat (dq) and ultimately appears as a temperature rise of water, dT_w, which leads to the fundamental relation:

$$D_{\mathrm{w}} = \mathrm{d}q = c_p \cdot \mathrm{d}T_{\mathrm{w}}, \qquad (5.2)$$

with c_p the specific heat capacity of water. If the assumption of complete energy conversion from deposited dose to heat is fulfilled, or if any discrepancy is well understood and taken into account, the calorimeter can be considered as the most fundamental and absolute method of the available techniques for the measurement of D_w (Seuntjens and Duane 2009). In magnetic fields, material or density inhomogeneities near the reference point affect the electron fluence and are undesired (O'Brien *et al* 2017). Therefore, water calorimetry appears to be the most suitable primary measurement method for application in magnetic fields.

VSL developed a new water calorimeter as a primary standard for absorbed dose to water. It was designed and built for on-site measurements in photon beams of ^{60}Co, kV x-ray and MV-photon beams, including MRI-incorporated treatment machines (de Prez *et al* 2016a). The uncertainty for ^{60}Co and MV-photon beams was established at 0.37 % ($k = 1$). The agreement for D_w without magnetic field (i.e. at 0 T) and its uncertainty was international accepted by taking part in BIPM[12] key comparisons (Büermann *et al* 2016, Picard *et al* 2017, Kessler *et al* 2018). The calorimeter has demonstrated its applicability on-site for conventional flattened and flattening filter free (FFF) high-energy photon beams (de Prez *et al* 2018b). Based on the preliminary assessment of the calorimeter temperature sensors

---

12 The Bureau Internationales des Poids et Mesures, BIPM in Sévres, is an international organization established by the Metre Convention, through which Member States act together on matters related to measurement science and measurement standards (https://www.bipm.org/).

in a magnetic field, it was proposed that the uncertainty for MV-photon beams at 1.5 T would not exceed that at a conventional 0 T field. Preliminary results were presented earlier (de Prez *et al* 2016b) and showed the feasibility of water calorimetry in the presence of a magnetic field.

The current study describes the characterization and commissioning of the VSL water calorimeter in the presence of a 1.5 T magnetic field of a 7 MV Elekta Unity MRI-linac. The aim of this study is to validate the claimed uncertainty of 0.37 % ($k = 1$) for determination for absorbed dose to water in MV-photon beams in the presence of a magnetic field.

5.2. Materials and methods

5.2.1. The wide bore hybrid MRI-linac system

The pre-clinical Elekta Unity hybrid MRI-linac system used in this study comprises a modified 1.5 T Philips wide bore MRI with 70 cm diameter and an Elekta 7 MV standing wave linear accelerator producing a flattening filter free (FFF) photon beam (Raaymakers *et al* 2009, Lagendijk *et al* 2014, Woodings *et al* 2018). The beam quality expressed in TPR$_{20,10}$ has a value of 0.701 and is, within its standard uncertainty independent of the presence of the magnetic field (van Asselen *et al* 2018). The accelerator is mounted on a ring 'inside' a low-field toroid to magnetically decouple it from the MRI (Overweg *et al* 2009). The ring allows for continuous rotation with an accelerator source to iso-centre distance of 143.5 cm. There is a beam-portal through the magnet and cryostat, however, the beam still passes through liquid helium and the cryostat wall. The described configuration provides for a transverse magnetic field relative to the beam. The linac is equipped with a multi-leaf collimator and an electronic portal imaging device (EPID) on the ring behind the beam exit side. A beam stopper is mounted behind the EPID. The MRI-linac is not equipped with conventional positioning tools such as alignment lasers, front pointer or a light field.

5.2.2. The VSL water calorimeter in the MRI-linac

The VSL calorimeter, shown in Figure 5-1 and described elsewhere in detail (de Prez *et al* 2016a), is constructed of non-ferromagnetic materials for the purpose to be operated in a magnetic field. It contains a cylindrical water phantom operated at 4 °C to avoid convection due to temperature gradients. The beam enters the calorimeter at the centre of a removable lid through a square radiation window. A cylindrical high-purity water cell (HPC) made of thin-walled glass contains two negative temperature coefficient (NTC) thermal resistors, so called thermistors, glued at the tip of miniature glass pipettes. These are used to measure the radiation induced temperature change in water, ΔT_{w}. The

5

removable thermostat lid
A. 11 cm × 11 cm entrance window
B. PU foam insulation
C. laminar passive heat sink
D. actively cooled PE tubing
E. aluminium heat sink

expanded view of radiation
entrance window (lid closed)
R. 10 mm PU foam insulation
S. laminar passive heat sink
(5 × 0.1 mm alu + 4 × 2 mm PU foam)
T. aluminium heat sink
U. 2.8 mm PMMA radiation entrance window

water phantom
F. aluminium phantom lid
G. O-ring to seal the phantom
H. PMMA radiation entrance window
I. PMMA detector support
J. high-purity water cell with 2 thermistors
K. phantom heat-exchanger

calorimeter thermostat
L. thermostat heat-exchanger
M. PU foam insulation
N. actively cooled PE tubing
O. aluminium heat sink
P. stirring device (hydraulic or electric)
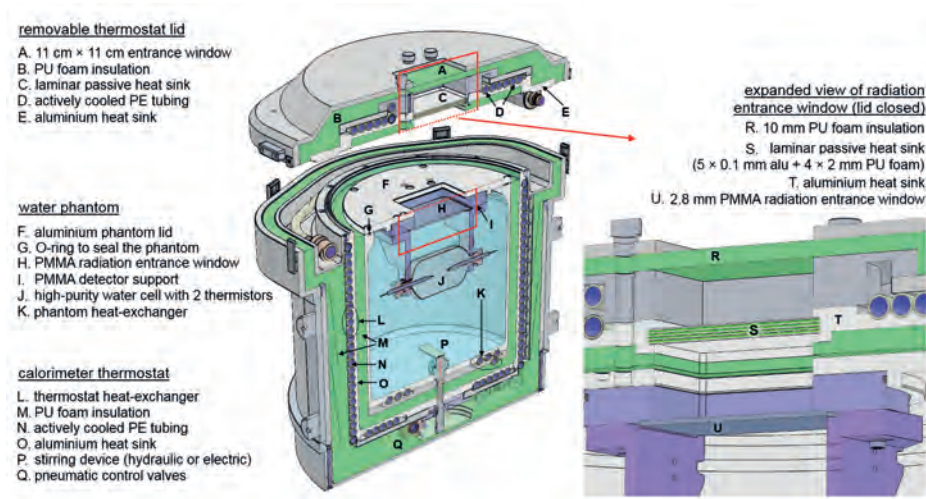Q. pneumatic control valves

Figure 5-1. Cross-section of the calorimeter described in more detail by de Prez *et al* (2016a). It contains the high-purity cell at a measurement depth of 10 cm (left) and includes an expanded view of the radiation entrance window (right).

thermistor probes are mounted 10 mm apart inside the HPC filled with argon-saturated ultra-pure water. Ion chambers can be calibrated directly inside the calorimeter water phantom. This is accomplished by using a detector mount that can accommodate either the calorimeter HPC or ion chambers on a replaceable detector mount.

Figure 5-2 shows the water calorimeter inside the 70 cm MRI-linac bore with the couch removed. It was mounted on an independent bridge with legs resting on the floor at both sides of the treatment machine (see Figure 5-2 (B)). The calorimeter was aligned in the centre of the beam using the EPID projection images providing a resolution of 0.2 mm at the point of measurement. The lateral position of the calorimeter was repeatedly verified using the EPID images at a gantry angle of 0°, i.e. with a vertical beam. Its SDD was determined to be 139.3 cm, i.e. 4.2 cm above iso-centre, using EPID images at a gantry angle of 90°. Changes in calorimeter height were checked regularly with two laser-distance meters (Leica Disto D810). These were positioned, with the laser beam in horizontal orientation, on a tripod outside the bore in low magnetic field (see Figure 5-2 (G)). The horizontal laser beams from the distance meters entering the bore were deflected downwards by 90° to measure the distance to the calorimeter reference plane and, with the calorimeter placed to the side, to the bottom of the bore (see Figure 5-2 (F)). The detector mount (Figure 5-1(I)) was enabled also to rotate 90º remotely, i.e. without the need to access the water phantom. With this set-up the variation in SDD was measured with an uncertainty of 0.3 mm ($k = 1$), equivalent to better than 0.05 % on the determination of D_w.
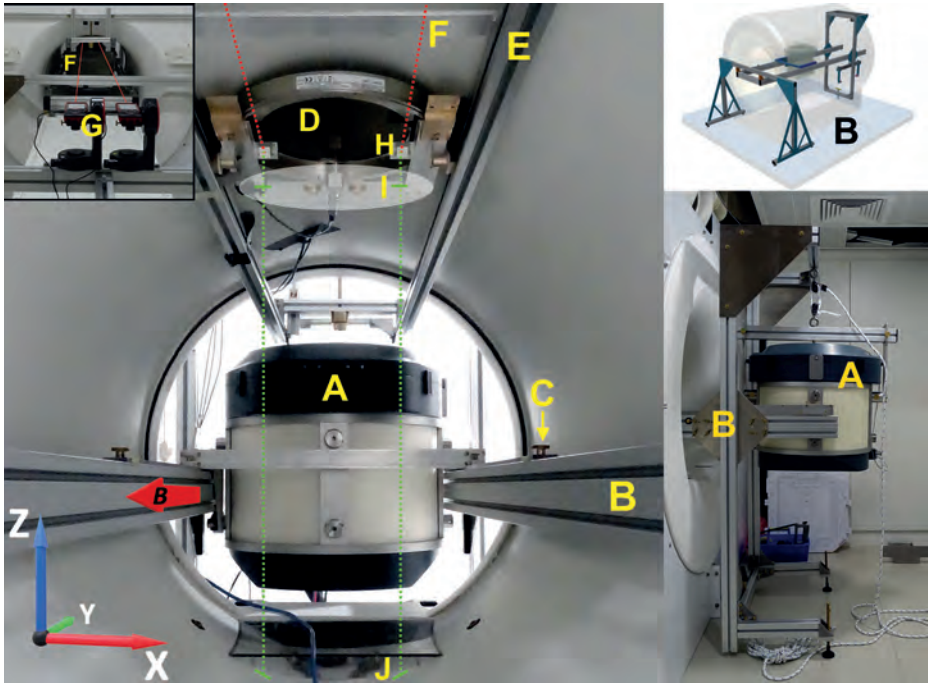
Figure 5-2. The water calorimeter phantom (A) positioned on two rails of a bridge (B), suspended outside the MRI-linac and fixed Y direction by two bolts on rulers (**C**) at both sides. An independent transmission monitor (D), fixed against the inside of the bore, on rails of a second bridge (E) served as the vertical reference point. Two laser-beams (F) from laser-distance meters outside the bore (G) are deflected in a right-angle downwards by 45° mirrors (H) to measure the vertical displacement of the calorimeter reference plane (I) in relation to the bottom of the bore (J).

5.2.3. Beam output monitoring

An external thin-window transmission monitor chamber (PTW 34014) was positioned in the MRI-linac bore, above the water calorimeter, as shown in Figure 5-2 (D). It was suspended from a second independent frame (Figure 5-2 (E)) that was not in direct mechanical contact with the frame of the calorimeter. In this study, no additional build-up material was placed on the entrance side of the transmission monitor to avoid any material inhomogeneities close to its sensitive volume. In an experiment prior to the calorimeter measurements this was found to be an improved method compared to the monitor setup equipped with 2 mm additional build-up material. Sufficient electron build-up from the MRI cryostat wall was presumed to reach the monitor chamber in order to justify the removal of the additional 2 mm build-up material. The relative standard deviation of linac output at 1.5 T measured with the transmission monitor compared to a reference ion chamber inside a water phantom was 0.16 % over a period

of 4 days. The internal monitor of this particular pre-clinical MRI-linac was not used because it showed leaking behaviour based on instabilities that followed the ambient pressure.

5.2.4. Calorimetry in magnetic fields

The water calorimetric determination of absorbed dose, D_w, at the reference point in water, requires measurement of the radiation induced temperature change in water, ΔT_w, multiplied by the specific heat capacity of water, c_p (4207.5 J kg^{-1} K^{-1} at 4 °C) and several correction factors, correcting for chemical heat defect, h, undesired conductive heat flow, k_C, the presence of the calorimeter glass cell, k_{HPC} and geometrical deviations from reference conditions, k_R:

$$D_{\mathrm{w}} = \Delta T_{\mathrm{w}} \cdot c_p \cdot (1-h)^{-1} \cdot k_{\mathrm{C}} \cdot k_{\mathrm{HPC}} \cdot k_{\mathrm{R}}. \qquad (5.3)$$

Traditionally, the absorbed dose to water with calorimeters is determined without a magnetic field. Operation in a magnetic field requires understanding of the effect of the magnetic field on measured temperature change per unit of gray (Gy). Any of the factors on the right-hand side of equation (5.3) could potentially be affected by the magnetic field. For commissioning and characterisation of the water calorimeter as a primary standard for D_w determination in the presence of magnetic fields, these factors are addressed in the following paragraphs and their relevance is described in relation to the presence or absence of a magnetic field.

5.2.4.1. Measurement of the water temperature change, ΔT_w

The radiation induced temperature change of water, ΔT_w, is measured by recording the resistance change of two thermistors, each connected to their own high-precision digital-multimeter (DMM). In a previous study the known magneto-resistance effect (MRE) on the resistance measurements was evaluated for two thermistor probes (de Prez *et al* 2016a). This was done between the poles of an electromagnet with the miniature glass pipettes containing thermistors, held perpendicular to the direction of the magnetic field (⊥). For a 1.5 T magnetic field a resistance change, $\Delta R_{\mathrm{MR\perp}}/R$, between -43 ppm and -24 ppm was observed for five temperatures between 0 °C and 23 °C. This was -38 ppm at 4.0 °C with a standard uncertainty of 4 ppm. For the measurement at 0 °C a melting-point of water was created by placing the thermistor probe in melting ice, an ice-point. This created a stable and constant temperature during half an hour in which the experiment took place and before the heat from the surroundings and the electromagnet melted the available ice. The variation of MRE over the measured range between the ice-point (at 0 °C) and room temperature was small, i.e. +19 ppm. Essential for the current study, however not reported

earlier was the inclusion of the ice-point, where the heat capacity of water (at the solid-liquid transition) is not defined. This showed agreement with the MRE in the liquid phase, above 0 °C. This confirmed that the thermistor resistance change in water at 4 °C was only caused by MRE and not by a change of the specific heat capacity of water explained later.

The variation or MRE over the operational temperature range of the calorimeter (i.e. ~3.8 °C to ~4.2 °C) was shown to be negligible, resulting in negligible effect on the calorimetric measurement of ΔT_{w}.

However, measurement of the MRE with the probes in parallel direction between the electromagnet's poles was not possible due to the restricted space. To verify the effect of the magnetic field direction on ΔT_{w}, in the current study measurements were done in the bore of the MRI-linac with the thermistor probes both perpendicular ($\perp$) and in parallel ($\parallel$) direction to the magnetic field. The resistance change, $(R_{\text{MR}\parallel} - R_{\text{MR}\perp})/R_{\text{MR},\parallel}$, of the two thermistors was measured while rotating them by 90°.

5.2.4.2. Water temperature effects in magnetic fields

To understand the effect of the magnetic field, B, on the calorimetric determination of D_{w} and the actual water temperature, T_{w}, the subject is approached from the concept of entropy and the laws of thermodynamics. Franco *et al* (2018) gave an overview of the so-called magneto-caloric effect (MCE) in materials. This is also known as 'adiabatic demagnetization'. The MCE gives rise to an adiabatic temperature change due to the application or removal of an external magnetic field. It is defined as 'the reversible temperature change produced upon a magnetic field change in an adiabatic process'. It can be shown that the specific entropy, s, at constant pressure, p, can be expressed as a function of water temperature, T_{w}, and magnetic field, B, i.e. s(T_{w}, B). It follows that:

$$\mathrm{d}s = \left(\frac{\delta s}{\delta T_{\text{w}}}\right)_{p,B} \mathrm{d}T_{\text{w}} + \left(\frac{\delta s}{\delta B}\right)_{p,T_{\text{w}}} \mathrm{d}B. \tag{5.4}$$

The 2$^{\text{nd}}$ law of thermodynamics defines entropy change, ds, for a reversible adiabatic process, such as the MCE, as:

$$\mathrm{d}s = \frac{\mathrm{d}q}{T_{\text{w}}}. \tag{5.5}$$

Where the specific heat flux, dq, is expressed in J kg^{-1}, and from equations (5.4) and (5.5) it follows that:

$$dq = T_{\mathrm{w}} \, ds = T_{\mathrm{w}} \cdot \left(\frac{\delta s}{\delta T_{\mathrm{w}}}\right)_{p,B} dT_{\mathrm{w}} + T_{\mathrm{w}} \cdot \left(\frac{\delta s}{\delta B}\right)_{p,T_{\mathrm{w}}} dB. \tag{5.6}$$

The specific heat capacity of water at constant pressure and constant magnetic field, $c_{p,B}$, is defined as $(dq/dT_{\mathrm{w}})_{p,B,}$ $(= T_{\mathrm{w}} \, \delta s/\delta T_{\mathrm{w}})$ thus, from this and equation (5.5) and (5.6) follows:

$$dq = c_p \cdot dT_{\mathrm{w}} + T_{\mathrm{w}} \cdot \left(\frac{\delta s}{\delta B}\right)_{p,T_{\mathrm{w}}} dB. \tag{5.7}$$

If the magnetic field is constant during a calorimeter measurement, with $dB = 0$ T and $c_{p,B} = c_p$, then equation (5.7) is reduced to equation (5.2). This shows that with a constant magnetic field, B, a heat flux entering the system, the energy imparted by ionizing radiation causes a temperature change which only depends on the specific heat capacity of water. Variation of the magnetic field during calorimetry is therefore not recommended since this could give potential erroneous results in the measurement of D_{w}.

5.2.4.3. Expected water temperature change due to the magneto-caloric effect
Measurement of the water temperature, T_{w}, was done during magnet ramp-down from 1.5 T to 0 T to indicate any changes in c_p, if this would occur. The second term on the right of equation (5.7) is governed by the MCE. It shows that changing the magnetic field during calorimetry could lead to a change in water temperature that is not only the result of absorption of ionizing radiation but also of the MCE. Franco *et al* (2018) showed that on the application of a magnetic field strength, H (in A m^{-1}), under adiabatic conditions at temperature T_{w}, a temperature change $dT_{\mathrm{w,ad,CE}}/dH$ is expected that is related to the vacuum permeability μ_0 $(= 4 \cdot \pi \cdot 10^{-7}$ N A$^{-2})$ and the specific magnetization per unit of temperature, $(\delta m/\delta T)_B$ in A m^2 kg^{-1} K^{-1}, at constant magnetic field strength, H:

$$dT_{\mathrm{w,ad,MCE}} = -\frac{\mu_0 \cdot T_{\mathrm{w}}}{c_p} \cdot \left(\frac{\delta m}{\delta T_{\mathrm{w}}}\right)_{p,H} dH. \tag{5.8}$$

With the magnetic field strength $H = B/(\mu_0(1 + \chi_v))$ and involving the dimensionless volume magnetic susceptibility, χ_v, this can be written as:

$$dT_{\mathrm{w,ad,MCE}} = -\frac{T_{\mathrm{w}}}{(1+\chi_v) \cdot c_p} \cdot \left(\frac{\delta m}{\delta T_{\mathrm{w}}}\right)_{p,B} dB. \tag{5.9}$$

The specific magnetization, m, can be derived from the material's magnetization, M in A m^{-1}, which has a relation with the magnetic field strength and the volume magnetic susceptibility, c_v:

$$m = \frac{M}{\rho} = \frac{\chi_v \cdot H}{\rho} = \frac{\chi_v \cdot B}{\rho \cdot \mu_0 \cdot (1+\chi_v)}. \tag{5.10}$$

The volume magnetic susceptibility for water is very small ($-9 \cdot 10^{-9}$). Therefore, at constant magnetic field, B, the specific magnetization at constant magnetic field, $(\delta m/\delta T)_B$, can be expressed as:

$$\left(\frac{\delta m}{\delta T_w}\right)_B = \frac{B}{\rho \cdot \mu_0 \cdot (1+\chi_v)^2} \cdot \left(\frac{\delta \chi_v}{\delta T_w}\right)_B .$$
(5.11)

Combining this with equation (5.9), the adiabatic temperature change due to the MCE can be obtained with:

$$\Delta T_{w,ad,MCE} = -\int_{B_{initial}}^{B_{final}} \frac{T_w \cdot B}{c_p \cdot \mu_0 \cdot \rho \cdot (1+\chi_v)^2} \cdot \left(\frac{\delta \chi_v}{\delta T_w}\right)_B dB .$$
(5.12)

For diamagnetic materials, such as water, the temperature dependence of $(\delta \chi_v/\delta T)_B$ is small and constant over the range between 0 °C and 100 °C with a value of $[\delta \chi_v/\delta T] = -1.1 \cdot 10^{-9}$ K^{-1} (Rumble *et al* 2018). In this study, a calorimeter temperature drift was recorded during ramp-down from 1.5 T of the MRI-magnet from 1.5 T to 0 T. If the heat capacity of water at 1.5 T is the same as at 0 T, this would result in an adiabatic temperature change of:

$$\Delta T_{w,ad,MCE} = \frac{T_w \cdot B^2}{2 \cdot c_p \cdot \mu_0 \cdot \rho} \cdot \left[\frac{\delta \chi_v}{\delta T_w}\right] = -0.06 \ \mu K .$$
(5.13)

5.2.4.4. The heat capacity of water in a magnetic field

The coefficient that converts the measured radiation induced temperature change, ΔT_w, to the quantity of interest, D_w, is the specific heat capacity of water, c_p (4207.5 J kg^{-1} K^{-1} at 4 °C), obtained from literature at 0 T (IAPWS 2014). No substantial literature was found on c_p in magnetic fields or the effect of magnetic fields on c_p. With the MCE described above, equation (5.7) does not provide a value of c_p in a magnetic field. For this c_p needs to be measured in a magnetic field, which is outside the scope of this study. However, to obtain an indication of a change in heat capacity between 0 T and 1.5 T, a calorimeter temperature measurement was performed during magnet ramp-down. A significantly larger change in water temperature than expected by the MCE, would then indicate a change of c_p.

5.2.4.5. The chemical heat defect, h

Situations for which full conversion of energy deposition into temperature rise is not fulfilled are indicated by the heat defect, *h*. For photon beams in water calorimetry the chemical heat effect is described by various authors, e.g. Domen (1982), Klassen and Ross

(1997), Seuntjens and Palmans (1999) and Krauss and Kramer (2003) and summarized by Seuntjens and Duane (2009). The chemical heat defect in a water calorimeter is almost entirely caused by radiation-induced exo- or endothermic chemical reactions. VSL applies a sealed glass vessel (HPC) filled with pure (hypoxic) water system which is saturated with Ar-gas to remove any remaining impurities. The VSL HPC is made of glass with Teflon™ seals in contact with the water. It undergoes a thorough cleaning process before it is filled. The preparation process, filling and Ar-saturation of the HPC has shown to be effective and reliable: i.e. with a successful fill no pre-irradiation is needed to reach a steady state zero heat-defect with $h = 0$ within the stated uncertainty of 0.2 %. Linear Energy Transfer (LET) and dose-rate are known to influence the chemical heat defect. However, these properties of radiation do not fundamentally change for the MRI-linac used in this study compared to conventional linacs. It is unknown how the reaction constants for the chemical heat defect are affected. For the time being, it is assumed that also in the presence of a magnetic field, a zero-chemical heat defect is valid within the relative standard uncertainty of 0.2 %.

5.2.4.6. Correction for conductive heat flow, k_C

The correction for conductive heat flow, k_C, is applied to correct for relative excess temperature rise, R_{XS}, due to non-water materials (HPC and probes, i.e. mainly glass) and dose distribution in the calorimeter water phantom (Palmans 2000, Krauss 2006b, de Prez *et al* 2016a). The dose distribution caused by a photon beam entering a water phantom changes with magnetic field strength. Potentially, k_C is also affected by the magnetic field induced changes in material thermal properties such as specific heat capacity, c_p and heat conduction coefficient, k. However, this is not considered in the calculation of k_C. Seuntjens and Duane (2009) showed that the excess temperature effect, R_{XS}, is proportional to both c_p and k. Because $k_C = (1 + R_{XS})^{-1}$, any change in R_{XS} caused by a change in c_p or k has a second order effect on k_C. In the current literature no evidence could be found to indicate an effect on c_p or k caused by a magnetic field. k_C was determined with finite element simulation according to the heat transfer model described by de Prez *et al* (2016a). In this model only ¼ of the beam and calorimeter were modelled with symmetry on the XZ and YZ planes (see Figure 5-2). The model was based on conduction-only since the water density was maximal at 4 °C, avoiding density driven convection due to thermal gradients. The magnetic field dependence on the radiation induced excess heat of the HPC, was investigated by Monte Carlo calculations and shown to be smaller than 4 %, affecting the overall k_C by less than 0.05 %. Measured lateral and depth dose profiles were used as input for the heat transfer calculations. Since the applied model was based on a quarter geometry with symmetry on the XZ and YZ-planes, asymmetry of the MRI-linac beam profiles was accounted

for by simulating only a profile shift in X-direction. The excess temperature, R_{XS}, was then calculated at reference points shifted in the opposite direction. Asymmetry of the cross-line profile could not be simulated in a quarter geometry, however, the input cross-line profile for the heat transport calculations were based on the mean +X and -X profiles to average the thermal effect approaching the ΔT_w measurement point from both sides. It must be noted that k_C does not account for beam radial non-uniformity. This is dealt with in correction factor k_R, shown in equation (5.3), described in section 5.2.4.8.

5.2.4.7. Correction for perturbation of the glass cell, k_{HPC}

The perturbation correction for the presence of the high-purity water cell and probes, k_{HPC} was measured in the MRI-linac both with and without 1.5 T magnetic field. For this purpose, a small ion chamber (PTW 31013) was placed in a water phantom. The ion chamber signal was measured repeatedly while it was inside the HPC and in water without HPC.

5.2.4.8. Correction for geometrical deviations from reference conditions, k_R

The correction, k_R, corrects for the deviation of the measurement conditions according to the defined reference geometry such as source detector distance (k_{SDD}), depth in water (k_d) and beam radial non-uniformity (k_{nu}):

$$k_R = k_{SDD} \cdot k_d \cdot k_{nu}. \tag{5.14}$$

In this study the reference SDD was 139.3 cm and the reference depth 10 g cm^{-2}. k_{SDD} and k_d are determined by applying respectively the inverse square law and photon beam effective attenuation, μ_{eff}, based on measured TPR$_{20,10}$ values, described by e.g. Andreo *et al* (2017). The calorimeter correction for beam radial non-uniformity, k_{nu}, at the position of the probe tips, 5 mm off-axis, was based on the measured cross-line (X) and in-line (Y) dose profiles and determined by the measured ratio at beam centre and 5 mm off-axis.

5.2.5. Calorimeter measurements

Measurements in the MRI-linac were performed in a 1.5 T magnetic field and, after ramp-down, repeated without magnetic field. Both measurement series, i.e. with and without magnetic field, were performed with the same high-purity cell, HPC and thermistor probes (HPC serial number 06 with thermistor probes serial numbers 13T023 and 15T006). Additionally, with and without magnetic field, the directional dependence of the HPC and probes was assessed. This was done by performing measurements with the HPC in parallel direction to the bore (and magnetic field) and in perpendicular direction. Variation in D_w measurements in the VSL ^{60}Co source before and after the

measurements at UMCU were smaller than 0.05 %, confirming chemically stable HPC and thermistor calibration during the measurements at UMCU. Pre-drifts and post-drifts were 120 seconds with intermediate heating drifts of 60 seconds at ~560 cGy min^{-1}. The nominal source surface distance (SSD) was set at 129.3 cm at nominal depth of 10 g cm^{-2}, at the beam central axis. Deviations from nominal SDD and depth were measured according to the methods described earlier (de Prez *et al* 2016a) and corrected to nominal SSD and depth by applying k_R in equation (5.14). Within the two separate measurement series, i.e. with and without magnetic field, the readings were normalized to the transmission monitor inside the bore of the MRI-linac. These series cannot be directly compared since the response of transmission monitor was affected by the magnetic field.

5.3. Results and uncertainties

5.3.1. Magnetic field effects during HPC rotation

The HPC and probes were rotated in relation to the magnetic field to investigate the effect of the field direction on the calorimeter performance. Figure 5-3 shows the thermistor drift while rotating the HPC with thermistors from perpendicular ($\perp$) to parallel ($\parallel$) direction. The first 40 seconds after rotation were discarded because of electrical noise due to movement of signal cables. Figure 5-3 shows that the rotation of the HPC causes a change in temperature drift. Presumably, this can be explained by two independent effects, illustrated by the inset on the top-right corner of the figure. The first effect (yellow line, marked *probe*) is caused by the movement of the water inside the HPC and causes an immediate drop of thermistor self-heat. Within about half an hour the self-heat is re-established to its initial conditions. The second effect (blue line, marked *phantom*) is caused by movement of the calorimeter phantom water outside the HPC. It causes a drop of water temperature outside the HPC resulting in a gradual temperature decrease at the position of the probes. A drop in phantom temperature is caused by a disturbance of the steady-state vertical temperature gradient in the phantom with relatively warm water at the top and colder water at the bottom. During steady-state, this gradient is intensified by a small influx of heat through the radiation entrance window (Figure 5-1). The second effect leads to a slow background drift which usually takes days to re-establish the steady-state equilibrium. Within the time scale of the experiment, this effect can be approximated by a constant cooling drift. Both effects add up to the illustrated *measured* temperature drift (green line, marked *measured*). It is assumed that extrapolation of the linear part of the post-drift to time = 0 min coincides with the thermistor resistance just after rotation ($\parallel$). This results in resistance changes, $\Delta R_{MR,\perp}/R_{MR,\parallel}$ of +1.4 ppm and +2.9 ppm for respectively thermistors 13T023 and 15T006, which are smaller than the uncertainty of 4 ppm on the total thermistor MRE.
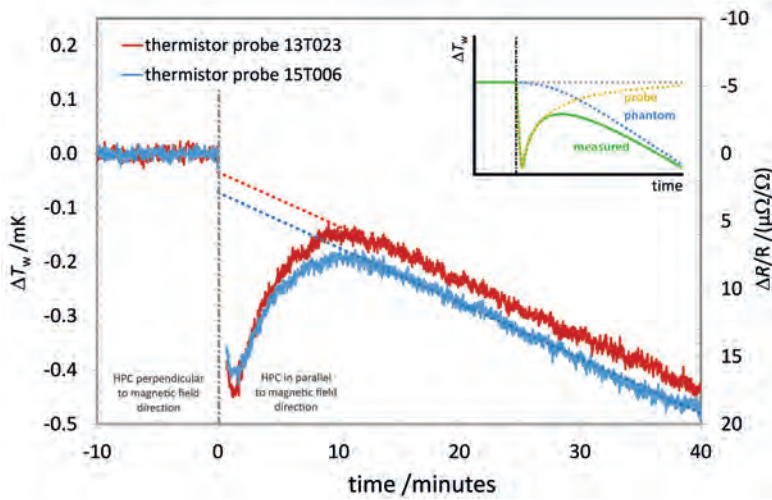
Figure 5-3. Calorimeter drift of two thermistors while rotating the HPC with thermistors from perpendicular to parallel direction in the magnetic field. The right-axis shows the actual relative resistance change, $\Delta R/R$, while the left-axis shows the equivalent in water temperature, ΔT_w, with a thermistor coefficient, α, of ~0.04 K^{-1}. The inset on the top-right corner illustrates the two presumed effects involved in a qualitative way: 'probe' cooling of the thermistor self-heat; 'phantom' movement of the phantom water.

An average value for the MRE of -38 ppm was obtained previously (de Prez *et al* 2016a) in a perpendicular orientation. Combining the values obtained in this study by correcting the probes MRE from ⊥ to ∥ leads to values for $\Delta R_{MR,\parallel}/R$ of respectively -36.6 ppm and -35.1 ppm for the current probes. The uncertainty on these values is estimated to remain 4 ppm.

5.3.2. Magnetic field effects during ramp-down

The top of Figure 5-4 shows the thermistor resistance change during magnet ramp-down from 1.5 T to 0 T with the probes in parallel direction to the magnetic field, $\Delta R_{MR\parallel}$. The drift was recorded from 3 hours prior to 3 hours after the start of the ramp down. The bottom of Figure 5-4 shows the thermistor temperature drifts before the start (time ≥ 0 h) and after completion (time ≤ 0.5 h) of the ramp-down.

The differences in temperatures between the two probes is smaller than 1.5 mK. This is within the uncertainty of the thermistors' temperature calibrations of 2 mK ($k = 2$). To obtain the temperature drifts, the thermistors resistances were corrected for the MRE determined previously. The difference in water temperature with and without magnetic field, T_w, is determined by extrapolation of the post-drift to the start of the ramp-down (time = 0 h).
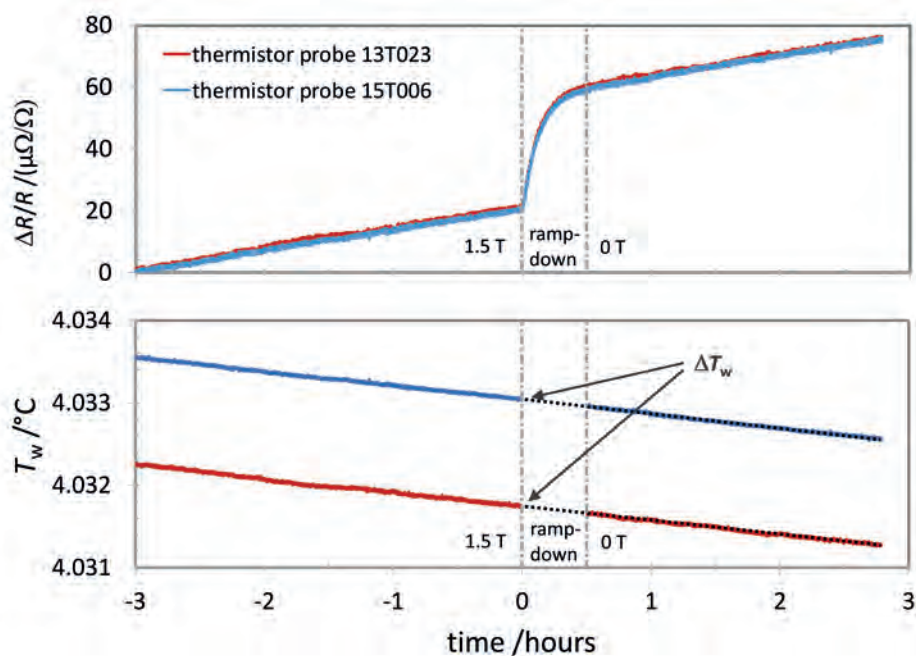
Figure 5-4. The thermistor resistance change, $\Delta R/R$ in ppm (top), and water temperature drift, T_w in °C (bottom), from 3 hours before until 3 hours after the start of the magnet ramp-down from 1.5 T to 0 T. The magnet ramp-down starts at time = 0 hours.

For thermistors 13T023 and 15T006 ΔT_w of respectively -0.16 mK and -0.13 mK was determined with an uncertainty of 0.20 mK ($k = 2$). The latter is based on an uncertainty of 4 ppm ($k = 1$) on the MRE and therefore ΔT_w does not deviate significantly from 0 K. The predicted temperature change due to adiabatic demagnetization, $\Delta T_{ad,MRE}$, of -0.06 μK, given by equation (5.13), is smaller than this uncertainty and therefore not detectable. Additionally, the bottom of Figure 5-4 shows no change in slope of the temperature drift before and after ramp-down. This suggests that there were no changes in thermal properties of water such as heat conduction coefficient, used for the conductive heat flow correction, k_C. The non-detectable temperature change combined with the constancy of temperature drift before and after ramp-down strongly suggests that there is no significant change in c_p between 0 T and 1.5 T. c_p is considered unchanged and no additional uncertainty was applied to c_p in a 1.5 T magnetic field.

5.3.3. Calorimeter correction factors

Table 5-1 shows the calculated correction factors for heat conduction, k_C, with and without magnetic field for both orientations of the calorimeter high-purity cell, HPC, perpendicular to the bore ($k_{C,\perp}$) and in parallel to the bore ($k_{C,\|}$). The standard deviation

in k_C for different orientations with and without magnetic field is 0.05 % and shows that differences are smaller than the assigned relative standard uncertainty for k_C calculation of 0.18 % (de Prez *et al* 2016a).

The correction for the lateral position of the thermistor probes, k_{nu}, in equation (5.14) accounts for the position of the thermistor probes, nominally 5 mm off-axis. It is based on the position of the calorimeter, based on EPID images in the linac beam and on measured lateral profiles obtained from (Woodings *et al* 2018) with an average dose shift of 2.4 mm in the X-direction, perpendicular to the bore. Because no internal markers were used for positioning of the calorimeter reference point, external structures were used. Therefore, and despite the 0.2 mm EPID resolution, the lateral positioning of the thermistors was estimated to be known within 1 mm. This corresponds to a Type B relative standard uncertainty of 0.05 % for the FFF beam of the MRI-linac, based on the dose gradients in the beam profiles. The radial non-uniformity correction at the position of the probes, corrected for lateral alignment of the calorimeter with the EPID images was between 1.0007 and 1.0025 with an average of 1.0014 and independent of magnetic field.

Table 5-1 also shows the measured corrections due to the perturbation and scatter of two high-purity glass cells (IDs #06 and #07) measured both with and without magnetic field. HPC #06 was used for the measurements described in this study. The measured values show that the respective correction factors with and without the presence of a magnetic field overlap within their assigned uncertainties. It can be concluded that the perturbation correction for the presence of the HPC is not affected by the magnetic field. Therefore, the assigned relative standard uncertainty is unchanged, i.e. 0.05 % ($k = 1$).

Overall it can be concluded that calorimeter correction factors, k_C, k_{nu} and k_{HPC} can be determined by calculations or measurement but are not significantly affected by the presence of the magnetic field.

Table 5-1: Calculated correction factors for heat conduction, k_C and measured correction factors for perturbation of the calorimeter HPC both with and without magnetic field.

correction	$B = 0$ T	$B = 1.5$ T
$k_{C,\perp}$	0.9976(18)	0.9979 (18)
$k_{C,\|\|}$	0.9970(18)	0.9969 (18)
$k_{nu,\perp}$	1.0013(5)	1.0015 (5)
$k_{nu,\|\|}$	1.0014(5)	1.0016 (5)
k_{HPC} (#06)	1.0033(5)	1.0025 (5)
k_{HPC} (#07)	1.0031(5)	1.0028 (5)

5.3.4. Calorimetry results parallel and perpendicular to the *B*-field

Calorimeter measurement parallel and perpendicular to the magnetic field are shown in Figure 5-5. The right graph of Figure 5-5 shows calorimetric D_w measurements in a 1.5 T magnetic field. Measurements were performed with the HPC in parallel and perpendicular direction to the magnetic field, resulting in average values for D_w normalized to the transmission monitor of respectively 0.6533 Gy MU^{-1} (n = 77) and 0.6544 Gy MU^{-1} (n = 60) both with a Type A standard uncertainty of 0.05 %. To compare the parallel and perpendicular values, the relative standard uncertainty was estimated to be 0.18 %. This includes a 0.05 % Type B uncertainty on k_{nu} for positioning in the MRI-linac FFF beam and 0.16 % for the day-to-day stability of the monitor ion chamber. The agreement between the values obtained with the two HPC orientations was 0.17 % and within the expanded uncertainty 0.36 % ($k = 2$).

The left graph of Figure 5-5 shows D_w measurements performed with the HPC in parallel and perpendicular direction to the bore, at 0 T. This resulted in average values for D_w normalized to the transmission monitor of respectively 0.6137 Gy MU^{-1} (n = 30) and 0.6120 Gy MU^{-1} (n = 29) with a type A standard uncertainty of respectively 0.18 % and 0.07 %. In the same way as with the 1.5 T measurements, the relative standard uncertainty on these values was estimated to be better than 0.09 % ($k = 1$). The agreement between the values obtained with the two HPC orientations was 0.28 %, also within the expanded uncertainty 0.36 % ($k = 2$).

For both measurements at 1.5 T and at 0 T the differences between parallel and perpendicular orientation are within the estimated expanded uncertainties.

5.4. Discussion and conclusion

5.4.1. Discussion

The aim of this study was to characterize and commission for the first time the Dutch national standard for kV and MV-photon beams as a primary standard for absorbed dose to water, D_w, in magnetic fields and evaluate its previously claimed uncertainty of 0.37 % ($k = 1$). Since a primary standard is defined as *a measurement standard obtaining a measurement result without relation to a measurement standard for a quantity of the same kind* (JCGM 2012), it cannot be compared to a more fundamental measurement standard. Agreement on an international level without magnetic field, e.g. organized by the BIPM (Allisy *et al* 2009), was shown by international comparisons (Picard *et al* 2017). However, due to the unique character of the VSL water calorimeter, comparison with equivalent standards in a magnetic field has not been possible. Therefore, a fundamental
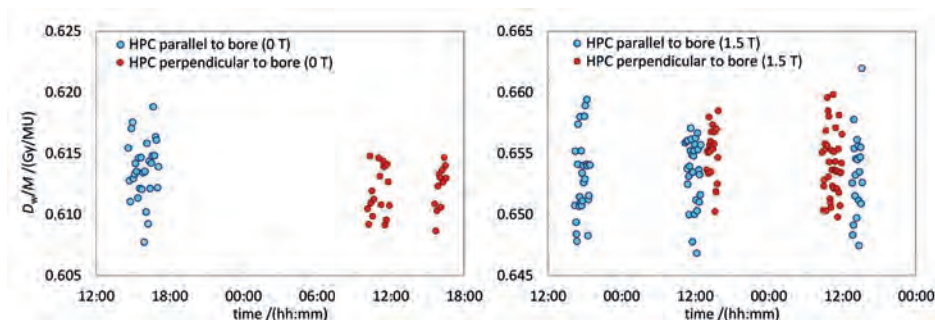
Figure 5-5. Corrected calorimetric D_w measurements in a 0 T magnetic field of an Elekta MRI-linac (left) and in the same machine with 1.5 T magnetic field (right). Both graphs show D_w measurements normalized to the transmission monitor in the bore with the HPC perpendicular and in parallel direction to the bore.

approach needed to be applied to commission the new primary standard in a magnetic field and evaluate its claimed uncertainty.

In the current study, the fundamental relation between radiation induced temperature change of the water, ΔT_w, and absorbed dose to water given by equation (5.3), was evaluated on a parameter by parameter basis. It was shown that the measurement of ΔT_w and most corrections, such as heat conduction, k_C, presence of non-water materials, k_{HPC}, and correction to reference geometry, k_R, in equation (5.3) are either independent of the magnetic field or can be determined in the presence of a magnetic field. It is known that chemical reaction constants, responsible for the potential chemical heat defect, could be affected by the magnetic field. For the chemical reactions responsible for the chemical heat defect in water calorimeters this data is lacking, therefore for the described water calorimeter, the chemical heat defect at 1.5 T is considered zero. LET and dose-rate are known to influence the chemical heat defect. However, these have not fundamentally changed for the MRI-linac used in this study. Therefore, it is assumed that also in the presence of a magnetic field, a zero-chemical heat defect is valid within the relative standard uncertainty of 0.2 %.

An indirect comparison of this study's D_w results with alanine dosimeters operated in an MRI-linac traceable to the NPL primary absorbed dose standard operated at 0 T showed excellent agreement of better than 0.3 % (Billas *et al* 2018). Here, the Degrees of Equivalence of NPL and VSL (see section 3.5) were taken into account (Allisy *et al* 2009). These results indicate that no significant effects in calorimetric D_w measurement were overlooked. However, they do not rule them out either including changes in the calorimeter heat defect for which future investigation is needed.

The potential temperature effect due to the magneto-caloric effect (MCE) $\Delta T_{w,ad,MCE}$ is expected to be -0.06 µK. Variation of magnetic field during calorimetric measurement might lead to erroneous results due to this effect.

The calorimeter temperature was recorded during the MRI magnet ramp-down. No change in water temperature was detected beyond the uncertainty of 0.20 mK. It is noted that a $\Delta T_{w,ad,MCE}$ of -0.06 µK would not have been detectable. As a change in c_p with magnetic field would lead to a sudden change in water temperature, it was concluded that it is adequate to apply the same c_p for 0 T and 1.5 T.

D_w measurements with the high-purity cell (HPC) were performed parallel to and perpendicular to a 1.5 T magnetic field as well as at 0 T. These measurements were normalized to the external transmission monitor positioned at the top of the bore. A previous experiment showed that an additional uncertainty of 0.16 % needed to be applied when normalizing the calorimetric D_w measurement to the applied monitor system in order to compare D_w measurements performed on one day to measurements on a different day. Furthermore, ratios between D_w measurement obtained in 0 T and 1.5 T with a rotated HPC were comparable and therefore the effect of HPC orientation in the magnetic field was considered insignificant. This confirms the validity of measured radiation induced temperature change, ΔT_w, and the calorimeter correction factors k_C and k_{HPC}, determined for both orientations.

This study confirms that the uncertainty contributions in determination of absorbed dose to water, D_w, with the VSL water calorimeter in a 1.5 T, compared to 0 T, are negligible. Therefore, the uncertainty for calorimetric absorbed dose measurements on-site in an MRI-linac is the same as reported earlier (de Prez *et al* 2016a, 2018b) where it was estimated to be 0.37 % ($k = 1$). However, due to the applied monitor system in the current study, an additional 0.16 % ($k = 1$) is included for day-to-day variations when measured D_w are normalized for MRI-linac output. This uncertainty needs to be applied when comparing results measured on different days and thus also when the calorimeter is used for ion chamber calibrations. Recent improvements in the linac internal monitor system would probably eliminate this uncertainty in future measurements.

The water calorimeter described in this study is currently the only primary standard available for measurement in a magnetic field. This study showed that no additional corrections are needed for operation in a magnetic field. Established methods applied at 0 T can be used in a magnetic field with additional care for geometric alignment. The calorimeter performance is therefore considered to be independent of magnetic field,

including orientation and direction of both field and radiation beam, with an uncertainty of 0.37 % ($k = 1$).

5.4.2. Conclusion

This study successfully characterized and commissioned a water calorimeter as a primary standard of absorbed dose to water with an uncertainty of 0.37 % ($k = 1$). All parameters in the determination of the absorbed dose to water were either independent on the magnetic field or can be determined in the presence of a magnetic field. Developments in radiotherapy continue rapidly and the radiotherapy community cannot be delayed until such traceability framework is established. The VSL calorimeter is currently the only primary standard that provides direct access to international traceability framework for absorbed dose to water in the presence of a magnetic field.

5

6

Direct measurement of ion chamber correction factors, k_Q and k_B, in a 7 MV MRI-linac

Abstract

The output of MRI-integrated photon therapy (MRgXT) devices is measured in terms of absorbed dose to water, D_{w}. Traditionally this is done with reference type ion chambers calibrated in a beam quality Q_0 without magnetic field. To correct the ion chamber response for the application in the magnetic field, a factor needs to be applied that corrects for both beam quality Q and the presence of the magnetic field B, $k_{Q,B}$. This can be expressed as the product of k_Q, without magnetic field, and ion chamber magnetic field correction, k_B. k_B depends on the magnetic field strength and its direction, the direction of the beam and the orientation and type of the ion chamber. In this study, for the first time, both k_Q and k_B were measured directly for 6 waterproof ion chambers (3 × PTW 30013 and 3 × IBA FC65-G) in a pre-clinical 7 MV MRI-linac at 0 T and at 1.5 T. Measurements were done with the only available primary standard built for this purpose, a water calorimeter. Resulting k_Q factors for PTW and IBA chambers were respectively 0.985(5) and 0.990(4). k_B factors were measured with the chambers in antiparallel direction to the magnetic field ($\parallel$ 180°), and perpendicular direction ($\perp$ -90°). $k_{B\parallel}$ and $k_{B\perp}$ for the PTW chambers were respectively 0.985(6) and 0.963(4) and for IBA chambers 0.995(4) and 0.956(4). Agreement with the available literature values was shown, partly caused by the relatively large standard deviation in those values. The values in this study are currently the only available measured values for k_Q and k_B in an MRI-linac that are directly linked to the international traceability framework for the quantity absorbed dose to water, D_{w}.

6.1. Introduction

MRI guided radiotherapy (MRgRT) uses an MRI scanner integrated with a treatment machine and allows for unprecedented real-time visualization and motion tracking of the target during the actual treatment, in real time. Several, integrated MRgRT devices are under development or in clinical use (Keall *et al* 2014, Fallone 2014, Mutic and Dempsey 2014, Raaymakers *et al* 2017). However, dosimetry in the presence of a magnetic field, B, is not trivial. The energy deposition of the secondary electrons trajectories is influenced by the Lorentz force and dose distributions change e.g. in build-up and penumbra regions, with depth and in regions with material and density inhomogeneities (Raaijmakers *et al* 2008, Raaymakers *et al* 2004, Woodings *et al* 2018, Oborn *et al* 2010). Traditionally, photon beams in radiotherapy are calibrated in terms of absorbed dose to water, D_w, by ion chambers calibrated in beam quality Q_0 (usually ^{60}Co), $N_{D,w,Q0}$, without magnetic field (Andreo *et al* 2000, McEwen *et al* 2014, Aalbers *et al* 2008). The most fundamental and direct method to calibrate detectors for reference dosimetry is against a *primary standard*[13] that realizes the unit gray (Gy) for D_w, at the reference point in a water phantom. The ion chamber calibration coefficients, $N_{D,w}$, is established by dividing D_w by the ion chamber reading, M, corrected for influence quantities (Andreo *et al* 2000, Almond *et al* 1999):

$$N_{D_w} = \frac{D_w}{M}. \tag{6.1}$$

Reference dosimetry in MRI-integrated photon therapy (MRgXT) devices is done with ion chambers that are placed in the magnetic field of an MRI-linac. Therefore, the change in ion chamber response needs to be corrected for both beam quality, Q, and magnetic field, B, by a factor $k_{Q,B}$. D_w is determined according to:

$$D_w = k_{Q,B} \cdot M \cdot N_{D_w Q_0}. \tag{6.2}$$

The correction factor $k_{Q,B}$ is, in analogy to k_Q (Andreo 1992), defined as the ratio between its calibration coefficients in beam quality Q with magnetic field, $N_{D,w,Q,B}$, and that in reference beam quality Q_0 without magnetic field, $N_{D,w,Q0}$:

$$k_{Q,B} = \frac{N_{D_w,Q,B}}{N_{D_w,Q_0}}. \tag{6.3}$$

---

13 *primary standard:* is defined as a measurement standard obtaining a measurement result without relation to a measurement standard for a quantity of the same kind (JCGM 2012)

Another approach is to apply the product of two independent correction factors, i.e. a beam quality correction for the MRI-linac photon beam without magnetic field, k_Q, and a magnetic field correction k_B:

$$k_{Q,B} = k_Q \cdot k_B = \frac{N_{D_w,Q}}{N_{D_w,Q_0}} \cdot \frac{N_{D_w,Q,B}}{N_{D_w,Q}}. \tag{6.4}$$

Monte Carlo calculations and measurements showed that the magnetic field affects k_B by several percent (Meijsing *et al* 2009, Reynolds *et al* 2013, Smit *et al* 2013). The amount depends on ion chamber design and construction, its orientation in the field and the direction and magnitude of the magnetic field in relation to the radiation beam. Recent studies reported k_B factors, determined either by Monte Carlo calculations (O'Brien *et al* 2016, Spindeldreier *et al* 2017, Malkov and Rogers 2018, Pojtinger *et al* 2018) or by measurement of ion chamber readings with and without magnetic field (van Asselen *et al* 2018). Most of these studies assumed that k_Q in equation (6.4) can be taken from existing Codes of Practise, CoPs (Andreo *et al* 2000, McEwen *et al* 2014, Aalbers *et al* 2008). However, as shown by Woodings *et al* (2018), in case of the Elekta Unity MRI-linac used in this study, the flattening filter free (FFF) beam characteristics are affected by the MRI-cryostat wall. Consequently, the applicability of the k_Q from existing CoPs for application in MRI-linacs was never confirmed. In addition, despite the recommendation to measure k_Q against primary standards (Andreo *et al* 2000), which presumably also holds for k_B, no experimental data for k_Q or k_B based on primary standards in MRI-linacs is available. In order to do this ion chambers need to be calibrated in beam quality Q_0 (^{60}Co) without magnetic field to obtain N_{D,w,Q_0}, and in MRI-linac beam quality Q both with and without magnetic field to obtain respectively $N_{D,w,Q,B}$ and $N_{D,w,Q}$ in equation (6.4).

VSL developed a new water calorimeter as a primary standard for absorbed dose to water in ^{60}Co, kV and MV-photon beams. It was designed to operate in a magnetic field of MRI-incorporated treatment devices (de Prez *et al* 2016a). The calorimeter demonstrated its capability for on-site measurements in conventional flattened (cFF) and flattening filter free (FFF) high-energy photon beams (de Prez *et al* 2018b). Its international agreement for measurement of D_w in beams without magnetic field (i.e. at 0 T) and its uncertainty was confirmed by BIPM[14] key comparisons (Picard *et al* 2017, Kessler *et al* 2018). A preliminary study showed its feasibility to measure absorbed dose to water, D_w, in a magnetic field and to calibrate ion chambers directly in the

---

14 The Bureau Internationales des Poids et Mesures, BIPM in Sévres, is an international organization established by the Metre Convention, through which Member States act together on matters related to measurement science and measurement standards (https://www.bipm.org/).

calorimeter phantom (de Prez *et al* 2016b). A more comprehensive study confirmed that the uncertainty for measurement of D_w with a water calorimeter in a 1.5 T magnetic field is estimated to be the same as under conventional reference conditions (de Prez *et al* 2019b). The VSL water calorimeter is currently the only primary standard operable in a magnetic field that provides a direct link to the international system of units (SI, *Système International*).

The aim of this study is to measure k_Q and k_B directly for 2 ion chamber types of each 3 serial numbers in a pre-clinical 7 MV Elekta Unity MRI-linac at 0 T and at 1.5 T. This is done by direct D_w calibrations against the VSL primary standard in ^{60}Co, without magnetic field, and in beam quality Q, with and without magnetic field. Some of the materials and methods applied here, were described in detail earlier (de Prez *et al* 2016a, 2018b, 2019b).

6.2. Materials and methods

6.2.1. The wide bore hybrid MRI-linac system
The pre-clinical Elekta Unity hybrid MRI-linac system comprised a modified 1.5 T Philips wide bore MRI with 70 cm diameter and an Elekta 7 MV standing wave linear accelerator producing a flattening filter free (FFF) photon beam with a pulse rate frequency (PRF) of 275 Hz (Raaymakers *et al* 2009, Lagendijk *et al* 2014b, Woodings *et al* 2018). A ring around the patient bore, allowed for rotation with the accelerator iso-centre at 143.5 cm. It provided for a transverse magnetic field relative to the direction of the MV-photon beam. The linac was equipped with an electronic portal imaging device (EPID), used for alignment of measurement equipment. The beam quality expressed in TPR$_{20,10}$ had a value of 0.701(2), independent of the presence of the magnetic field within its reported standard uncertainty (van Asselen *et al* 2018). All measurements in the current study were performed with a vertical beam, i.e. at gantry angle 0°.

6.2.2. The orientation dependence of $k_{Q,B}$
The effect on ion chamber responses due to the magnetic field, B, in beam quality Q, $k_{Q,B}$ in equation (6.4), is dependent on the orientation of the chamber and the direction of the magnetic field in relation to that of the beam. Hence, these conditions need to be specified to fully describe the relevant measurement conditions. It was shown previously that chamber orientations with the thimble facing in opposite direction (or the magnetic field sign changed) can result in a different chamber response. This is caused by a non-symmetric, chamber dependent dead-volume near the chamber guard electrode, i.e. at the stem-side (Butler *et al* 2015, Spindeldreier *et al* 2017, Malkov and Rogers 2017). It

Figure 6-1. Vertical beam (gantry 0°) beam's-eye-views of the relative orientations of an ion chamber, magnetic field and beam direction for (A) antiparallel ($\parallel$ 180°), and (B) perpendicular, ($\perp$ -90°, i.e. counter-clockwise), orientations.

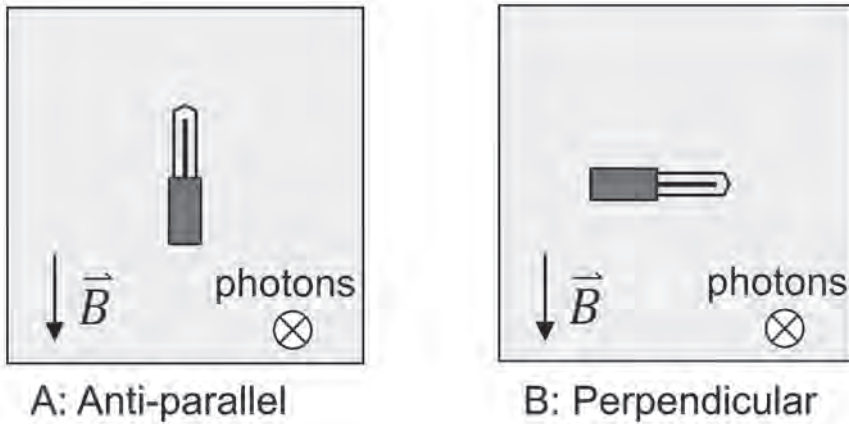is caused by the design of modern ion chambers. The orientations applied in this study are illustrated in Figure 6-1. Vertical beam (gantry 0°) beam's-eye-views of the relative orientations of an ion chamber, magnetic field and beam direction for (A) antiparallel ($\parallel$ 180°), and (B) perpendicular, ($\perp$ -90°, i.e. counter-clockwise), orientations.

6.2.3. Calorimetric determination of D_w

The D_w measurements are described elsewhere (de Prez *et al* 2019b). Measurements at 1.5 T took place on day, 1, 2, 3 and 19 of a 19-day period (6 measurement series). The MRI-linac magnet was ramped down on day 22 and calorimeter measurements were repeated at 0 T on day 23, 24, and 34 (3 measurement series). The measurements were performed in groups of approximately N = 30 consecutive calorimeter runs, taking about 5 min per run of which 1 min of irradiation. On three occasions, two with magnetic field and one without magnetic field, the orientation of the calorimeter high-purity water cell was changed from perpendicular to parallel as described previously (de Prez *et al* 2019b). Each time this was done on the same day. It was shown earlier that the calorimeter performance, both with and without magnetic field, was unaffected by the orientation of the vessel. Therefore, in this study, perpendicular and parallel measurements with magnetic field were combined for their contribution to D_w. The same was done for perpendicular and parallel measurement without magnetic field.

6.2.4. Ion chamber calibration

Ion chamber calibrations at 1.5 T were done in the period between day 4 and day 18 and at 0 T in the period between day 25 and day 33, both preceded and succeeded by

calorimeter D_w measurements. Prior to the ion chamber calibration, all chambers were imaged by CT and no irregularities in chamber construction were observed. The ion chamber signal, M, was integrated over 60 s, the same integration time as used for the calorimetric D_w measurements, described earlier (de Prez *et al* 2019b). This was done to avoid introduction of differences in beam on-off timing between calorimetry and ion chamber measurements. Furthermore, the ion chambers signal was measured in the same set-up as the D_w measurements, i.e. inside the calorimeter water phantom, however, with the water at room temperature. The corrected ion chamber reading, M, in equation (6.1) was determined by:

$$M = \left(M_{\mathrm{raw}} - M_{\mathrm{leakage}}\right) \cdot k_{\mathrm{elec}} \cdot k_{\mathrm{p,T}} \cdot k_{\mathrm{s}} \cdot k_{\mathrm{pol}} \cdot k_{\mathrm{R}}, \qquad (6.5)$$

where the leakage signal, M_{leakage}, in the electrometer readings, M_{raw}, was shown to be negligible (< 0.05 %). The reading was corrected for electrometer calibration, k_{elec}, air cavity density compared to reference air density, $k_{\mathrm{p,T}}$, incomplete charge collection due to recombination, k_{s} and chamber polarity, k_{pol}. Temperature was measured in water, close to the ion chamber thimble. The air pressure was measured in the linac room at the approximate ion chamber height. Deviation from geometrical reference conditions and to the dose at the central axis of the beam was corrected for by k_{R}:

$$k_{\mathrm{R}} = k_{\mathrm{SDD}} \cdot k_{\mathrm{d}} \cdot k_{\mathrm{v}}, \qquad (6.6)$$

which contains corrections to reference source detector distance, k_{SDD}, specific depth (in g cm^{-2}) in water, k_{d}, and correction for volume averaging over the length of the ion chamber, k_{v}.

The ion chamber collecting potential, supplied to the central electrode by the electrometer (Keithley 6517B), was set to -300 V. In the MRI-linac, the ion recombination correction, k_{s}, was measured by applying the method described by Weinhous and Meli (1984) as recommended by commonly used Codes of Practice (Andreo *et al* 2000) with a collecting potential of -100 V directly following a measurement with a collection potential of -300 V. This method was shown to be independent of magnetic field (Smit *et al* 2013). In the beam quality Q_0, ^{60}Co, the ion recombination was measured by applying the method described by Boutillon (1998) for continuous beams. For all beams, the polarity correction, k_{pol}, was applied according to the methods described by e.g. Andreo *et al* (2000), performing measurements at +300 V collecting potential.

No additional correction was applied for the air attenuation between the monitor ion chamber and the calorimeter, since the variation of the correction with varying ambient

conditions was small. No correction was applied for air relative humidity since all measurements took place at a relative humidity between 25 % and 60 % for which no correction is needed (ICRU 1979, McEwen and Taank 2017). Source detector distance (SDD) of the instruments, i.e. ion chambers and calorimeter, was within 0.2 cm from the nominal SDD of 139.3 cm, 4.2 cm above iso-centre. The depth of the instruments was within 0.06 g cm^{-2} from the nominal value of 10 g cm^{-2}. SDD and depth were corrected to the nominal values by inverse square law and effective attenuation, μ (0.036 cm^2 g^{-1} based on a TPR$_{20,10}$ of 0.70), as described by e.g. Andreo *et al* (2017), respectively k_{SDD} and k_d in equation (6.6). The field size of the beam was set to 10 × 10 cm^2 at the iso-centre, corresponding to 9.7 × 9.7 cm^2 at the measurement position. The correction to the central axis-profile was applied by the ion chamber volume averaging correction, k_v. by a simple integration of the lateral beam profile over the length of the ion chamber cavity and normalization to central axis dose as described by (Palmans *et al* 2017). In this study k_v was applied separately and not included in k_Q because the available k_Q literature value to compare to was also determined without inclusion of k_v (Malkov and Rogers 2018).

The ion chambers were calibrated in both antiparallel (∥ 180°) and perpendicular (⊥ -90°) direction in a 1.5 T magnetic field, illustrated in Figure 6-1. After ramp down, the calibrations were repeated at 0 T.

6.2.5. Ion chamber positioning

The ion chambers were positioned inside the calorimeter phantom by methods described elsewhere (de Prez *et al* 2016a). To prevent variations in reading due to air around the ion chamber waterproofing sleeves (Hackett *et al* 2016), all measurements were performed in water using the waterproof ion chambers. The black line on the stem of the ion chambers were facing the radiation source. After measurement in perpendicular orientation (Figure 6-1(B), ⊥ -90°), the ion chambers orientations were remotely rotated 90° around the beam-axis to antiparallel orientation (Figure 6-1(A), ∥ 180°) without the need to access the water phantom. The difference between source detector distance in both orientations was negligible (< 0.05 mm). The difference in ion chamber SDD, compared to calorimeter SDD, was measured with an uncertainty of 0.3 mm (k = 1), equivalent to a relative standard uncertainty of 0.05 % on the determination of k_{SDD} in equation (6.6). This was slightly larger than in conventional linacs where it was considered to be 0.02 % (de Prez *et al* 2016a). The uncertainties in the depth and volume averaging correction, k_d and k_v was the same as reported earlier (de Prez *et al* 2016a, 2018b), respectively 0.04 % and 0.05 % (k = 1).

6.2.6. Beam output monitoring

The D_w and ion chambers measurements performed in this study took place over a period of several weeks. Therefore, an independent beam output monitor was used to normalize the measurement of D_w and M for determination of $N_{D,w,Q0}$ and, after ramp-down $N_{D,w,Q}$ in equation (6.4). The monitor system was described in detail earlier (de Prez *et al* 2019b), where an additional standard uncertainty of 0.16 % was applied for the monitor day-to-day variations.

6.2.7. Consistency check by independent posterior cross-calibration

The ion chamber measurements in the calorimeter water phantom are potentially sensitive to errors that can be made due to e.g. unnoticed geometrical misalignment, displacement of the transmission monitor, air-bubbles around the chamber or other unwanted effects. To validate ion chamber measurement in the calorimeter, an independent consistency check was done by cross-calibrating the ion chambers in an independent experiment. This was done after the calorimeter set-up was removed from the bore and the patient couch was re-installed. Each ion chamber was cross-calibrated against the other five. The cross-calibration was performed in such a way that most of the correction factors from equation (6.5) and (6.6) cancelled. The cross-calibrations were performed at 0 T and, after magnet ramp-up, at 1.5 T in the orientations shown in Figure 6-1, i.e. antiparallel (∥ 180°) and perpendicular (⊥ -90°). Measurements were performed in a modified MRI-compatible PTW MP1 water phantom, placed on the patient couch. The chambers were positioned at the iso-centre (143.5 cm), at a nominal depth of 10 cm. The black line on the stem of the ion chamber was facing the radiation source. At the same depth, approximately 2 cm off-centre, a waterproof IBA CC13 ion chamber was used as an independent monitor chamber. The ion chambers were connected to PTW Unidos E electrometers. All ion chamber readings were recorded in the same set-up. For each ion chamber, j, the calibration coefficient, $N_{D_w}^{\mathrm{cross,j}}$, was determined according to:

$$N_{D_w}^{\mathrm{cross,j}} = \frac{1}{5} \cdot \frac{\sum_{i \neq j}\left(N_{D_w}^{\mathrm{wcm,i}} \cdot M_i \cdot k_{s,i} \cdot k_{\mathrm{pol,i}}\right)}{M_j \cdot k_{s,j} \cdot k_{\mathrm{pol,j}}}. \tag{6.7}$$

The average of absorbed dose, D_w, based on measurement with the other 5 chambers (i ≠ j) was based on their calibration coefficients measured in the water calorimeter, $N_{D_w}^{\mathrm{wcm,i}}$, and represented by one fifth of the value of the numerator of the right-hand side of equation (6.7). Leakage signal, M_{leakage}, in the electrometer readings, M_{raw}, according to equation (6.5) was shown to be negligible (< 0.05 %). Corrections for polarity, k_{pol}, and recombination, k_s, were applied according to the methods described earlier. The corrections for $k_{p,T}$ in equation (6.5) and k_{SDD} and k_d in equation (6.6) were not considered

relevant because the monitor ion chamber was in a fixed geometry and therefore affected in the same way by variations in temperature, pressure, SDD and depth. Additionally, ion chamber volume averaging effect, k_v in equation (6.6) was shown to be the same for all chambers and therefore not applied. Despite the different SDD and thus a slightly different beam size at the position of the ion chamber than used during the measurements in the calorimeter phantom, differences in ion chamber stem corrections between the two chamber types were considered negligible. Corrections for electrometer calibration, k_{elec}, were not applied since all ion chambers were measured with the same electrometer, at the same range and with the same collection potential (-250 V) applied. All ion chambers measurements at either 0 T and 1.5 T were performed on the same day.

Due to the nature of this experimental set-up measured ratios of ion chamber readings at either 0 T or 1.5 T were potentially more reliable than those in the calorimeter phantom. Therefore, erroneous results of a single chamber measurement in the calorimeter dataset could be detected as an outlier using this method. Note that direct transfer of the calorimetric D_w was not possible because different monitor ion chambers were used in both the calorimeter and the cross-calibration set-up. Note that equation (6.7) could have been expressed as ratios of chamber readings. However, it was chosen to express the values in terms of calibration coefficients because k_B values are based on a ratio of calibration coefficients according to equation (6.3).

6.3. Results and uncertainties

6.3.1. Calorimeter D_w measurements

Calorimetric determination of D_w are shown in Table 6-1 and Figure 6-2. For each group of ~30 runs the mean and the standard deviation, SD was determined. The standard deviation of the mean, SDOM, was calculated for the groups based on the square root of N. It was shown to be less than 0.1 % and independent of the magnetic field. Additionally, the mean of the respective 6 and 3 groups was determined and the related SD of the group of these means was calculated, referred to as the *actual standard deviation of the means* or *actual SDOM*. The *actual SDOM* was respectively 0.26 % and 0.08 % for the 6 groups of D_w measurements with magnetic field and 3 groups of D_w measurements without magnetic field. If no additional day-to-day variation would be present, the SDOM should be the same as the *actual SDOM*. This is the case for the measurements without magnetic field. However, with magnetic field, the *actual SDOM* is larger than the SDOM, indicating an additional day-to-day variation in the D_w measurements. This effect was also found in a previous study (de Prez *et al* 2019b), where the day-to-day variation was presumably caused by the transmission monitor set-up in the

MRI-linac with magnetic field and amounted to 0.16 % for measurements over a period of 4 days (de Prez *et al* 2019b). In the current study, the calorimeter measurements with magnetic field took place at the start and end of a 19-day period. The D_w measurements, performed over the first days at the beginning of the respective periods were shown to be closer together than the final D_w measurements. This indicates the presence of a long-term (> 10 day) day-to-day variation, larger than 0.16 %, previously determined over a period of 4 days. To account for this in the current study, the measured *actual SDOM* is applied as the Type A uncertainty contribution, i.e. determined by repeated measurement, to the D_w for determination of the ion chamber magnetic field correction factor, k_B. No additional day-to-day variation on the ion chamber measurements was applied, because this was accounted for by the variation in calorimetric D_w measurements. The dose-rate at the calorimeter reference conditions before and after ramp-down was approximately 9.4 cGy s^{-1}, which relates at a 275 Hz PRF to a water absorbed dose per pulse of approximately 0.34 mGy pulse^{-1}.

Table 6-1: Summary of D_w measurements at 1.5 T and at 0 T, normalized to the applied transmission monitor, D_w/MU in cGy μC^{-1}, during the 30-day measurement period in the MRI-linac.

normalized D_w at 1.5 T					normalized D_w at 0 T				
day	N	D_w/MU	SD	SDOM	day	N	D_w/MU	SD	SDOM
		/cGy μC^{-1}	/%	/%			/cGy μC^{-1}	/%	/%
#1 ‖	28	65.31	0.49	0.09	#23 ‖	30	61.48	0.40	0.07
#2 ‖	29	65.36	0.42	0.08	#24 ⊥	29	61.49	0.32	0.06
#2 ⊥	22	65.50	0.32	0.07	#34 ‖	30	61.40	0.33	0.06
#3 ⊥	38	65.41	0.41	0.07					
#3 ‖	20	65.33	0.53	0.12					
#19 ‖	30	65.00	0.47	0.09					
group		65.32	0.26*		group		61.46	0.08**	

*average and SD of 6 measurement series, performed on days #1, #2, #3 and #19 at 0 T
**average and SD of 3 measurement series at 1.5 T, performed on days #23, #24 and #34
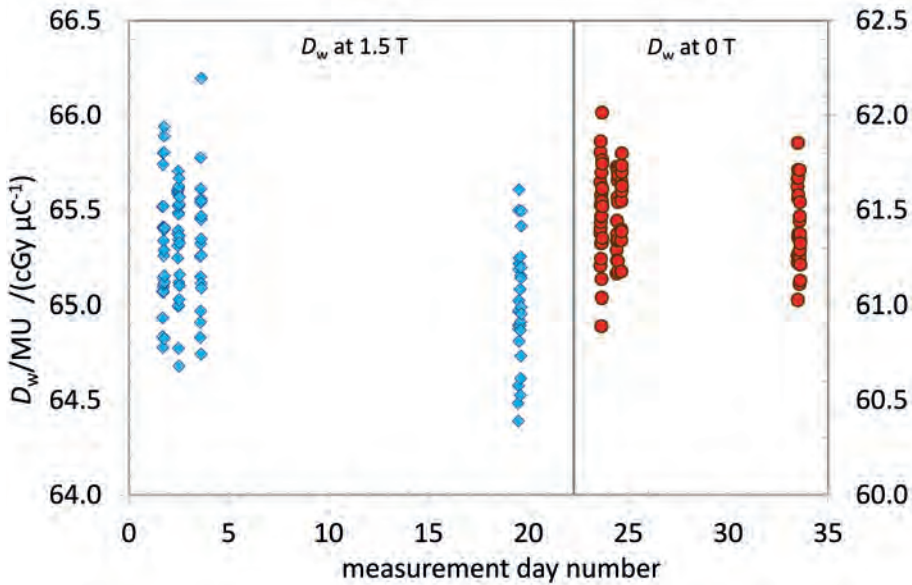
Figure 6-2. D_w measurements, normalized to the applied transmission monitor, D_w/MU in cGy μCy^{-1}, before and after MRI-linac ramp-down.

6.3.2. Ion chamber measurements

The ion chamber correction factors from equation (6.5), except for k_{elec}, $k_{p,T}$ and k_R, are given in Table 6-2. For all Farmer type chambers applied in this study with the same nominal cavity length of 2.3 cm, the volume averaging correction, k_v, from equation (6.6) was 1.0022(5) with magnetic field and 1.0023(5) without magnetic field. These values were in agreement with a volume averaging correction of 1.0021 calculated with a generic equation for FFF beams given by Palmans *et al* (2017). Despite a slight difference in beam profile between the lateral X and Y directions, k_v, was not significantly different between the two chamber orientations. In the current study, the corrections k_{SDD} and k_d were always smaller than 0.27 % and usually smaller than 0.10 %. Uncertainties for the contributions to k_R in equation (6.6) are presented elsewhere (de Prez *et al* 2016a, 2018b). Measurement of k_s and k_{pol} in the MRI-linac were done immediately following the ion chamber calibrations. The average values per chamber type are given in Table 6-2. With and without magnetic field, all measurements were done in perpendicular (⊥ -90°) and antiparallel (∥ 180°) direction to the bore. The measurements with the ion chambers in different orientations with magnetic field are reported separately in Table 6-2. However, corresponding measurements without magnetic field were combined because no significant differences were seen between the chamber orientations.

Table 6-2. Ion chamber correction factors for recombination, k_s, and polarity, k_{pol}, in the MRI-linac. Differences in k_s and k_{pol} in different orientations were smaller than 0.05 %.

chamber	beam	B-field	k_s	k_{pol}
PTW 30013	X7	1.5 T	1.0053(5)	1.0000(4)
		0 T	1.0047(1)	1.0002(3)
	^{60}Co	0 T	1.0010(2)	1.0002(3)
IBA FC65-G	X7	1.5 T	1.0060(4)	0.9989(4)
		0 T	1.0054(1)	0.9991(2)
	^{60}Co	0 T	1.0007(2)	0.9991(1)

6.3.3. Uncertainties in ion chamber k_Q and k_B factors

The uncertainty budget for D_w measurements with and without magnetic field was presented earlier (de Prez *et al* 2016a). It was shown that measurement of D_w with a water calorimeter and its related uncertainties are independent of the magnetic field, except for the larger Type A uncertainty in the repeated D_w/MU measurements, caused by the monitor set-up in the magnetic field. Therefore, the Type A uncertainty of 0.20 % for repeated $\Delta R/R$ measurements in Table 6-3 of de Prez *et al* (2016a), was replaced by the Type A uncertainties of the current study, respectively 0.26 % and 0.08 %. Furthermore, the uncertainty in correction to reference source detector distance k_{SDD} was adjusted from 0.02 % to 0.05 % caused by the alignment of the calorimeter in the MRI-linac bore. For the current study, this led to relative standard uncertainties in D_w for measurements at 1.5 T and at 0 T of respectively 0.53 % and 0.38 % ($k = 1$). The uncertainty in k_B and k_Q in this study was established in the same way as described earlier, taking correlation between the dose measurements in the denominator and nominator of equation (6.3) into account (de Prez *et al* 2016a, 2018b). The calorimetric contributions to the uncertainties in k_B and k_Q are shown in the first row of Table 6-3. The *actual SDOM* of calorimeter measurements, shown in Table 6-1, is applied as the Type A uncertainty on determination of D_w. The uncertainty for the ion chamber beam quality corrections at 0 T, k_Q, is determined as the quadratic sum of the contributions reported in Table 6-3 under ^{60}Co and Q. The uncertainty for the ion chamber magnetic field corrections at 1.5 T, k_B is determined as the quadratic sum reported in the table under Q and B at 1.5 T. The differences in uncertainty contributions to the SDD in ^{60}Co and in the MRI-linac were accounted for in k_Q because of the measurement in different facilities and therefor correlations don't apply. This means that 0.02 % and 0.05 % is accounted for in k_Q while only 0.05 % is accounted for in k_B. No distinction is made between the uncertainties in k_B factors for chambers placed in either antiparallel or perpendicular orientation to magnetic field. The uncertainty in $k_{Q,B}$ is determined in a similar way to be 0.39 %, but not shown in Table 6-3. No uncertainty contribution was applied for the response change

as a result of chamber misalignment with respect to its angle, which was expected to be smaller than 0.05 % based on a potential misalignment smaller than 0.5° (Smit *et al* 2013).

Table 6-3. Uncertainty budget for k_Q and k_B factors in this study. All uncertainties are of Type B, except for the repeated chamber measurements, M/MU.

source of uncertainty	measurement:	k_Q		k_B	
		^{60}Co: 0 T	Q: 0 T	Q: 0 T	Q: 1.5 T
D_w/MU, contribution to k_B and k_Q measurements		0.20	0.08	0.08	0.26
charge measurement per monitor unit (M/MU), Type A		0.10		0.10	
corrections for saturation and polarity, k_s and $_{kpol}$		0.07		0.07	
correction for p, T, $k_{p,T}$ and relative humidity		0.15		0.15	
correction to reference SDD, k_{SDD}		0.02	0.05	0.05	
correction to reference depth in water, k_d		0.04		0.04	
relative combined standard uncertainty ($k = 1$)		0.30		0.34	

6.3.4. Ion chamber consistency checks

Table 6-4 shows the ion chamber calibration coefficients, $N_{D,w}$, of the 6 ion chambers based on direct calibration with the water calorimeter. The table also shows the results of the additional cross-calibration, performed after removal of the calorimeter equipment from the MRI-linac bore. These results are expressed as relative deviations compared to the direct calibration coefficients, $\Delta N_{D,w,Q}$, where each chamber was cross-calibrated against the other five ion chambers. Per chamber type, field strength and chamber orientation, the standard deviation (SD) of the respective $\Delta N_{D,w,Q}$ for the three corresponding calibration coefficients is reported. Table 6-4 shows that for individual chambers, deviations are mostly smaller than 0.10 % and for some chambers about 0.25 %. However, for chamber PTW 30013 with serial number 008474, deviations with magnetic field antiparallel and perpendicular are respectively +0.50 % and -0.44 % which influences respectively the $k_{B\parallel}$ and $k_{B\perp}$ by the same amount. For the measurements without magnetic field, standard deviations of the differences are smaller than 0.10 %. Standard deviations for measurements with magnetic field are larger and range between 0.10 % and 0.35 %. Similar to the D_w/MU measurements, standard deviations without magnetic field are smaller than with magnetic field. Pojtinger *et al* (2018) also observed larger day-to-day variation for their experiments with Farmer type ion chambers in a magnetic field for which the reason remained unresolved. However, based on the standard deviations given in Table 6-4, it can be concluded that the individual ion chamber measurements show an adequate consistency as a basis for the generic k_Q and k_B data per chamber type, reported in Table 6-5. Therefore, no direct calorimeter calibrations were rejected.

Table 6-4. Direct calibration coefficients for the 6 ion chambers measured without magnetic field, $N_{D,w,Q}$, and with magnetic field in antiparallel and perpendicular orientation, respectively $N_{D,w,Q,B||}$ and $N_{D,w,Q,B\perp}$. The results of the cross-calibration are expressed as the relative deviations compared to the direct calibrations in the water calorimeter, $\Delta N_{D,w,Q}$. The cross-calibration coefficients were based on the same calorimeter D_w values as the direct calibration coefficients.

chamber	sn	$N_{D,w,Q}$ /(mGy pC^{-1})	$\Delta N_{D,w,Q}$ /%	$N_{D,w,Q,B||}$ /(mGy pC^{-1})	$\Delta N_{D,w,Q,B||}$ /%	$N_{D,w,Q,B\perp}$ /(mGy pC^{-1})	$\Delta N_{D,w,Q,B\perp}$ /%
PTW 30013	007120	52.53	+0.07	52.04	−0.15	50.65	+0.24
	008377	52.74	−0.03	51.81	−0.01	50.66	+0.04
	008474	52.52	+0.02	51.54	+0.50	50.68	−0.44
	SD		0.05		0.34		0.35
IBA FC65-G	3129	47.50	−0.08	47.20	+0.02	45.29	+0.16
	3212	47.52	+0.03	47.38	−0.25	45.52	−0.04
	3213	47.40	+0.05	47.19	−0.11	45.29	+0.06
	SD		0.07		0.14		0.10

6.3.5. Ion chamber k_Q and k_B factors

Ion chamber k_Q and k_B values and their uncertainties are given in Table 6-5. Ion chamber calibrations were based on the calorimetric D_w measurements with the high-purity cell in antiparallel as well as perpendicular direction to the bore, both with and without magnetic field. The ^{60}Co measurements at 0 T, before and after the measurements at the MRI-linac, were performed in a similar way as described earlier (de Prez *et al* 2016a). k_B values were entirely based on the measurements done at 1.5 T, before magnet ramp-down and at 0 T, just after magnet ramp-down. Therefore, the reported k_B is independent on the ^{60}Co measurements. Variation of D_w in ^{60}Co, used for determination of k_Q, before and afterwards was smaller than 0.05 %, confirming a chemically stable HPC and thermistor calibration during the measurements in the MRI-linac. The uncertainties on the generic k_Q and k_B values are established by adding the uncertainties reported in Table 6-3 to the relative standard deviation, SD, reported in Table 6-5. $k_{Q,B}$ factor can be obtained by multiplication of k_Q and k_B according to equation (6.4).

Based on the cross-calibration dataset, presented in Table 6-4, ratios between chamber calibration coefficients and thus between chamber k_Q and k_B values were verified in the same way. Consistency of generic k_Q and k_B values were shown to be always smaller than 0.11 % with standard deviations smaller than 0.14 %.

Table 6-5. This study's ion chamber k_Q and k_B factors for with magnetic field in antiparallel ($||$ 180°) orientation and perpendicular ($\perp$ -90°), orientation. $k_{Q,B}$ factors can be obtained by multiplication of k_Q and k_B.

chamber	sn	k_Q	k_B	
			$||$	$\perp$
PTW 30013	007120	0.985	0.991	0.964
	008377	0.988	0.982	0.961
	008474	0.982	0.982	0.965
	SD /%	0.3	0.5	0.2
	generic	0.985(5)	0.985(6)	0.963(4)
IBA FC65-G	3129	0.990	0.994	0.953
	3212	0.993	0.997	0.958
	3213	0.987	0.996	0.956
	SD /%	0.3	0.2	0.2
	generic	0.990(5)	0.995(4)	0.956(4)

6.4. Discussion and conclusion

6.4.1. Measurement of k_Q and k_B

k_Q and k_B values for ion chambers, reported in Table 6-5 , were measured with uncertainties of respectively 0.30 % and 0.34 %, given in Table 6-3. The major contribution to these uncertainties were of Type A, obtained from repeated calorimeter measurements, D_w/MU, in ^{60}Co and in the MRI-linac with magnetic field. The Type A uncertainty in the calorimeter measurements with magnetic fields (0.26 %) was higher than that without magnetic field (0.08 %). This was presumably caused by day-to-day variations in normalization due to the transmission monitor set-up inside the magnetic field of the MRI-linac (de Prez *et al* 2019b). To reduce this uncertainty contribution for future measurement the independent monitor set-up needs to be improved. Other uncertainty contributions in the MRI-linac determination of k_Q, are the same as in conventional linac beams, except for the uncertainty in correction to reference source detector distance k_{SDD}. This was adjusted from 0.02 % to 0.05 % due to the alignment of the calorimeter in the MRI-linac bore. Ion chamber corrections for volume averaging, k_v were smaller than previously measured in conventional flattening filter free beams and larger than those in beams with flattening filter (de Prez *et al* 2018b). This was mainly caused by beam flattening due to an increased SDD in the MRI-linac (139.3 cm) compared to the SDD in conventional linacs as given by Palmans *et al* (2017). Corrections for recombination and polarity, presented in Table 6-2, confirm that, for the applied ion

chambers, the polarity correction is both independent on beam modality and magnetic field within the reported uncertainty. k_s in a continuous beam of ^{60}Co is very small (< 0.1 %) as expected and mainly caused by initial recombination (Boutillon 1998). A consistency check by independent cross-calibration of each ion chamber against the other five, showed adequate consistency as a basis for the generic k_Q and k_B data per chamber type as reported in Table 6-5. However, also here also here the measurements with magnetic field showed a larger standard deviation than without magnetic field.

6.4.2. Comparison of k_Q and k_B with current literature

k_Q factors were determined independent of chamber orientation. k_B factors were determined in two orientations, antiparallel (∥ -180°) and perpendicular (⊥ –90°) to the transverse magnetic field. Table 6-6 gives currently reported literature values. All currently available values were reported with their Type A uncertainties only. The values summarized in Table 6-6 represent the unweighted means, which assumes that the overall uncertainties of the reported values (i.e. Type A plus Type B uncertainties) are very close to each other. Differences between beam profiles with and without magnetic field are not considered to affect k_B factors. The study by Malkov and Rogers (2018) is the only study that also reports Monte Carlo calculated k_Q values for the same ion chambers and MRI-linac as applied in the current study at 0 T. The other studies assume that k_Q values for the MRI-linac can be taken from existing CoPs, which is not trivial because the MRI-linac FFF beam is affected by the MRI-cryostat (Woodings *et al* 2018). Differences in ion chamber volume averaging, k_v, must be considered when comparing k_Q values. In the current study, k_Q values in Table 6-6 were corrected for chamber volume averaging effect. Table 6-6 gives the differences between the mean of the earlier reported values in literature and the values obtained in the current study. Differences for k_B range from -0.4 % to +0.8 %. Differences in k_Q based only one study (Malkov and Rogers 2018) are smaller than 0.2 %. All results are well within the expanded uncertainties ($k = 2$) of their differences. The largest difference from literature of 0.8 % is observed for the $k_{B⊥}$ of the PTW 30013 type. However, this value is consistent with the performed cross-calibration against the other five ion chambers and there is no reason to reject this value. In general, it can be concluded that the values presented in Table 6-5 are currently the best estimates provided with a comprehensive uncertainty budget for k_Q and k_B, both ∥ 180° and ⊥ -90°, in the Elekta Unity 7 MV MRI-linac.

The only studies basing their results on measurements are the current study and the study by van Asselen *et al* (2018). It is known that the chamber sensitive volume described by Butler *et al* (2015) plays a significant role in k_B and subsequently the orientation of the chamber (Malkov and Rogers 2017, Spindeldreier *et al* 2017). This must be accounted for correctly when calculating k_B by Monte Carlo methods. The reported Monte Carlo

studies only accounted for this in a quantitative way, i.e. based on matching Monte Carlo calculations with experiments. However, since the exact ion chamber dead-volume is currently unknown and is dependent of chamber guard construction, thus chamber type, this introduces an increased Type B uncertainty in the calculations. This is not covered by the reported uncertainties of the current Monte Carlo studies.

Table 6-6. This study's ion chamber k_Q and k_B factors compared to available literature values. Note that the Monte Carlo (MC) studies included the ion chamber sensitive volume, indicated with SV (Butler *et al* 2015, Malkov and Rogers 2017, Spindeldreier *et al* 2017) in the calculation of k_B, which is intrinsically incorporated in the measured k_B values.

chamber	study	method	k_Q	$k_{B||}$	$k_{B\perp}$
PTW 30013	van Asselen *et al* 2018	measured	–	0.992(2)	0.963(2)
	Malkov and Rogers 2018	MC – SV	0.984(1)	0.988(1)	–
	Pojtinger *et al* 2018	MC	–	0.996(2)	–*
	Spindeldreier *et al* 2017	MC – SV	–	0.993(3)	0.954(3)
	O'Brien *et al* 2016	MC	–	0.994(1)	0.976(1)
	mean (SD)		–	0.993(3)	0.964(11)
	difference from this study		−0.1(5) %	+0.8(7) %	+0.1(12) %
IBA FC65–G	van Asselen *et al* 2018	measured	–	0.997(3)	0.952(2)
	Malkov and Rogers 2018	MC – SV	0.988(1)	0.992(1)	–*
	mean (SD)		–	0.995(4)	0.952(2)
	difference from this study		−0.2(5) %	−0.1(6) %	−0.4(5) %

*These studies reported values in perpendicular direction to the magnetic field, however with the chamber in opposite orientation to the other studies reported in the table. It was shown in the reported studies that 'perpendicular' and 'anti-perpendicular' value for k_B could give different results. Therefore, these values are not reported here.

6.4.3. Conclusion

This study reports, for the first time, measured k_Q factors at 0 T and k_B factors at 1.5 T in a 7 MV-photon beam of a pre-clinical Elekta Unity MRI-linac. The measurements were based on direct calibrations, traceable to the Dutch primary standard for absorbed dose to water, operated on-site in the bore of the MRgXT device. Despite variations in measurements with magnetic field, the values presented are currently the best estimated provided with a comprehensive uncertainty budget for generic k_Q and k_B, both antiparallel (‖ 180°) and perpendicular (⊥ -90°), for PTW 30013 and IBA FC65-G chambers in the Elekta Unity MRI-linac. Partly because of the relatively large standard deviation of the available literature values (up to 1 %), agreement was shown with the values presented in the current study.

7

General summary

Accuracy in the delivery of radiotherapy treatment dose to the patient is of vital importance for individual patient treatment and for clinical trials on which patient treatment decisions are based. With respect to the physical aspects for accuracy in external beam radiotherapy, the accurate delivery of absorbed dose starts with reference dosimetry by the medical physics team in the clinical treatment beam.

The aim of reference dosimetry is to establish the absorbed dose to water, D_w, under reference conditions. Accuracy requirements for radiotherapy demand for a continuous improvement of dosimetry methods and adaption of dosimetry (primary) standards for new applications, including the introduction of new treatment modalities (e.g. FFF) and reference conditions (e.g. magnetic fields in MRgRT) in the clinic. However, existing dosimetry protocols are not always applicable for rapidly emerging new treatment modalities, while for primary standard dosimetry laboratories it is generally not feasible to acquire such modalities. Therefore, it was strongly desired that D_w measurements with primary standards could be performed on-site in clinical beams for the new treatment modalities. By this means, it would be possible to characterize and calibrate detectors with a target uncertainty that agrees with the accuracy requirements for the final dose delivery to the patient, not exceeding the 1 % ($k = 1$) target uncertainty for D_w in reference dosimetry. The aim of this thesis was to develop a transportable absorbed dose to water primary standard, a water calorimeter with the objective to measure ion chamber correction factors k_Q and k_B with a target relative standard uncertainty of 0.6 % ($k = 1$).

In Chapter 2 a new water calorimeter is described, developed for operation on-site in various beam geometries including MRI-incorporated treatment machines. The new calorimeter was successfully validated in the VSL ^{60}Co beam and on-site in clinical MV-photon beams. Excellent agreement of 0.1 % was achieved with previous ^{60}Co field calibrations, i.e. well within the uncertainty of the previous calorimeter, and with measurements performed in horizontal and vertical MV-photon beams. The k_Q factors determined for two PTW 30013 ionization chambers, agreed very well with available literature data. The relative combined standard uncertainty ($k = 1$) for D_w measurements in ^{60}Co and MV-photons is 0.37 % ($k = 1$). Calibrations were carried out with a standard uncertainty of 0.42 % and k_Q-factors are determined with a standard uncertainty of 0.40 %.

Chapter 3 describes the verification of the new primary standard in the on-going BIPM key comparison for accelerator beams, BIPM.RI(I)-K6. The comparison took place between 23 September to 20 October 2014 at the accelerator facilities of the National Physical Laboratory (Teddington, UK). The comparison results, reported as ratios of the

VSL and the BIPM evaluations (and with the combined standard uncertainties given in parentheses), are 0.9959(54) at 6 MV, 0.9958(64) at 10 MV and 0.9991(75) at 25 MV. The key comparison results led to a set of degrees of equivalence for VSL water calorimeter, resulting in registration of related calibration measurement capabilities in the BIPM key comparison database (BIPM 2019). This provided the required evidence for international acceptance of the calorimeter as the Dutch absorbed dose to water primary standard for accelerator photon beams, ensuring acceptance of its measurement results through the CIPM Mutual Recognition Arrangement, CIPM MRA.

In Chapter 4 the application of the calorimeter is described to measure for the first time k_Q factor in accelerator flattening filter free (FFF) beams and to assess the applicability of ion chamber k_Q factors from existing Codes of Practice (CoPs), based on conventional flattening filter (cFF) beams. The measurements were performed in FFF-cFF beam pairs at 6 MV and 10 MV of an Elekta Versa HD for a selection of three different Farmer-type ion chambers (8 serial numbers) and were corrected for recombination and beam radial non-uniformity. The ratio of measured k_Q factors of the FFF-cFF beam pairs were compared with the $TPR_{20,10}$ CoPs of the NCS and IAEA and the $\%dd(10)_x$ CoP of the AAPM. For the $TPR_{20,10}$ based CoPs differences less than 0.19 % were found in k_Q factors between the corresponding FFF-cFF beams with standard uncertainties smaller than 0.35 %, while for the $\%dd(10)_x$ these differences were smaller than 0.42 % and within the expanded uncertainty of the measurements. Based on the measurements made with the new equipment described in this study the authors conclude that the k_Q factors provided by the NCS-18 and IAEA TRS-398 codes of practice can be applied for flattening filter free beams without additional correction. However, existing codes of practice ignoring the significant volume averaging effect of the FFF beams over the ion chamber cavity cannot be applied. Here, a corresponding volume averaging correction must be applied.

Chapter 5 describes commissioning of the calorimeter in the 7 MV-photon beam of a pre-clinical MRI-linac in a 1.5 T magnetic field. This resulted in D_w measurements with a magnetic field of 1.5 T and, after ramp-down, without magnetic field. It was shown that the measurement of ΔT_w and calorimeter corrections are either independent of magnetic field or can be determined in a magnetic field. The chemical heat defect, h, was considered zero within its stated uncertainty, as for 0 T. Evaluation of the magneto-caloric effect (MCE) and measurements done during magnet ramp-down, indicated no changes in the specific heat capacity, c_p, of water. However, variations of the applied monitor system increased the uncertainty on beam output normalization. This study confirmed that the uncertainty for measurement of D_w with a water calorimeter in a 1.5 T magnetic field is estimated to be the same as under conventional reference conditions.

7

It is concluded that the VSL water calorimeter can be applied as a primary standard for D_w in magnetic fields and is currently the only primary standard operable in a magnetic field that provides direct access to the international traceability framework.

In Chapter 6 the application of the calorimeter is described to measure for the first time k_Q and k_B factors in the 7 MV-photon beam of a pre-clinical MRI-linac in a 1.5 T magnetic field. This was done for 6 waterproof ion chambers (3 × PTW 30013 and 3 × IBA FC65-G) in a pre-clinical 7 MV MRI-linac at 0 T and at 1.5 T. The resulting k_Q factors for the PTW and IBA chambers were respectively 0.985(5) and 0.990(4). The k_B factors were measured with the chambers both in antiparallel direction to the magnetic field (∥ 180°), and perpendicular direction (⊥ -90°). The $k_{B\parallel}$ and $k_{B\perp}$ values for the PTW chambers were respectively 0.985(6) and 0.963(4) and for IBA chambers 0.995(4) and 0.956(4). The values were shown to agree with the available literature values. The values in this study are currently the only available measured values for k_Q and k_B in an MRI-linac that are directly linked to the international traceability framework for the quantity absorbed dose to water, D_w.

8

General discussion and conclusion

8.1. A new primary standard for external beam radiotherapy

8.1.1. A transportable primary standard for ^{60}Co and MV-photon beams

Water calorimetry is generally considered to be the most direct way of determining D_w (Seuntjens and Duane 2009, Andreo *et al* 2000). This thesis describes the successful introduction of a transportable water calorimeter as an internationally accepted primary standard for the realization of the quantity absorbed dose to water, D_w, on-site in ^{60}Co and clinical MV-photon beams. The thermostat phantom, equipment and measurement methods showed its proficiency by successful participation in the on-going BIPM key comparisons, BIPM.RI(I)-K6, in accelerator photon beams and BIPM.RI(I)-K4 in ^{60}Co beams (Burns *et al* 2017, Kessler *et al* 2018). The calorimeter demonstrated its performance and versatility for application in the PSDL and on-site clinical environments. Its measurement uncertainties have been shown to be independent on the presence of a magnetic field and comparable in magnitude to those of other (non-transportable) primary standards, also registered in the BIPM key comparison database (BIPM 2019). Currently, the BIPM graphite calorimeter (see Chapter 3), and the new water calorimeter described in this thesis are the only transportable, internationally accepted absorbed dose to water primary standards suitable for on-site measurements.

Any primary standard is of limited value if its results cannot be disseminated for application to the end-user. The new water calorimeter is purposely built to calibrate detectors directly in terms of absorbed dose to water inside the calorimeter thermostat phantom, providing a direct link to the international system of units (SI, *Système International*). Uncertainties in detector calibration coefficients are minimized by avoiding a conversion for *absorbed dose to water in the calorimeter thermostat* to *absorbed dose to water in a calibration phantom*.

Despite that the new calorimeter is built to be used on-site in clinical environments, routine application of water calorimetry in the clinic is not yet feasible for practical reasons. The water calorimeter is currently used as the Dutch national standard for absorbed dose to water in ^{60}Co beams. Its performance is also demonstrated for accurate calibration of secondary standards as well as measurement of ion chamber k_Q and k_B factors in modern radiotherapy facilities such as FFF beams and MRgRT facilities.

8.1.2. Traceable measurements for the MRI-linac

This thesis shows that water calorimetry, by first principles, is unaffected by the presence of a constant magnetic field. It is currently the only internationally accepted primary standard that can be operated in recently introduced MRgRT devices and therefore the

only method that provides a direct link to the international traceability framework and the international system of unites (SI) for dosimetry in MRgRT facilities.

Several groups are currently working on traceable measurements in MRI-linacs. Promising results were obtained with alanine dosimetry (Billas *et al* 2018) and the method described by van Asselen *et al* (2018), where k_B factors were determined by ion chamber measurements with and without magnetic field. Also, a feasibility study applying a small graphite calorimeter (Renaud *et al* 2016b) showed promising results in a 1.5 T magnetic field, however still with rotational variations of the order of 1 %. This method is challenged due to the detector's material inhomogeneities and densities.

8.1.3. Current state of the art: advantages and challenges

The water calorimeter described in this thesis has several advantages. It uses a compact thermostat phantom and measurement equipment. It reaches a thermally stable operation temperature quickly, i.e. overnight. It is transportable and can be fully utilized on-site in clinical treatment machines. It was designed to operate in horizontal beams, vertical beams and treatment bores with diameters down to 70 cm. Compared to e.g. graphite calorimetry and ionometry, in water calorimetry only a few beam dependent correction factors are needed without the need for complex (Monte Carlo) calculations. The most important water calorimeter corrections are those for conductive heat transport, k_C, and perturbation of non-water materials, k_{HPC}.

There are, however, a few remaining challenges. With a mass of approximately 100 kg, the calorimeter is heavy. For its positioning inside a 70 cm treatment bore the patient couch needs to be removed and an additional frame is needed to support the calorimeter. This is impractical for routine type measurements. Improved application under these conditions requires a reduction in size and weight, such that it would fit on the treatment couch. A reduction of size, without compromising its thermal performance and dosimetric characteristics, can only be achieved by thermal re-engineering of the thermostat enclosure. A reduction of mass would follow its size and could further be improved by choice of different materials.

Further improvements would involve better beam output monitoring for measurements in magnetic fields. Due to the applied monitor system in the current thesis, an additional Type A uncertainty of up to 0.26 % ($k = 1$) was found in the D_w measurements. This directly affected the uncertainties of the ion chamber calibration coefficients and k_B factors. Improvements in the linac internal monitor system could reduce this Type A uncertainty in future measurements.

8.1.4. Application in other beam modalities

In other studies, the application of absorbed dose to water primary standards in various beam modalities has been investigated. Water calorimetry was shown applicable or feasible in e.g. kV x-rays (de Prez and de Pooter 2008, Büermann *et al* 2016), electron beams (Renaud *et al* 2016a) and proton beams (Sassowsky and Pedroni 2005, Medin 2010, Sarfehnia *et al* 2010, Renaud *et al* 2016a, Mulder 2018). The application of water calorimeter in small non-reference fields is challenged by the limitations of the heat transport correction, k_C (Krauss 2006a, de Prez and de Pooter 2009), and is currently limited to fields larger than 3 cm.

8.2. Future perspective

This thesis shows that a great potential of the new calorimeter is its ability to accurately characterize detector types in a variety of new treatment modalities. When it would be desirable to apply calorimetry routinely in a clinical environment, a reduction in weight and size would be essential. However, new treatment modalities will be introduced continuously with a demand for detector characterization in terms of absorbed dose to water. These measurements also require continuous improvement of the water calorimeter. E.g. a (dynamic) variation of calorimeter measurement depth for measurement of beams of charged particles is desired.

Based on its current characteristics and with suitable modifications and validation, the possibilities of the new primary standard are virtually unlimited and can, with the necessary effort, be extended to any treatment modality. Therefore, the primary standard can provide an impulse on the development of new detector types that are suited for application under specific conditions. This could be done by direct on-site characterization and calibration of new detectors, specifically developed for dedicated treatment modalities and new clinical applications. Subsequently, these detectors and applications could boost accurate measurements for safe clinical introduction of new treatment modalities that impact directly on the improvement of accuracy in radiotherapy.

8.3. General conclusion

This thesis describes the successful introduction of water calorimeter as an internationally accepted primary standard for the realization of the quantity absorbed dose to water, D_w in the unit Gy, in clinical accelerator photon beams. In its current form, the water calorimeter demonstrated its applicability to calibrate and characterize dosimetry detectors in non-conventional clinical reference conditions. The uncertainties

for generic k_Q and $k_{Q,B}$ factors have been shown to meet the requirement of 0.6 % ($k = 1$, see section 1.8), with standard uncertainties for individual chambers smaller than 0.4 % (section 6.3.3).

Future applications of the primary standard can contribute to the fast and safe adoption of new treatment modalities in the clinic, by providing direct characterization of new detectors in new treatment modalities. This will have a direct impact on an improved accuracy in reference dosimetry for external beam radiotherapy, especially when new treatment modalities are introduced.

8

9

Samenvatting

Radiotherapie maakt gebruikt van ioniserende straling om kankercellen te doden en daarmee tumoren te vernietigen. De straling dringt diep in het lichaam door waarbij deze door energieafgifte schade aanricht aan weefsel. Door uit verschillende richtingen te stralen naar hetzelfde centrum in de tumor wordt een hoge stralingsdosis afgegeven aan het tumorweefsel waarbij de dosis over het gezonde weefsel wordt uitgesmeerd dat zodoende wordt gespaard.

Teletherapie is de meest gebruikte vorm van radiotherapie. Bij teletherapie worden bundels ioniserende straling, afkomstig van bestralingsapparatuur buiten de patiënt, op de tumor gericht. Voorafgaand aan de bestraling wordt door de radiotherapeut, op basis van medische beeldvorming de tumor ingetekend en de vereiste dosis voorgeschreven, alsook de maximaal toelaatbare dosis in kritieke organen. Het beheer, onderhoud en de kalibratie van alle bestralingsapparatuur wordt uitgevoerd door de klinisch fysicus en de klinisch fysisch medewerker als onderdeel van de fysica-groep in de radiotherapieafdeling.

Een geslaagde behandeling heeft minimale bijeffecten en de best mogelijke kwaliteit-van-leven voor de patiënt. Het succes van een behandeling wordt onder andere bepaald door de *nauwkeurigheid* waarmee de gewenste dosis (zoals vooraf berekend) in de patiënt overeenkomt met de daadwerkelijk afgegeven dosis. Dit is van belang tijdens een individuele patiëntbehandeling maar ook voor wetenschappelijke onderzoek bij de introductie van nieuwe behandelmethoden waarbij het effect van de afgegeven dosis (dosis-effect-relatie) bij patiënten wordt bestudeerd. Deze onderzoeken, clinical-trials genaamd, vormen de basis voor beslissingen van artsen bij de behandeling van toekomstige patiënten.

Eén van de voorwaarden voor nauwkeurige bestraling is nauwkeurige *kalibratie*[15] van bundels ioniserende straling. Kalibratie van teletherapiebundels vindt plaats in de grootheid *geabsorbeerde dosis in water*[16], D_w (de mens bestaat namelijk voor het grootste gedeelte uit water). Dit gebeurt met behulp van detectoren, zogenaamde ionisatiekamers. Hierbij is D_w gedefinieerd als de afgegeven energie door ioniserende straling per eenheid van massa in water, in de eenheid gray (1 gray is gelijk aan 1 joule per kilogram). Ionisatiekamers zelf worden ook gekalibreerd en wel in bundels straling afkomstig van de radioactieve bron Cobalt-60 (^{60}Co), onder 'normale' omstandigheden, zonder

---

15   kalibratie: het vergelijken van een meetwaarde van een meetinstrument met dat van een (primaire) meetstandaard met betrekking tot de gewenst grootheid

16   geabsorbeerde dosis in water: de hoeveelheid stralingsenergie die door water wordt opgenomen. De eenheid van energie is Joule (J) de hoeveelheid water wordt uitgedrukt in massa met de eenheid kilogram (kg).

magneetveld. Deze referentiebundels worden ook wel aangeduid met het symbool Q_0. Het gedrag van ionisatiekamers is afhankelijk van het type stralingsbundel en verandert drastisch bij de aanwezigheid van een magneetveld. Om ionisatiekamers te gebruiken in deze bundels, aangeduid met Q, of bij de aanwezigheid van een sterk magneetveld, aangeduid met B, worden correctiefactoren (*k*-factoren) gebruikt om voor het verschil te compenseren. Dit zijn k_Q-factoren voor de bundelkwaliteit Q en k_B-factoren voor aanwezigheid van een magneetveld B. Het product van k_Q en k_B kan worden weergegeven als $k_{Q,B}$. Bij afwezigheid van een magneetveld is k_B gelijk aan 1 en is $k_{Q,B}$ dus gelijk aan k_Q.

Fysische grootheden zoals bijvoorbeeld *lengte* (*l*), *massa* (*m*), *elektrische stroom* (*I*) of *geabsorbeerde dosis in water* (D_w) worden uitgedrukt in fysische eenheden zoals *meter* (m), *kilogram* (kg), *ampère* (A) en *gray* (Gy). Het gebruik en de definitie van eenheden is afgesproken in het Internationale Systeem van eenheden (*SI*, Systèm International d'unités). *De praktisch realisatie van een eenheid voor een bepaalde grootheid*[17] vindt plaats met behulp van een primaire (meet)standaard. Primaire standaarden voor dosimetrie in de radiotherapie zijn gebaseerd op watercalorimeters, grafietcalorimeters of speciaal ontwikkelde ionisatiekamers. Bij watercalorimetrie wordt de geabsorbeerde dosis als gevolg van straling gemeten door een temperatuurverhoging in water. Dit wordt algemeen beschouwd als de meest directe methode voor realisatie van de eenheid Gy voor D_w (1 gray in water geeft een temperatuursverhoging van 0,00024 °C). Iedere meting heeft een bepaalde *nauwkeurigheid*[18]. De nauwkeurigheid van een meting hangt af van verschillende factoren zoals bijvoorbeeld de kwaliteit van het gebruikte meetinstrument, variaties in omgevingstemperatuur of luchtdruk, maar ook variaties in de grootheid van het te meten onderwerp zoals variaties in bundelsterkte bij radiotherapie. Als maat voor de nauwkeurigheid van een meting wordt de *meetonzekerheid* toegepast. Hoe kleiner de meetonzekerheid hoe groter de nauwkeurigheid.

In het algemeen geldt dat, om metingen in radiotherapie-instituten wereldwijd met elkaar te kunnen vergelijken zijn betrouwbare meetresultaten essentieel. Dit is gebaseerd op een internationaal systeem van metingen waarbij meetresultaten middels een ononderbroken keten van kalibraties te herleiden zijn naar internationaal geaccepteerde primaire standaarden. Echter, de veilige en effectieve klinische introductie van nieuwe bestralingstechnieken wordt gehinderd als dit systeem van *metrologische herleidbaarheid* ontbreekt.

---

17 iedereen kan met de juiste middelen op basis van natuurkundige constanten en meetmethoden zelf een primaire standaard bouwen en daarmee de eenheid volgens de definitie *realiseren*

18 *naukeurigheid*: de mate van overeenkomst tussen een meetwaarde van een bepaalde grootheid en de (onbekende) werkelijke waarde van de te meten grootheid

9

Ook tijdens radiotherapiebehandelingen en wetenschappelijk onderzoek geldt dat betrouwbare metingen essentieel zijn. Hierin zit de behoefte aan primaire dosimetriestandaarden en dosimetrieprotocollen. Huidige dosimetrieprotocollen zijn vooral gebaseerd op referentiebundels van ^{60}Co, maar met de introductie nieuw bundelmodaliteiten (bijv. vlakheidsfilter-vrije, FFF, fotonenbundels, protonen, etc.) of de toepassing van magneetvelden kan niet zonder meer worden volstaan met herleidbaarheid naar ^{60}Co alleen. Metingen met primaire dosimetriestandaarden onder deze omstandigheden zijn noodzakelijk. Vanwege de hoge kosten voor deze faciliteiten is het voor nationale metrologie instituten (NMIs) niet haalbaar om de nieuwste bestralingsfaciliteiten zelf aan te schaffen. Daaruit volgt dat primaire standaarden voor de radiotherapie transportabel moeten zijn, zodat er op locatie, in de kliniek gemeten kan worden voor dergelijke nieuw ontwikkelde bestralingsapparatuur.

Dit proefschrift beschrijft de realisatie en internationale acceptatie van een nieuwe transportabele primaire dosimetriestandaard voor herleidbare metingen in de moderne radiotherapie, een watercalorimeter.

Hoofdstuk 1 beschrijft het doel van nauwkeurige metingen in de radiotherapie en de eisen die gesteld worden aan de onzekerheid bij het meten van de grootheid geabsorbeerde dosis in water, D_w. Op internationaal niveau is metrologische herleidbaarheid geregeld via het internationale standaardenlaboratorium, het BIPM (Bureau International des Poids et Mesures) in Sèvres. Het BIPM staat onder toezicht van het CIPM (Comité International des Poids et Mesures, Sèvres). In het kader van de CIPM-MRA (CIPM - Mutual Recognition Arrangement), erkennen alle deelnemende landen elkaars kalibratie- en meetcertificaten voor de grootheden, bereiken en meetonzekerheden waar succesvol is deelgenomen aan vergelijkingen (key comparisons) georganiseerd door het BIPM. Er vinden continu nieuwe ontwikkelingen plaats in de radiotherapie. Recentelijk zijn er toepassingen geïntroduceerd op basis van hoogenergetische (megavolt, MV) fotonenbundels zonder vlakheidsfilter (flattening-filter free, FFF-bundels) en MR gestuurde radiotherapie (MR-guided Radiotherapy, MRgRT). Deze ontwikkelingen hebben geleid tot een toename van de complexiteit voor herleidbare metingen. Het gevolg is een noodzaak om voor nieuwe toepassingen correctiefactoren aan te passen, in geval van k_Q voor FFF-bundels, of te herzien, in geval van k_B voor MRgRT. Deze correctiefactoren kunnen worden gemeten voor individuele ionisatiekamers of voor een ionisatiekamertype. Voor het meten van deze correctiefactoren is toepassing van primaire dosimetriestandaarden in klinische bundelkwaliteit noodzakelijk.

De maximaal toelaatbare standaard onzekerheid voor referentiedosimetrie in de kliniek is afhankelijk van de klinische toepassing en ligt tussen 1,0 % en 1,5 %. Dit leidt tot een onzekerheidseis voor de bepaling van k_Q, k_B en $k_{Q,B}$ die ligt tussen 0,6 % en 1,2 %.

Hoofdstuk 2 beschrijft het ontwerp, de realisatie en de werking van een nieuwe transportabele watercalorimeter. De calorimeter is ontwikkeld voor metingen op locatie in diverse moderne radiotherapiebundels, waaronder klinische versnellers met geïntegreerde MRI scanners (MRI versnellers). De nieuwe calorimeter is succesvol gevalideerd in de ^{60}Co bundel van *VSL*[19] en op locatie in klinische megavolt (MV) fotonenbundels. De overeenkomst tussen de nieuwe watercalorimeter en de voorgaande watercalorimeter, die dienstdeed tussen 2002 en 2014) was uitstekend. De verschillen in D_w-meting tussen de twee calorimeters was kleiner dan 0.1 %, veel kleiner dan de onzekerheid in de D_w van beide calorimeters. Validatie van de nieuwe calorimeter in horizontale en verticale MV-fotonenbundels liet geen significante verschillen zien, wat aantoonde dat de calorimeter in beide oriëntaties naar verwachting functioneert. De in deze studie gemeten k_Q-factoren voor PTW 30013 ionisatiekamers kwamen binnen de meetonzekerheid overeen met die in de literatuur.

De relatieve standaard onzekerheid voor meting van geabsorbeerde dosis in water in MV-fotonen is 0,37 %. Deze studie laat zien dat kalibraties van ionisatiekamers kunnen worden uitgevoerd met een relatieve standaard onzekerheid van 0,42 % en dat k_Q-factoren kunnen worden gemeten met een relatieve standaardonzekerheid van 0,40 %.

Hoofdstuk 3 beschrijft de vergelijking tussen de primaire standaarden voor geabsorbeerde dosis in water van VSL en BIPM in het kader van keycomparison BIPM.RI(I)-K6. Deze vergelijking vond plaats tussen 23 september en 20 oktober 2014 in de versnellerfaciliteit van het Britse nationale metrologie instituut (National Physical Laboratory, NPL, in Teddington). De metingen vonden plaats in MV-fotonenbundels met nominale energieën van 6 MV, 10 MV en 25 MV. De vergelijkingsresultaten zijn gerapporteerd als verhoudingen van meetresultaten tussen VSL en het BIPM met de standaardonzekerheden als de laatste significante cijfers tussen haakjes: 0,9959(54) in 6 MV, 0,9958(64) in 10 MV en 0,9991(75) in 25 MV. Deze vergelijkingsresultaten hebben

---

19 VSL – Dutch Metrology Institute (https://www.vsl.nl/) is het nationaal metrologisch instituut (NMI) van Nederland. VSL maakt meetresultaten van bedrijven, ziekenhuizen, laboratoria en instellingen direct herleidbaar naar internationale meetstandaarden (SI-eenheden). Het beheer en de ontwikkeling van dé nationale meetstandaarden behoort tot een van de kerntaken van de organisatie.

geleid tot zogenaamde *Degrees of Equivalence*[20] voor de VSL watercalorimeter, met als resultaat registratie van de betreffende CMCs (Calibation Measurement Capabilities) in de BIPM key comparison database (KCDB).

Deze studie levert het benodigde bewijs voor internationale acceptatie van de calorimeter als de Nederlandse primaire standaard voor geabsorbeerde dosis in water in MV-fotonenbundels. Sindsdien is de nieuwe calorimeter ook in gebruik als de Nederlandse primaire standaard. Dit verzekert internationale acceptatie van meetresultaten via de CIPM-MRA.

Hoofdstuk 4 beschrijft een toepassing van de transportabele watercalorimeter, waarbij voor de eerste keer k_Q-correctiefactoren voor ionisatiekamers zijn gemeten in vlakheidsfiltervrije MV-fotonenbundels (flattening-filter free, FFF). Het doel van deze studie was om te bepalen of k_Q-factoren voor conventionele bundels met vlakheidsfilter (cFF-bundels) zoals gegeven in huidige dosimetrieprotocollen toepasbaar zijn in FFF-bundels. De ionisatiekamermetingen, gecorrigeerd voor recombinatie en bundel-non-uniformiteit zijn uitgevoerd in FFF-cFF bundelparen van 6 MV en 10 MV afkomstig van een Elekta Versa HD klinische lineaire versneller bij het Antoni van Leeuwenhoek (NKI-AVL) in Amsterdam. Voor drie verschillende Farmer-type ionisatiekamers (8 serienummers) zijn k_Q-factoren gemeten. De verhouding van gemeten k_Q-factoren FFF-cFF bundelparen zijn vergeleken met die uit gangbare dosimetrieprotocollen op basis van bundelkwaliteitsparameters, aageduid met $TPR_{20,10}$ en $\%dd(10)_x$. Met betrekking tot de $TPR_{20,10}$ protocollen (NCS-18 en IAEA TRS-398) waren de verschillen kleiner dan 0,19 % met een relatieve standaardonzekerheid van 0,35 %. Met betrekking tot het $\%dd(10)_x$ protocol (AAPM TG-51) waren de verschillen kleiner dan 0,42 %. In beide gevallen waren de verschillen kleiner dan de uitgebreide onzekerheid ($k = 2$) van de meting.

Op basis van de metingen uitgevoerd met de instrumenten beschreven in deze studie kan geconcludeerd worden dat voor k_Q-factoren gegeven in bestaande dosimetrieprotocollen, geen aanvullende correctie nodig is voor toepassing van de gegeven k_Q-factoren in FFF bundels. Echter, bestaande dosimetrieprotocollen kunnen niet toegepast worden zonder een aanvullende correctie voor variatie van het dosisprofiel over de lengte van de ionisatiekamer. Deze correctie moet wel worden toegepast.

---

20 *Degrees of Equivalence* (mate van gelijkheid): de internationale term voor de mate waarin meetresultaten met elkaar overeenstemmen

Hoofdstuk 5 beschrijft de validatie van de watercalorimeter in een 7 MV-fotonenbundel van een pre-klinische MRI-versneller in een 1.5 T magnetisch veld. Dit resulteerde in D_w metingen in een 1,5 T magneetveld en zonder magneetveld (bij 0 T). De studie liet zien dat de meting van de stralingsgeïnduceerde temperatuurverandering, ΔT_w onafhankelijk is van het aanwezige magneetveld. Correctiefactoren van de calorimeter kunnen worden bepaald zoals bij metingen zonder magneetveld. Het chemische warmtedefect, h, is verwaarloosbaar verondersteld binnen de bijbehorende standaardonzekerheid zoals bepaald zonder magneetveld (bij 0 T). Evaluatie van het magneto-calorische effect (MCE of adiabatische demagnetisatie) en metingen verricht gedurende de ramp-down van de magneet gaven geen aanleiding om een verandering van specifieke warmtecapaciteit, c_p, van water te veronderstellen. Echter, variaties in het toegepaste bundelmonitorsysteem gaven wel aanleiding tot een verhoogde Type A onzekerheid als gevolg van normalisatie van de D_w metingen. Deze studie bevestigde dat de onzekerheid voor de meting van D_w niet wordt beïnvloed door de aanwezigheid van een sterk magneetveld in vergelijking met metingen zonder magneetveld.

De transportabele watercalorimeter kan worden toegepast als primaire standaard voor D_w in constante magneetvelden en is momenteel de enige primaire standaard die metingen kan leveren herleidbaar naar het hoogste internationale niveau.

Hoofdstuk 6 beschrijft toepassing van de transportabele watercalorimeter voor metingen van ionisatiekamercorrectiefactoren k_Q (bij 0 T) en k_B bij aanwezigheid van een magneetveld. Deze metingen zijn uitgevoerd in een 7 MV-fotonenbundel van een pre-klinische MRI-versneller bij aanwezigheid van een 1,5 T magneetveld. Dit is uitgevoerd voor 6 waterdichte ionisatiekamers (3 × PTW 30013 en 3 × IBA FC65-G) bij 0 T en bij 1,5 T. De gemeten k_Q factoren voor de PTW en de IBA kamers waren respectievelijk 0,985(5) en 0,990(4). De k_B-factoren zijn gemeten in antiparallel-oriëntatie ten opzichte van het magneetveld (∥ -180°), $k_{B\parallel}$, en in loodrechte-oriëntatie ten opzichte van het magneetveld (⊥ 90°), $k_{B\perp}$. De waarden van $k_{B\parallel}$ en $k_{B\perp}$ voor de PTW ionisatiekamer waren respectievelijk 0,985(6) en 0,963(4) en voor de IBA kamers 0,995(4) en 0,956(4). De beschikbare literatuurwaarden voor k_B vertonen een vrij grote spreiding met standaarddeviaties tussen 0.5 % en 1.2 %. Echter de gemiddelden hiervan waren overeenstemming met de nieuw gemeten waarden. Internationale herleidbaarheid is gebaseerd op de overeenkomst van meetresultaten uit vergelijkingen. Voor dosimetrie in magneetvelden bestaan nog geen internationale vergelijkingen. Hoofdstuk 3 leverde het benodigde bewijs voor internationale acceptatie van de calorimeter als de Nederlandse primaire standaard voor geabsorbeerde dosis in water in MV-fotonenbundels (zonder magneetveld). Hoofdstuk 5 liet zien dat de meetresultaten verkregen met de nieuwe

9

watercalorimeter niet beïnvloed worden door een aanwezig magneetveld.

Op basis hiervan kan worden gesteld dat k_Q- en k_B-factoren, in de huidige studie, op basis van de nieuwe watercalorimeter herleidbaar zijn naar het internationale metrologie netwerk voor dosimetrie in de radiothreapie. De nieuwe watercalorimeter momenteel de enige primaire geabsorbeerde-dosis standaard voor metingen in magneetvelden.

Hoofdstuk 7 bevat de Engelstalige samenvatting van het proefschrift.

Hoofdstuk 8 bevat de algemene discussie en conclusie van het proefschrift dat een succesvolle introductie beschrijft van een nieuwe transportabele watercalorimeter voor metingen in teletherapie. Het is momenteel de enige primaire standaard die aantoonbare internationale herleidbaarheid levert voor de modernste teletherapietoepassingen. Voor toekomstige routinematige toepassing in de kliniek zijn een aantal aanpassingen wenselijk. Deze aanpassingen hebben betrekking op het verkleinen van de afmetingen en het gewicht zonder de thermische prestaties of dosimetrische eigenschappen te beïnvloeden. Tevens zal het onafhankelijke bundelmonitorsysteem in MRgRT toepassingen verbeterd moeten worden. Toepassing van de calorimeter in andere bundelmodaliteiten zoals bijv. MeV-protonen- of MeV-elektronenbundels vergt aanpassing van positionering van detectoren op verschillende dieptes in water.

Toekomstige toepassingen van de transportabele watercalorimeter kunnen een impuls geven tot de ontwikkeling van nieuwe detectoren, welke op hun beurt bijdragen aan nauwkeurige metingen voor een veilige introductie van nieuwe bestralingstechnieken.

10

Addenda

References, Publications, Dankwoord, Curriculum Vitae

References

Aalbers A H L 2003 *Status report on the NMi portable water calorimeter* CCRI(I) Sèvres, Paris

Aalbers A H L, Hoornaert M-T, Minken A, Palmans H, Pieksma M W H, De Prez L A, Reynaert N, Vynckier S and Wittkämper F W 2008 *NCS Report 18: Code of practice for the absorbed dose determination in high energy photon and electron beams* Delft

ADWG(I) 2017 *Compariosn of absorbed dose to water at high photon energies at a reference facility* Sèvres, Paris

Allisy P J, Burns D T and Andreo P 2009 International framework of traceability for radiation dosimetry quantities *Metrologia* **46** S1–8

Almond P R, Biggs P J, Coursey B M, Hanson W F, Huq M S, Nath R and Rogers D W O 1999 AAPM's TG-51 protocol for clinical reference dosimetry of high-energy photon and electron beams *Med. Phys.* **26** 1847–70

Andreo P 1992 Absorbed dose beam quality factors for the dosimerty of high-energy photon beams *Phys. Med. Biol.* **37** 2189–211

Andreo P, Burns D, Nahum A, Seuntjens J and Attix F H 2017 *Fundamentals of Ionizing Radiation Dosimetry* Wiley-VCH Berlin

Andreo P, Burns D T, Hohlfeld K, Huq M S, Kanai T, Laitano F, Smyth V G, Vynckier S, Hohlfield K, Huq M S, Kanai T, Laitano F, Smyth V G and Vynckier S 2000 *IAEA TRS-398: Absorbed Dose Determination in External Beam Radiotherapy* Technical Report Series, 2000 International Atomic Energy Agency Vienna, Austria

van Asselen B, Woodings S J, Hackett S L, van Soest T L, Kok J G M, Raaymakers B W and Wolthaus J W H 2018 A formalism for reference dosimetry in photon beams in the presence of a magnetic field *Phys. Med. Biol.* **63** 125008

Berger M J, Coursey J S, Zucker M A and Chang J 2005 Stopping-Power and Range Tables for Electrons, Protons, and Helium Ions *ESTAR, ASTAR and PSTAR* Online: https://www.nist.gov/pml/stopping-power-and-range-tables-electrons-protons-and-helium-ions-version-history

Billas I, de Prez L, de Pooter J and Duane S 2018 Reference dosimetry in MRI-linac using alanine detector *6th MR in RT Symposium* Utrecht

BIPM 2019 KCDB The BIPM Key Comparison Database is available online Online: http://kcdb.bipm.org

Boutillon M 1998 Volume recombination parameter in ionization chambers *Phys. Med. Biol.* **43** 2061–72

Brahme A 1984 Dosimetric precision requirements in radiation therapy *Acta Oncol. (Madr).* **23** 379–91

Brahme A, Kraepelien T and Svensson H 1980 Electron and photon beams from a 50 MeV racetrack microtron. *Acta Radiol. Oncol.* **19** 305–19

van den Brom H E, Houtzager E, Rietveld G, van Bemmelen R and Chevtchenko O 2007 Voltage linearity measurements using a binary Josephson system *Meas. Sci. Technol.* **18** 3316–20

Bruggmoser G, Saum R, Schmachtenberg A, Schmid F and Schüle E 2007 Determination of the recombination correction factor k S for some specific plane-parallel and cylindrical ionization chambers in pulsed photon and electron beams *Phys. Med. Biol.* **52** N35–50

Budgell G, Brown K, Cashmore J, Duane S, Frame J, Hardy M, Paynter D and Thomas R 2016 IPEM topical report 1: guidance on implementing flattening filter free (FFF) radiotherapy *Phys. Med. Biol.* **61** 8360–94

Büermann L, Guerra A S, Pimpinella M, Pinto M, Pooter J de, Prez L de, Jansen B, Denoziere M and Rapp B 2016 First international comparison of primary absorbed dose to water standards in the medium-energy X-ray range *Metrologia* **53** 06007–06007

Burns D T 2006 A new approach to the determination of air kerma using primary-standard cavity ionization chambers *Phys. Med. Biol.* **51** 929–42

Burns D T 2014 *The dose conversion procedure for the BIPM graphite calorimeter standard for absorbed dose to water* Sèvres, Paris

Burns D T and McEwen M R 1998 Ion recombination corrections for the NACP parallel-plate chamber in a pulsed electron beam. *Phys. Med. Biol.* **43** 2033–45

Burns D T, Picard S, Roger P, de Prez L A, Jansen B J, de Pooter J A, Burns D T, Roger P, de Prez L A, Jansen B J, Pooter J A, Picard S, Roger P, de Prez L A, Jansen B J and De Pooter J A 2017 Key comparison BIPM.RI(I)-K6 of the standards for absorbed dose to water of the VSL, Netherlands and the BIPM in accelerator photon beams *Metrologia* **54** 06005

Butler D J, Stevenson A W, Wright T E, Harty P D, Lehmann J, Livingstone J and Crosbie J C 2015 High spatial resolution dosimetric response maps for radiotherapy ionization chambers measured using kilovoltage synchrotron radiation *Phys. Med. Biol.* **60** 8625–41

CCRI 2013 *Report of the 24th meeting (17 May 2013) to the International Committee for Weights and Measures* Sèvres, Paris

Cen J 2011 *Report: Self-heat effect of thermistors for absorbed dose measurements* Delft

CIPM 2016 *Measurement comparisons in the CIPM MRA, CIPM MRA-D-05* Sèvres, Paris

CIPM 1999 Mutual recognition of national measurement standards and of calibration and measurement certificates issued by national metrology institutes Online: https://www.bipm. org/en/cipm-mra/

Cool J C, Schijff F J and Viersma T J 1991 *Regeltechniek* Overberg

Dalaryd M, Knöös T and Ceberg C 2014 Combining tissue-phantom ratios to provide a beam-quality specifier for flattening filter free photon beams *Med. Phys.* **41** 111716

DIN 2008 *6800-2:2008-03 Dosismessverfahren nach der Sondenmethode für Photonen- und Elektronenstrahlung* Deutsche Industrie Norm Berlin

Domen J K and Domen S R 2001 Studies of excess heat and convection in a water calorimeter *J. Res. Natl. Inst. Stand. Technol.* **106** 843–56

Domen S R 1994 A sealed water calorimeter for measuring absorbed dose *J. Res. Natl. Inst. Stand. Technol.* **99** 121–41

10

References

Domen S R 1982 An Absorbed Dose Water Calorimeter: Theory, Design, and Performance *J. Res. Natl. Bur. Stand. (1934).* **87** 211–35

Domen S R 1988 Convective velocity effects on a thermistor in water *J. Res. Natl. Bur. Stand. (1934).* **93** 603–12

EA 2013 *EA-4/02 M Evaluation of the Uncertainty of Measurement in Calibration*

Fallone B G 2014 The Rotating Biplanar Linac-Magnetic Resonance Imaging System *Semin. Radiat. Oncol.* **24** 200–2

Franco V, Blázquez J S, Ipus J J, Law J Y, Moreno-Ramírez L M and Conde A 2018 Magnetocaloric effect: From materials research to refrigeration devices *Prog. Mater. Sci.* **93** 112–232

Georg D, Knöös T and McClean B 2011 Current status and future perspective of flattening filter free photon beams *Med. Phys.* **38** 1280–93

Hackett S L, van Asselen B, Wolthaus J W H H, Kok J G M M G, Woodings S J, Lagendijk J J W W and Raaymakers B W 2016 Consequences of air around an ionization chamber: Are existing solid phantoms suitable for reference dosimetry on an MR-linac? *Med. Phys.* **43** 3961–8

Hohlfeld K 1988 The standard DIN 6800: Procedures for absorbed dose determination in radiology by the ionization method *Proc. 1987 Symp. Dosim. Radiother. (IAEA, Vienna) Vol 1* 13–24

IAEA 2017 *IAEA Human Health Series no. 31: Accuracy Requirements and Uncertainties in Radiotherapy* Vienna

IAEA 2008 Measurement Uncertainty - A practical Guide for Secondary Standards Dosimetry Laboratories **TECDOC-158** 1–53

IAPWS 2014 *Revised Release on the IAPWS Formulation 1995 for the Thermodynamic Properties of Ordinary Water Substance for General and Scientific Use* Revised Release 2014, ed T Petrova and R B Dooley International Association for the Properties of Water and Steam Moscow

ICRU 1979 *ICRU report 31: Average Energy Required To Produce An Ion Pair* 31 ICRU Washington

ICRU 2010 *ICRU report 83: Prescribing, Recording, and Reporting Photon-Beam Intensity-Modulated Radiation Therapy (IMRT)* 10 Washington

JCGM 2008 *Evaluation of measurement data — Guide to the expression of uncertainty in measurement* 100:2008, 100:2008 BIPM Sèvres, Paris

JCGM 2012 *International vocabulary of metrology – Basic and general concepts and associated terms (VIM)* 200:2012 Sèvres

Kawrakow I, Mainegra-Hing E, Rogers D W O, Tessier F and Walters B R B 2019 *The EGSnrc Code System: Monte Carlo Simulation of Electron and Photon Transport, NRCC Report PIRS-701* Ottawa

Keall P J, Barton M and Crozier S 2014 The Australian Magnetic Resonance Imaging-Linac Program *Semin. Radiat. Oncol.* **24** 203–6

Kessler C, Allisy-Roberts P J, Burns D T, Roger P, de Prez L A, de Pooter J A and Damen P M G 2009 *Final report: Comparison of the standards for absorbed dose to water of the VSL and the BIPM for Co-60 Gamma rays* 2009-05-31 Bureau International des Poids et Mesures Sèvres, Paris

Kessler C, Burns D, Jansen B J, de Pooter J A de and de Prez L A 2018 Comparison of the standards for absorbed dose to water of the VSL, The Netherlands, and the BIPM for 60 Co γ rays *Metrologia* **55** 06012–06012

Klassen N V and Ross C K 1997 Water Calorimetry : The Heat Defect *J. Reseach Natl. Inst. Stand. Technol.* **102** 63–74

Klevenhagen S C, Aukett R J, Harrison R M, C M, Nahum A E and Rosser K E 1996 The IPEMB code of practice for the determination of absorbed dose for x-rays below 300 kV generating potential (0 . 035 mm Al – 4 mm Cu HVL ; 10 – 300 kV generating potential) Prepared by a Working Party of the IPEMB with the following members : *Phys. Med. Biol.* **41** 2605

Krauss A 2002 Experimental verification of caluclated radiation-induced heat conduction effects in the water absorbed dose calorimeter *Thermochim. Acta* **382** 99–107

Krauss A 2006a Heat conduction effects during the calorimetric determination of absorbed dose to water in radiotherapy beams *Thermochim. Acta* **445** 126–32

Krauss A 2006b The PTB water calorimeter for the absolute determination of absorbed dose to water in ^{60} Co radiation *Metrologia* **43** 259–72

Krauss A and Kramer H-M 2003 The heat defect in the PTB water calorimeter: A discussion on uncertainty *Workshop on Recent Advances in Absorbd Dose Standards* ed R Huntley, D Webb, M Cox, D Butler, L Kotler and R Argent ARPANSA Melbourne pp 15–6

Krauss A and Roos M 1998 Heat conduction, convection and radiolysis of the H_2/O_2 system in the water absorbed dose calorimeter *Thermochim. Acta* **310** 53–60

Lagendijk J J W, Raaymakers B W, Van den Berg C A T, Moerland M A, Philippens M E and van Vulpen M 2014a MR guidance in radiotherapy *Phys. Med. Biol.* **59** R349–69

Lagendijk J J W, Raaymakers B W and van Vulpen M 2014b The Magnetic Resonance Imaging-Linac System *Semin. Radiat. Oncol.* **24** 207–9

Lemmon E W, McLinden M O and Friend D G 2015 Thermophysical Properties of Fluid Systems *NIST Chem. Webb.*

Lillicrap S C, Owen B, Williams J R and Williams P C 1990 Code of Practice for high-energy photon therapy dosimetry based on the NPL absorbed dose calibration service *Phys. Med. Biol.* **35** 1355–60

LNHB 2010 Table de Radionucléides Co-60 *Lab. Natl. Henri Becquerel* Online: https://www.bipm.org/utils/common/pdf/monographieRI/Monographie_BIPM-5_Tables_Vol5.pdf

Lye J E, Butler D J, Oliver C P, Alves A, Lehmann J, Gibbons F P and Williams I M 2016 Comparison between the TRS-398 code of practice and the TG-51 dosimetry protocol for flattening filter free beams *Phys. Med. Biol.* **61** N362–72

Lye J E, Butler D J, Ramanathan G and Franich R D 2012 Spectral differences in 6 MV beams with matched PDDs and the effect on chamber response *Phys. Med. Biol.* **57** 7599–614

Malkov V N and Rogers D W O 2018 Monte Carlo study of ionization chamber magnetic field correction factors as a function of angle and beam quality *Med. Phys.* **45** 908–25

Malkov V N and Rogers D W O 2017 Sensitive volume effects on Monte Carlo calculated ion chamber response in magnetic fields *Med. Phys.* **44** 4854–8

McEwen M, DeWerd L, Ibbott G, Followill D, Rogers D W O, Seltzer S and Seuntjens J 2014 Addendum to the AAPM's TG-51 protocol for clinical reference dosimetry of high-energy photon beams *Med. Phys.* **41** 041501

McEwen M R 2010 Measurement of ionization chamber absorbed dose kQ factors in megavoltage photon beams *Med. Phys.* **37** 2179–93

McEwen M R and Duane S 2000 A portable calorimeter for measuring absorbed dose in the radiotherapy clinic *Phys. Med. Biol.* **45** 3675–91

McEwen M R and Taank J 2017 Examining the influence of humidity on reference ionization chamber performance *Med. Phys.* **44** 694–702

Medin J 2010 Implementation of water calorimetry in a 180 MeV scanned pulsed proton beam including an experimental determination of kQ for a Farmer chamber. *Phys. Med. Biol.* **55** 3287–98

10

References

Meijsing I, Raaymakers B W, Raaijmakers A J E, Kok J G M, Hogeweg L, Liu B and Lagendijk J J W 2009 Dosimetry for the MRI accelerator: the impact of a magnetic field on the response of a Farmer NE2571 ionization chamber *Phys. Med. Biol.* **54** 2993–3002

van der Merwe D, Van Dyk J, Healy B, Zubizarreta E, Izewska J, Mijnheer B and Meghzifene A 2017 Accuracy requirements and uncertainties in radiotherapy: a report of the International Atomic Energy Agency *Acta Oncol. (Madr).* **56** 1–6

Mijnheer B J, Battermann J J and Wambersie A 1987 What degree of accuracy is required and can be achieved in photon and neutron therapy? *Radiother. Oncol.* **8** 237–52

Mostert D 2014 *Report: Self-heat effect of the thermistors in the VSL water calorimeter* Delft

Mulder J 2018 *PhD thesis: Water calorimetry for proton therapy* Groningen

Mutic S and Dempsey J F 2014 The ViewRay System: Magnetic Resonance-Guided and Controlled Radiotherapy *Semin. Radiat. Oncol.* **24** 196–9

O'Brien D J, Roberts D A, Ibbott G S and Sawakuchi G O 2016 Reference dosimetry in magnetic fields: formalism and ionization chamber correction factors *Med. Phys.* **43** 4915–27

O'Brien D J, Sawakuchi G O, Brien D J O and Sawakuchi G O 2017 Monte Carlo study of the chamber-phantom air gap effect in a magnetic field *Med. Phys.* **44** 3830–8

O'Brien P F, Gillies B A, Schwartz M, Young C and Davey P 1991 Radiosurgery with unflattened 6-MV photon beams *Med. Phys.* **18** 519–21

Oborn B M, Metcalfe P E, Butson M J and Rosenfeld A B 2010 Monte carlo characterization of skin doses in 6 MV transverse field MRI-linac systems: Effect of field size, surface orientation, magnetic field strength, and exit bolus *Med. Phys.* **37** 5208–17

OIML 2007 *VOCABULARY OIML V 2-200 Edition 2007 (E/F) International Vocabulary of Metrology – Basic and General Concepts and Associated Terms (VIM)* 2007 Paris

Overweg J, Raaymakers B, Lagendijk J and Brown K 2009 System for MRI guided Radiotherapy *Proc. Intl. Soc. Mag. Reson. Med. 17 (2009) View publication stats* 594

Palmans H 2000 Proceedings of NPL Workshop on Recent Advances in Calorimetric Absorbed Dose Standards *Proc. NPL Work. Recent Adv. Calorimetric Absorbed Dose Stand.*

Palmans H, Andreo P, Saiful Huq M, Seuntjens J, Vatnitsky S, Meghzifene A and Christaki K 2017 *IAEA-AAPM TRS-483: Dosimetry of small static fields used in external beam radiotherapy* Vienna

Paynter D, Weston S J, Cosgrove V P, Evans J A and Thwaites D I 2014 Beam characteristics of energy-matched flattening filter free beams *Med. Phys.* **41** 052103

Picard S, Burns D T and Los Arcos J M 2013a Establishment of degrees of equivalence of national primary standards for absorbed dose to water in accelerator photon beams *Metrologia* **50** 06016

Picard S, Burns D T and Ostrowsky A 2011a *Determination of the recombination correction for the BIPM parallel plate ionization chamber type in a pulsed photon beam* Sèvres, Paris

Picard S, Burns D T and Roger P 2009 *Construction of an absorbed-dose graphite calorimeter* 1 Sèvres, Paris

Picard S, Burns D T and Roger P 2007 Determination of the specific heat capacity of a graphite sample using absolute and differential methods *Metrologia* **44** 294–302

Picard S, Burns D T and Roger P 2010a The BIPM Graphite Calorimeter Standard for Absorbed Dose to Water *International Symposium on Standards, Applications and Quality Assurance in Medical Radiation Dosimetry in Standards, Applications and Quality Assurance in Medical Radiation Dosimetry (IDOS)* Proceeding Series IAEA Vienna, Austria pp 55–65

Picard S, Burns D T, Roger P, Allisy-Roberts P J, Kapsch R P and Krauss A 2011b Key comparison BIPM.RI(I)-K6 of the standards for absorbed dose to water of the PTB, Germany and the BIPM in accelerator photon beams *Metrologia* **48** 06020–06020

Picard S, Burns D T, Roger P, Allisy-Roberts P J, McEwen M R, Cojocaru C D and Ross C K 2010b Comparison of the standards for absorbed dose to water of the NRC and the BIPM for accelerator photon beams *Metrologia* **47** 06025–06025

Picard S, Burns D T, Roger P, Bateman F B, Tosh R E and Chen-Mayer H 2013b Key comparison BIPM.RI(I)-K6 of the standards for absorbed dose to water of the NIST, USA and the BIPM in accelerator photon beams *Metrologia* **50** 06004–06004

Picard S, Burns D T, Roger P, Delaunay F, Gouriou J, Le Roy M, Ostrowsky A, Sommier L and Vermesse D 2013c Key comparison BIPM.RI(I)-K6 of the standards for absorbed dose to water of the LNE–LNHB, France and the BIPM in accelerator photon beams *Metrologia* **50** 06015–06015

Picard S, Burns D T, Roger P, Duane S, Bass G A, Manning J W and Shipley D R 2015a Key comparison BIPM.RI(I)-K6 of the standards for absorbed dose to water at 10 g cm-2 of the NPL, United Kingdom and the BIPM in accelerator photon beams *Metrologia* **52** 06021–06021

Picard S, Burns D T, Roger P, Duane S, Bass G A, Manning J W and Shipley D R 2015b Key comparison BIPM.RI(I)-K6 of the standards for absorbed dose to water at 5 g cm -2 and 7 g cm -2 of the NPL, United Kingdom and the BIPM in accelerator photon beams *Metrologia* **52** 06010–06010

Picard S, Burns D T, Roger P, Harty P D, Ramanathan G, Lye J E, Wright T, Butler D J, Cole A, Oliver C and Webb D V 2014 Key comparison BIPM.RI(I)-K6 of the standards for absorbed dose to water of the ARPANSA, Australia and the BIPM in accelerator photon beams *Metrologia* **51** 06006–06006

Picard S, Burns D T, Roger P, de Prez L A, Jansen B J and de Pooter J A 2017 Key comparison BIPM.RI(I)-K6 of the standards for absorbed dose to water of the VSL, Netherlands and the BIPM in accelerator photon beams *Metrologia* **54** 06005–06005

Pojtinger S, Dohm O S, Kapsch R-P and Thorwarth D 2018 Ionization chamber correction factors for MR-linacs *Phys. Med. Biol.* **63** 11NT03

de Prez L A 2008 Report: De NMi standaard voor geabsorbeerde dosis in water in hoogenergetische fotonenstraling **2007**

de Prez L A and de Pooter J A 2009 *Small field dosimetrie in high-energy photon beams based on water calorimetry : a feasibility study Development of a water calorimeter as a primary standard for absorbed dose to water measurements for HDR brachytherapy sources* Delft

de Prez L A and de Pooter J A 2008 The new NMi orthovolt x-rays absorbed dose to water primary standard based on water calorimetry. *Phys. Med. Biol.* **53** 3531–42

de Prez L A, de Pooter J A, Jansen B J and Aalbers A H L 2016a A water calorimeter for on-site absorbed dose to water calibrations in 60 Co and MV-photon beams including MRI incorporated treatment equipment *Phys. Med. Biol.* **61** 5051–76

de Prez L, Heukelom S, Jansen B, Jansen W, van de Kamer J, van Klink W, Kok E, Perik T, de Pooter J and Wittkämper F 2018a An on-site dosimetry audit for high-energy electron beams *Phys. Imaging Radiat. Oncol.* **5** 44–51

de Prez L, de Pooter J, Jansen B, Perik T and Wittkämper F 2018b Comparison of k Q factors measured with a water calorimeter in flattening filter free (FFF) and conventional flattening filter (cFF) photon beams *Phys. Med. Biol.* **63** 045023

de Prez L, de Pooter J, Jansen B, Perik T and Wittkämper F 2019a Corrigendum: Comparison of k Q factors measured with a water calorimeter in flattening filter free (FFF) and conventional flattening filter (cFF) photon beams (de Prez et al 2018 Phys. Med. Biol . 63 045023) *Phys. Med. Biol.* **64** 039501

de Prez L, de Pooter J, Jansen B, Wolthaus J, van Asselen B, Woodings S, Soest T, Kok J and Raaymakers B 2016b TH-CD-BRA-05: First Water Calorimetric Dw Measurement and Direct Measurement of Magnetic Field Correction Factors, KQ,B, in a 1.5 T B-Field of An MRI Linac *Med. Phys.* **43** 3874–3874

de Prez L, de Pooter J, Jansen B, Woodings S, Wolthaus J, van Asselen B, van Soest T, Kok J and Raaymakers B 2019b Commissioning of a water calorimeter as a primary standard for absorbed dose to water in magnetic fields *Phys. Med. Biol.* **64** 035013

de Prez L, Woodings S, de Pooter J, van Asselen B, Wolthaus J, Jansen B and Raaymakers B

10

References

2019c Direct measurement of ion chamber correction factors, k Q and k B , in a 7 MV MRI-linac *Phys. Med. Biol.* **64** 105025

Raaijmakers A J E, Raaymakers B W and Lagendijk J J W 2008 Magnetic-field-induced dose effects in MR-guided radiotherapy systems: Dependence on the magnetic field strength *Phys. Med. Biol.* **53** 909–23

Raaymakers B W, Jürgenliemk-Schulz I M, Bol G H, Glitzner M, Kotte A N T J, Van Asselen B, De Boer J C J, Bluemink J J, Hackett S L, Moerland M A, Woodings S J, Wolthaus J W H, Van Zijp H M, Philippens M E P, Tijssen R, Kok J G M, De Groot-Van Breugel E N, Kiekebosch I, Meijers L T C, Nomden C N, Sikkes G G, Doornaert P A H, Eppinga W S C, Kasperts N, Kerkmeijer L G W, Tersteeg J H A, Brown K J, Pais B, Woodhead P and Lagendijk J J W 2017 First patients treated with a 1.5 T MRI-Linac: Clinical proof of concept of a high-precision, high-field MRI guided radiotherapy treatment *Phys. Med. Biol.* **62** L41–50

Raaymakers B W, Lagendijk J J W, Overweg J, Kok J G M, Raaijmakers A J E, Kerkhof E M, van der Put R W, Meijsing I, Crijns S P M, Benedosso F, van Vulpen M, de Graaff C H W, Allen J, Brown K J, Raaymakers B W, Lagendijk J J W, Overweg J, Kok J G M, Raaijmakers A J E, Kerkhof E M, van der Put R W, Meijsing I, Crijns S P M, Benedosso F, van Vulpen M, de Graaff C H W, Allen J, Brown K J, Raaymakers B W, Lagendijk J J W, Overweg J, Kok J G M, Raaijmakers A J E, Kerkhof E M, van der Put R W, Meijsing I, Crijns S P M, Benedosso F, van Vulpen M, de Graaff C H W, Allen J and Brown K J 2009 Integrating a 1.5 T MRI scanner with a 6 MV accelerator: proof of concept *Phys. Med. Biol.* **54** N229–37

Raaymakers B W, Raaijmakers A J E, Kotte A N T J, Jette D and Lagendijk J J W 2004 Integrating a MRI scanner with a 6 MV radiotherapy accelerator: dose deposition in a transverse magnetic field *Phys. Med. Biol.* **49** 4109–18

Rapp B, Perichon N, Denoziere M, Daures J, Ostrowsky A and Bordy J-M 2013 The LNE-LNHB water calorimeter for primary measurement of absorbed dose at low depth in water: application to medium-energy x-rays. *Phys. Med. Biol.* **58** 2769–86

Renaud J, Marchington D, Seuntjens J and Sarfehnia A 2013 Development of a graphite probe calorimeter for absolute clinical dosimetry *Med. Phys.* **40** 020701

Renaud J, Rossomme S, Sarfehnia A, Vynckier S, Palmans H, Kacperek A and Seuntjens J 2016a Development and application of a water calorimeter for the absolute dosimetry of short-range particle beams *Phys. Med. Biol.* **61** 6602–19

Renaud J, Sarfehnia A, Marchant K, McEwen M, Ross C and Seuntjens J 2015 Direct measurement of electron beam quality conversion factors using water calorimetry *Med. Phys.* **42** 6357–68

Renaud J, Sarfehnia A, Woodings S, Kok J, van Asselen B, Wolthaus J, Raaymakers B and Seuntjens J 2016b TH-CD-BRA-10: Towards Reference Dosimetry of MR-Linacs Using a Clinical Probe-Format Calorimeter *Med. Phys.* **43** 3875–3875

Reynolds M, Fallone B G and Rathee S 2013 Dose response of selected ion chambers in applied homogeneous transverse and longitudinal magnetic fields *Med. Phys.* **40** 042102

Robar J L, Riccio S A and Martin M A 2002 Tumour dose enhancement using modified megavoltage photon beams and contrast media *Phys. Med. Biol.* **47** 305

Rogers D W O 1992 The advantages of absorbed-dose calibration factors *Med. Phys.* **19** 1227–39

Rogers D W O, Walters B and Kawrakow I 2015 *BEAMnrc Users Manual* 509 Ottawa

Ross C K and Klassen N V 1996 Water calorimetry for radiation dosimetry. *Phys. Med. Biol.* **41** 1–29

Ross C K and Shortt K R 1992 The effect of waterproofing sleeves on ionization chamber response *Phys. Med. Biol.* **37** 1403–11

Rumble J R, Lide D R and Bruno T J 2018 *CRC Handbook of Chemistry and Physics, 99th Edition* Boca Raton : CRC Press

Salvat F (Universitat D B, Fernandez-Varea J (Universitat D B and Sempau J (Universitat D B 2009 PENELOPE-2008: A Code System for Monte Carlo Simulation of Electron and Photon Transport 339

Salvat F, Fernández-Varea J M and Sempau J 2014 PENELOPE-2011: A code system for Monte Carlo simulation of electron and photon transport *Work. Proc.* **NEA/NSC/DO** 384

Sarfehnia A, Clasie B, Chung E, Lu H M, Flanz J, Cascio E, Engelsman M, Paganetti H and Seuntjens J 2010 Direct absorbed dose to water determination based on water calorimetry in scanning proton beam delivery. *Med. Phys.* **37** 3541–50

Sassowsky M and Pedroni E 2005 On the feasibility of water calorimetry with scanned proton radiation. *Phys. Med. Biol.* **50** 5381–400

Seltzer S M, Bartlett D T, Burns D T, Dietze G, Menzel H-G, Paretzke H G and Wambersie A 2011 ICRU Report 85 Fundamental Quantities and Units for Ionizing Radiation *J. ICRU* **11** NP.1-NP

Seuntjens J and Duane S 2009 Photon absorbed dose standards *Metrologia* **46** S39–58

Seuntjens J P, Ross C K, Shortt K R and Rogers D W O 2000 Absorbed-dose beam quality conversion factors for cylindrical chambers in high energy photon beams. *Med. Phys.* **27** 2763–79

Seuntjens J and Palmans H 1999 Correction factors and performance of a 4 degrees C sealed water calorimeter. *Phys. Med. Biol.* **44** 627–46

Smit K, van Asselen B, Kok J G M, Aalbers A H L, Lagendijk J J W and Raaymakers B W 2013 Towards reference dosimetry for the MR-linac: magnetic field correction of the ionization chamber reading *Phys. Med. Biol.* **58** 5945–57

Spindeldreier C K, Schrenk O, Bakenecker A, Kawrakow I, Burigo L, Karger C P, Greilich S and Pfaffenberger A 2017 Radiation dosimetry in magnetic fields with Farmer-type ionization chambers: determination of magnetic field correction factors for different magnetic field strengths and field orientations *Phys. Med. Biol.* **62** 6708–28

Szymanowski H, Baek W Y, Neungang-Nganwa R, Nettelbeck H and Rabus H 2015 PO-0850: MRI-Linac: Effect of the magnetic field on the interaction cross sections *Radiother. Oncol.* **115** S431

Thwaites D 2013 Accuracy required and achievable in radiotherapy dosimetry: Have modern technology and techniques changed our views? *J. Phys. Conf. Ser.* **444**

Thwaites D I and Malicki J 2011 Physics and technology in ESTRO and in Radiotherapy and Oncology: Past, present and into the 4th dimension *Radiother. Oncol.* **100** 327–32

Titt U, Vassiliev O N, Pönisch F, Dong L, Liu H and Mohan R 2006 A flattening filter free photon treatment concept evaluation with Monte Carlo *Med. Phys.* **33** 1595–602

Vassiliev O N, Titt U, Kry S F, Pönisch F, Gillin M T and Mohan R 2006 Monte Carlo study of photon fields from a flattening filter-free clinical accelerator *Med. Phys.* **33** 820–7

Wagner W and Pruß A 1999 The IAPWS Formulation 1995 for the Thermodynamic Properties of Ordinary Water Substance for General and Scientific Use *J. Phys. Chem. Ref. Data* **31** 387

Wambersie A 2001 What accuracy is required and can be achieved in radiation therapy (review of radiobiological and clinical data) *Radiochim. Acta* **89**

Weinhous M S and Meli J A 1984 Determining P ion , the correction factor for recombination losses in an ionization chamber *Med. Phys.* **11** 846–9

Woodings S J, Bluemink J J, de Vries J H W, Niatsetski Y, van Veelen B, Schillings J, Kok J G M, Wolthaus J W H, Hackett S L, van Asselen B, van Zijp H M, Pencea S, Roberts D A, Lagendijk J J W and Raaymakers B W 2018 Beam characterisation of the 1.5 T MRI-linac *Phys. Med. Biol.* **63** 085015

Xiao Y, Kry S F, Popple R, Yorke E, Papanikolaou N, Stathakis S, Xia P, Huq S, Bayouth J, Galvin J and Yin F F 2015 Flattening filter-free accelerators: a report from the AAPM Therapy Emerging Technology Assessment Work Group *J. Appl. Clin. Med. Phys.* **16** 5219

Xiong G and Rogers D W O 2008 Relationship between %dd(10)x and stopping-power ratios for flattening filter free accelerators: A Monte Carlo study *Med. Phys.* **35** 2104–9

Yu C X and Tang G 2011 Intensity-modulated arc therapy: Principles, technologies and clinical implementation *Phys. Med. Biol.* **56** R31–54

10

Publications

Papers in international journals:

de Prez L A, Woodings S, de Pooter J, van Asselen B, Wolthaus J, Jansen B and Raaymakers B 2019 *Direct measurement of ion chamber correction factors, k_Q and k_B, in a 7 MV MRI-linac Phys. Med. Biol.* 64 105025

de Prez L A, de Pooter J A, Jansen B J, Woodings S J, Wolthaus J W H, van Asselen B, van Soest T, Kok J and Raaymakers B W 2019 *Commissioning of a water calorimeter as a primary standard for absorbed dose to water in magnetic fields* Phys. Med. Biol. 64 035013

de Prez L A, Heukelom S, Jansen B, Jansen W, van de Kamer J, van Klink W, Kok E, Perik T, de Pooter J and Wittkämper F 2018 An on-site dosimetry audit for high-energy electron beams *Phys. Imaging Radiat. Oncol.* 5 44–51

de Prez L A, de Pooter J, Jansen B, Perik T and Wittkämper F 2018 *Comparison of k Q factors measured with a water calorimeter in flattening filter free (FFF) and conventional flattening filter (cFF) photon beams* Phys. Med. Biol. 63 45023

Woodings S J, van Asselen B, van Soest T L, de Prez L A, Lagendijk J J W, Raaymakers B W and Wolthaus J W H 2019 Technical Note: Consistency of PTW 30013 and FC65-Ah dG ion chamber magnetic field correction factors *Med. Phys.* 002 mp.13623

Picard S, Burns DT, Roger P, de Prez L A, Jansen BJ, de Pooter JA *Key comparison BIPM. RI(I)-K6 of the standards for absorbed dose to water of the VSL, Netherlands and the BIPM in accelerator photon beams*. Metrologia [Internet]. 2017 Jan 1;54(1A):06005–06005

de Prez L A, de Pooter J A, Jansen B J and Aalbers A H L 2016 *A water calorimeter for on-site absorbed dose to water calibrations in ⁶⁰Co and MV-photon beams including MRI-incorporated treatment equipment* Phys. Med. Biol. 5051

Büermann L, Pinto M, Pimpinella M, Stefano A, de Pooter J A, de Prez L A, Jansen B J, Rapp B and Denoziere M 2016 *First international comparison of primary absorbed dose to water standards in the medium-energy x-ray range* Metrologia 54 Techn. Suppl. 06007

de Pooter J A, de Prez L A and Bouchard H 2015 *Application of an adapted Fano cavity test for Monte Carlo simulations in the presence of B-fields* Phys. Med. Biol. 60 9313–27

Pinto M, Pimpinella M, Guerra A S, Rapp B, Denozière M, Büermann L, De Pooter J, De Prez L A, Machula G and Bordy J-M 2015 *Measuring absorbed dose to water in medium energy x-ray beams–traceability to the primary standards available in Europe and future dosimetry protocols Phys. Medica* 31 e49

Burns D T, Kessler C, de Prez L A and Joulaeizadeh L 2014 *Key comparison BIPM.RI(I)-K2 of the air-kerma standards of the VSL, Netherlands and the BIPM in low-energy x-rays* Metrologia 51 (2014) Tech. Suppl. Series 06010

Kessler C, Burns D T, de Prez L A, Joulaeizadeh L 2014 *Key comparison BIPM.RI(I)-K7 of the air-kerma standards of the VSL, Netherlands and the BIPM in mammography x-rays* Metrologia 51 Tech. Suppl. Series 06025

Kessler C, Allisy-Roberts P J, de Prez L A and van Dijk E 2010 *Comparison of the standards for air kerma of the VSL and the BIPM for ⁶⁰Co gamma radiation* Metrologia 47 Tech. Suppl. 06015

Burns D T and de Prez L A 2009 *Key comparison BIPM.RI(I)-K3 of the air-kerma standards of the VSL, Netherlands and the BIPM in medium-energy x-rays* Metrologia 46 Tech. Suppl. 06002

Kessler C, Allisy-Roberts P J, Burns D T, Roger P, de Prez L A, de Pooter J A and Damen P M G 2009 *Comparison of the standards for absorbed dose to water of the VSL and the BIPM for ⁶⁰Co γ-rays* Metrologia 46 Tech. Suppl. 06009

de Prez L A and de Pooter J A 2008 *The new NMi orthovolt x-ray absorbed dose to water primary standard based on water calorimetry* Phys. Med. Biol. 53 3531-3542

Kessler C, Burns D T, Büermann L and de Prez L A 2007 *A study of the response of ionization chambers to mammography beams* Rapport BIPM-07/02

NCS-reports:

de Prez L A, Heukelom S, Jansen B, Jansen W, Kok E, Perik T, de Pooter J and Wittkämper F 2018 *NCS Report 29: An on-site dosimetry audit for high-energy electron beams* Delft

Perik T J, de Prez L A, Aalbers A H L, Monseux A, Sergent F, Wittkämper F W and van de Kamer J B 2013 *Audit of High-Energy Photon Beams in Belgian and Dutch Radiotherapy Departments NCS report 23* of the Netherlands Commission on Radiation Dosimetry, December

Aalbers A H L, Hoornaert M-T, Minken A, Palmans H, Vynckier S, Pieksma M W H, de Prez L A, Reynaert N and Wittkämper F W 2008 *NCS report 18: Code of Practice for the Absorbed Dose Determination in High Energy Photon and Electron Beams* Report 18 Nederlandse Commissie voor Stralingsdosimetrie Delft

10

Dankwoord / Acknowledgements

Familie, vrienden en collega's (inclusief iedereen die ik hieronder niet expliciet noem), bedankt voor jullie vertrouwen, interesse, discussies, motivatie, inspiratie en geduld. Mede door jullie is dit proefschrift tot stand gekomen.

Silvana, zonder jou zou ik nooit aan dit avontuur zijn begonnen. Jij bent mijn grote steun en motivator. Jij hebt mij gestimuleerd om het beste uit mezelf te halen en (vlot) door te zetten. **Emma**, jij bent mijn grootste bron van inspiratie. Bedankt dat je me er vaak op wijst dat ik je trotse papa mag zijn.

Bas Raaymakers, promotor, jij was vanaf de eerste dag enthousiast over m'n promotieonderzoek. Mede dankzij jou heb ik de afgelopen periode een dag in de week bij het UMCU kunnen werken. Ik heb genoten van onze discussies en samenwerking en heb veel geleerd van je praktische en nuchtere kijk op dingen.

Begeleiders, onze discussies, jullie begeleiding en aanmoedigingen zijn dit proefschrift ten goede gekomen. **Bram van Asselen**, jouw inzicht in de klinische aspecten van dosimetrie heeft dit werk toepasbaarder gemaakt. **Jacco de Pooter**, dankzij jou ben ik niet gestruikeld over mijn eigen afleidingen en formules. **Jochem Wolthaus**, door jouw

inzicht was ik in staat m'n werk toegankelijker te maken voor een bredere doelgroep.

Carlos Rosas Mendoza and Tony Aalbers, I am proud that both of you didn't hesitate to be my paranymph. **Carlos***,* thank you for your trust and for your support towards me and my family. **Tony**, jij hebt mij geleerd dat succesvolle metrologie (dosimetrie in het bijzonder) draait om de verbinding tussen mensen. Het was eind jaren 1990 jouw oorspronkelijke idee om een transportabele watercalorimeter te ontwikkelen.

Job Kneppers, Luc Kouters, Tim Sanders en Maurice Heemskerk, jullie hebben de nieuwe calorimeter ontworpen en gebouwd. Ik waardeer jullie creativiteit, doorzettingsvermogen en geduld tijdens onze zoektocht naar het beste ontwerp binnen de kaders van de gestelde eisen.

VSL-collega's, VSL is wereldwijd een speler op het gebied van geabsorbeerd dosis in water. Ik heb het vertrouwen dat we dat kunnen voortzetten en uitbouwen. **Marc Pieksma**, wat we geleerd hebben gedurende onze tientallen metingen voor NCS-18 heeft bijgedragen aan het succes van de nieuwe calorimeter. Mede dankzij jouw raad en je aanmoediging is dit proefschrift er gekomen. **Bartel Jansen**, onze vele metingen met de nieuwe calorimeter hebben ons inzicht gegeven in alle aspecten van het systeem. We hebben mooie resultaten geboekt. **Andrea Peruzzi**, dankzij jouw verwijzing naar de thermodynamische vergelijkingen is het gelukt een verband te leggen tussen het aanwezige magneetveld en de soortelijke warmte van water. **Gert Rietveld**, dankzij jou is het gelukt om digitale multimeters in te zetten voor onze temperatuurmetingen. Je 'last-minute' commentaar en bijdragen aan dit proefschrift hebben het beter gemaakt. **Frans Bader, Louise van Bloois, Paz Avilès Lucas, Elfried Kok, Tessel van der Laan, Jacob-Jan de Boer,** bedankt voor jullie bijdragen, interesse, begrip en geduld in de afgelopen periode. **Lydia de Koning en Gerla Koole,** dankzij jullie kon ik zonder problemen in Utrecht starten. **Directie en management**, dankzij jullie ondersteuning en vertrouwen was het mogelijk om mijn woensdagen bij VSL in te ruilen voor een dag in het ziekenhuis.

UMCU-collega's, ik heb genoten van onze samenwerking en ik heb bewondering voor wat jullie met de MRI-linacgroep hebben neergezet. **Simon Woodings**, onze discussies tijdens de metingen, overleggen en korte koffiepauzes hebben mij altijd aan het nadenken gehouden. **Jan Kok**, dankzij jouw enorme kennis en je tomeloze inzet, zijn onze metingen succesvol verlopen. **Theo van Soest**, onze discussies over ionisatiekamercorrecties hebben me telkens geboeid. **Sarah Hackett**, jouw nuchtere inzicht heeft me meerdere malen op het juiste spoor gehouden. **Jan Lagendijk**, dankzij

10

jouw geweldige team is mij de mogelijkheid geboden om de nieuwe calorimeter realiteit te maken. **Niels Raaijmakers, Tristan van Heijst, Astrid van Lier, Loes van Zijp**, dankzij jullie kon ik op de woensdagen rustig werken op m'n vaste werkplek in jullie klifio-kamer. Ik ben jullie dankbaar voor het regelen van een stoel, een beeldscherm en een toetsenbord maar bovenal voor de vele fijne gesprekken. Ik denk met veel genoegen terug aan deze periode.

Thijs Perik, Jochem Kaas, Frits Wittkämper, dankzij jullie bijdragen en de beschikbaar gestelde bundeltijd bij het AVL zijn de allereerste metingen met de calorimeter goed verlopen. Ik heb genoten van onze samenwerking en hoop dat dit nog lang zo voortgaat.

Graham Bass, James Manning, Ileana Silvestre, Simon Duane, thank you for kindly providing us beam time and technical support at the NPL clinical accelerator facilities during the BIPM.RI(I)-K6 key comparison.

Susanne Picard, David Burns, Philip Roger, Cecilia Kessler, Penny Allisy-Roberts, you inspired me to achieve the best and most reliable measurement results.

Christian Pychlau, thanks to your kind and prompt help we were able to verify or modify the PTW dosimetry equipment for application inside the magnetic field of the MRI-linac.

Karen Christaki, thanks to you we were able to visit Elekta in December 2013 and virtually-fit the new calorimeter in the bore of the Elekta Unity.

Carina, gracias por tú continuo apoyo y confianza; para mi y mi familia. **Frans en Marciel**, bedankt voor jullie steun, interesse en vertrouwen en het doorworstelen van de Nederlandse samenvatting.

Curriculum Vitae

Leon de Prez is op zaterdag 1 maart 1975 geboren in Schiedam. Daar groeide hij ook op. Na basisschool De Notenkraker stroomde Leon door naar HAVO (bèta) op Scholengemeenschap Spieringshoek. In 1998 behaalde hij zijn diploma *Technische Natuurkunde* aan de r.-k. TH Rijswijk (nu HHS, Delft). Tijdens zijn stage- en afstudeeropdrachten voor deze opleiding bij het toenmalige Nederlands Meetinstituut (nu VSL, Delft) is zijn interesse gewekt voor radioactiviteit en dosimetrie. Hier is, samen met Tony Aalbers, Tom Grimbergen en Eduard van Dijk, de basis gelegd voor de eerste transportabele watercalorimeter. Later is deze calorimeter samen met Marc Pieksma en Eduard van Dijk uitgewerkt tot een volwaardige primaire standaard, die voor het eerst in 2005 bij het BIPM in Sèvres (Parijs) deelnam aan een key comparison. Onder begeleiding van Ben Mijnheer en Jacco de Pooter heeft Leon zijn master thesis afgerond aan de INHOLLAND Academy in Haarlem (i.s.m. South Bank University, London) met als onderwerp het meten van kleine fotonenbundels met de toenmalige watercalorimeter. Naast calorimetrie heeft Leon zich tijdens zijn loopbaan beziggehouden met de ontwikkeling, beheer en implementatie van (nieuwe) meetmethoden, kwaliteitssystemen en automatisering. De afgelopen 19 jaar was Leon werkzaam bij VSL waarvan de laatste 2 jaar parttime gedetacheerd bij het UMC in Utrecht met dit proefschrift als resultaat.